

**AN EXPERIMENTAL INVESTIGATION ON
PROPERTIES OF Cu-Al-Be-X SHAPE MEMORY
ALLOYS FOR SMART STRUCTURE
APPLICATIONS**

Thesis

Submitted in partial fulfillment of the requirements for the degree of
DOCTOR OF PHILOSOPHY

by

G. BALA NARASIMHA



**DEPARTMENT OF MECHANICAL ENGINEERING
NATIONAL INSTITUTE OF TECHNOLOGY KARNATAKA,
SURATHKAL, MANGALORE - 575025**

NOVEMBER – 2020

**AN EXPERIMENTAL INVESTIGATION ON
PROPERTIES OF Cu-Al-Be-X SHAPE MEMORY
ALLOYS FOR SMART STRUCTURE
APPLICATIONS**

Thesis

Submitted in partial fulfillment of the requirements for the degree of
DOCTOR OF PHILOSOPHY

by

G. BALA NARASIMHA

Under the guidance of

Prof. S.M. MURIGENDRAPPA

Professor



DEPARTMENT OF MECHANICAL ENGINEERING
NATIONAL INSTITUTE OF TECHNOLOGY KARNATAKA,
SURATHKAL, MANGALORE - 575025

NOVEMBER – 2020

DECLARATION

I hereby *declare* that the Research Thesis entitled “**AN EXPERIMENTAL INVESTIGATION ON PROPERTIES OF Cu-Al-Be-X SHAPE MEMORY ALLOYS FOR SMART STRUCTURE APPLICATIONS**” which is being submitted to the **National Institute of Technology Karnataka, Surathkal** in partial fulfillment of the requirements for the award of the degree of **Doctor of Philosophy in Mechanical Engineering** is a *bonafide report of the research work carried out by me*. The material contained in this Research Thesis has not been submitted to any other Universities or Institutes for the award of any degree.

Register Number: **145072ME14F05**

Name of the Research Scholar: **G. Bala Narasimha**

Signature of the Research Scholar:

G. Bala Narasimha
8/7/2020

Department of Mechanical Engineering

Place: NITK-Surathkal

Date: *08/07/2020*

CERTIFICATE

This is to *certify* that the Research Thesis entitled “**AN EXPERIMENTAL INVESTIGATION ON PROPERTIES OF Cu-Al-Be-X SHAPE MEMORY ALLOYS FOR SMART STRUCTURE APPLICATIONS**” submitted by **Mr. G. Bala Narasimha. (Register Number: 145072ME14F05)** as the record of the research work carried out by him, *is accepted as the Research Thesis submission* in partial fulfillment of the requirements for the award of the degree of **Doctor of Philosophy.**



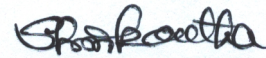
Prof. S.M. Murigendrappa

Research Guide

Professor

Dept. of Mechanical Engg.

NITK, Surathkal.



Chairman - DRPC

Prof. Shrikantha S. Rao

Dedicated to....



INDIAN ARMY

ACKNOWLEDGEMENT

I cannot believe this long journey called PhD has come to an end. It has been a very intensive but yet invaluable experience in my life, and its successful completion would not have been possible without the precious help of my supervisor, faculty members, colleagues, friends and family. It is a pleasure to have an opportunity to convey my thanks to them all.

Firstly, I would like to express my deepest sense of gratitude and heartfelt thanks to my supervisor and mentor **Prof. S.M. Murigendrappa** for his guidance and support from the very early stages of this research. His experience, passion, dedication and kindness have inspired me to challenge myself and develop as a person as well as improve my technical abilities. His encouragement at every step of my research boosts me to finish tasks with much confidence and knowledge.

I would like to thank the **Department of Science and Technology, Science and Engineering Research Board**, India, for financially supporting this part of research under grant No. **EMR/2016/001247**.

I am grateful to Research Progress Assessment Committee members, **Dr. Subashchandra Kattimani**, Department of Mechanical Engineering and **Dr. Vishwanath K.P.**, Department of Mathematical and computational sciences for their critical evaluation and valuable suggestions during the progress of the work.

I am greatly indebted to **Prof. Gangadharan K. V.** and **Prof. Narendranath S.** the former Heads of the Department of Mechanical Engineering, and **Prof. Shrikantha S. Rao**, the present Head of the Department of Mechanical Engineering, for providing all kind of necessary facilities in the department to carry out the experimental research.

I express my heartfelt thanks to **Dr. S. Parida**, Department of Metallurgical Engineering and Materials Science, IIT Bombay for supporting in the preparation of master alloys for the research work.

I express my heartfelt gratitude to **Prof. Narendranath S., Dr. Ramesh M. R.** and **Dr. Mrityunjay Doddamani**, Department of Mechanical Engineering and **Dr. Ravishankar K.S.** Department of Metallurgical and Materials Engineering for extending the support for experimental work.

I express my heartfelt gratitude to **Prof. Rajendra Udupa K., Prof. Udaya Bhat K.** and **Prof. Jagnannath Nayak**, Department of Metallurgical and Materials engineering for their technical advices and suggestions during the research work.

I am also grateful to all the teaching and non-teaching staff members of the Department of Mechanical Engineering, Department of Metallurgical and Materials Engineering, Department of Physics and Department of Chemical Engineering for their timely help in completing my research work.

I heartfully acknowledge each member of my research consortium, **Mr. T. Kalinga, Mr. Ratnesh kumar Singh, Mr. M. L. J. Suman, Mr. V S Phani Kumar, Mr. Mohammed Sohail Bakshi, Mr. Chetan HC** and **Mr. Vinayak kallannavar** with whom I enjoyed working and shared ideas in developing knowledge.

It is also a pleasure to acknowledge and convey thanks to my friends **Mr. Venkatadri Tekuri, Mr. Bharath Kumar Momidi, Mr. Sangamesh Rajole** for their help in conducting the numerous experimental tests and characterization. It would have never been possible to complete the research without their contribution.

I would like to pay a special thanks to my friends **Mr. Yashwanth B., Mr. Pratheep Reddy T., Mr. Susheel Kumar G.N., Mr. Mallikarjun Balichakra, Mr. Rajesh Gogineni, and Mr. Sreenivasulu P.** with whom I shared many laughs and tears. They have been supportive at any time of the day and night during all my ups and downs and for their timely help and moral support.

I would like to pay deepest sense of gratitude to my mother **Mrs. Dhakshayani Guniputi**, and aunt **Mrs. Kumari** who taught me values and brought up me to achieve this degree. A special and heartfelt thanks, gratitude, love and affection to my beloved entire family members, especially to my lovely sister **Mrs. Lakshmi Priya** and brother in law **Mr. Harish Kumar** and my brother **Mr. Narasimha Rao Guniputi** for their love and persistent confidence in me have taken the load off my shoulder. They have been patient to put up with me when I was stressed and they have been unselfishly happy for my successes. I would have never been able to do what I managed to achieve without their endless support.

Finally, I would also like to take this opportunity to convey my profound gratitude to everybody who have supported directly or indirectly and encouraged me during all these years. The successful completion of this thesis would not have been possible without them.

G. BALA NARASIMHA

ABSTRACT

Smart materials are new class of materials, capable of sensing and responding to the change of its environment are of much interest in robotics, structural, biomedical and aerospace technologies. Shape memory alloys (SMA), Shape memory polymers (SMP), Hydrogels, Electrostrictive (ES), Electrorheological (ER), Piezoelectric (PE), and Magnetostrictive (MS), Magnetorheological (MRE) are the most common smart materials. Among these, shape memory alloys hold a peculiar property viz. deformed material can restore their actual shape either by an increase in temperature or removal of the load, known as shape memory effect and super-elasticity respectively. These two distinct properties attract the usage of SMA's as actuators in smart structures to suppress flutter and in civil structures to isolate vibrations.

Past decades, intense research has been carried out and still progressing in the development of a novel, economical and long functional SMA for the flutter suppression in the smart/adaptive structures. From 1960s to till today, Ni-Ti based SMAs are used mostly in applications because of their superior advantages i.e., high strain recovery, long functional life, however their utilization is limited due to the difficulties in processing and expensive. Cu-Al based shape memory alloys are selected as an alternative to Ni-Ti (Nitinol), because of ease of production and economical.

This thesis is concerned with the design and development of Cu-Al-Be based shape memory alloys with improved microstructure, mechanical properties, and narrow thermal hysteresis with better shape/strain recovery for the actuator applications. The investigation has been carried out on the effect of variation in wt.% of Cu, Al, Be and the grain refiners viz. Boron (B), zirconium (Zr), and rare-earth elements, cerium (Ce) and gadolinium (Gd), and also manganese (Mn) on microstructure, mechanical and shape memory properties. The present investigation suggests that Al plays a vital role in the modification of martensitic fraction followed by Be. Boron and zirconium grain refiners enhance the grain refinement with minimal addition and better shape recovery. Cu-Al-Be-B shape memory alloys are chosen as suitable for the rapid response.

Keywords: *Cu-Al-Be, Shape memory alloys, Grain Refiners, Rare-earth elements, Grain refinement, Ductility, Shape memory effect, Thermal Hysteresis.*

Contents

Contents	i
List of Figures	iv
List of Tables	vii
ABBREVIATIONS.....	viii
ROMAN SYMBOLS	ix
GREEK LETTERS	xi
1 INTRODUCTION.....	1
1.1 Background of study	1
1.2 Limitations of Study.....	3
1.3 Motivation	3
1.4 Organization of Thesis	4
2 LITERATURE SURVEY	5
2.1 Introduction	5
2.2 Smart materials	5
2.2.1 Types of smart materials	5
2.3 Shape memory alloys	7
2.3.1 Shape memory effect (SME)	8
2.3.2 Pseudo-elasticity (PE).....	9
2.4 Types of shape memory alloys	9
2.4.1 Ni-Ti.....	10
2.4.2 Cu-Zn-Al.....	10
2.4.3 Cu-Al.....	12
2.4.4 Cu-Al-Ni	13
2.4.5 Cu-Al-Mn.....	14
2.4.6 Cu-Al-Be.....	15
2.5 Grain refinement	17
2.5.1 Grain Refiners	17
2.5.2 Thermal treatments	21
2.5.3 Severe plastic deformation - Equal channel angular pressing (ECAP) .	22

2.6	Transition temperatures	23
2.6.1	Alloying elements	23
2.6.2	Effect of thermal treatments.....	24
2.7	Response - Thermal hysteresis	24
2.8	Identification of the problem.....	25
2.9	Research gaps	25
2.10	Objectives	26
2.11	Closure.....	26
3	MATERIALS AND METHODS.....	27
3.1	Introduction	27
3.2	Elemental compositions	27
3.3	Metals and purity	28
3.4	METHODOLOGY.....	31
3.4.1	Alloy preparation	32
3.4.2	Characterization	33
3.5	Closure.....	36
4	RESULTS & DISCUSSION	37
4.1	Introduction	37
4.2	Cu-Al-Be – Ternary SMAs	37
4.2.1	XRD – Phases	39
4.2.2	Microstructure and morphology	40
4.2.3	Phase transformation temperatures	42
4.2.4	Shape recovery ratio	45
4.2.5	Mechanical properties	45
4.3	Cu-Al-Be-B	48
4.3.1	XRD - Phases.....	49
4.3.2	Microstructure and morphology	52
4.3.3	Phase transformation temperatures	56
4.3.4	Shape recovery ratio	60
4.3.5	Mechanical properties	61

4.4	Cu-Al-Be-Ce	64
4.4.1	XRD - Phases	65
4.4.2	Microstructure and morphology	66
4.4.3	Phase transformation temperatures	69
4.4.4	Shape recovery ratio	72
4.5	Cu-Al-Be-Gd.....	73
4.5.1	XRD - Phases	73
4.5.2	Microstructure and morphology	74
4.5.3	Phase transformation temperatures	76
4.5.4	Shape recovery ratio	77
4.5.5	Mechanical Properties.....	78
4.6	Cu-Al-Be-Mn	81
4.6.1	XRD - Phases	81
4.6.2	Microstructure and Morphology	83
4.6.3	Phase transformation temperatures	85
4.6.4	Shape recovery ratio	87
4.7	Cu-Al-Be-Zr.....	89
4.7.1	XRD – phases	89
4.7.2	Microstructure and morphology	91
4.7.3	Phase transformation temperatures	94
4.7.4	Shape recovery ratio	95
4.7.5	Mechanical Properties.....	96
4.8	Closure	99
5	CONCLUSIONS & FUTURE SCOPE	101
5.1	Conclusions	101
5.2	Scope for further research.....	102
	References.....	103
	List of publications based on Ph.D. research work.....	121
	BIODATA.....	122

List of Figures

Figure 2.1 Smart Materials based on Energy Transformation.....	6
Figure 2.2 Phases and crystal structures	8
Figure 2.3 Shape Memory Effect.....	8
Figure 2.4 Pseudoelasticity.	9
Figure 2.5 Types of SMAs.....	9
Figure 2.6 Types of Cu-based SMAs.....	10
Figure 2.7 Pseudo binary Cu-Zn phase diagram.....	11
Figure 2.8 Cu – Al phase diagram	12
Figure 2.9 Pseudo binary Cu-Al-Ni phase diagram.....	13
Figure 2.10 Pseudo binary phase diagram of Cu-Al-Mn.....	14
Figure 2.11 Quasi binary phase diagram of Cu-Al-Be.	16
Figure 3.1 Aluminium buttons.....	28
Figure 3.2 CuBe ₄ master alloy.....	28
Figure 3.3 a) Photograph of CuB ₂ Inoculant b) EDS of CuB ₂ Inoculant	29
Figure 3.4 a) Photograph of Cu ₉ Gd ₂ Inoculant b) EDS of Cu ₉ Gd ₂ Inoculant.....	29
Figure 3.5 a) Photograph of CuMn ₃₀ Inoculant b) EDS of CuMn ₃₀ Inoculant.....	30
Figure 3.6 a) Photograph of Cu ₅₁ Zr ₁₄ Inoculant b) EDS of Cu ₅₁ Zr ₁₄ Inoculant.....	30
Figure 3.7 Flow chart of Methodology	31
Figure 3.8 Induction melting furnace with inert gas setup.	32
Figure 3.9 Muffle Furnace with inert gas setup.....	32
Figure 3.10 Alloy Plate.....	32
Figure 3.11 Bend Test.....	35
Figure 3.12 Tensile Specimens	36
Figure 4.1 Cu-Al phase diagram.....	38
Figure 4.2 X-ray diffractograms of Cu-Al-Be SMAs.....	39
Figure 4.3 Microstructures of Cu-Al-Be SMAs.	40
Figure 4.4 Thermograms of T_1 , T_2 , T_3 , and T_4 Cu-Al-Be SMAs.....	42
Figure 4.5 Thermograms of T_5 , T_6 , T_7 , T_8 , T_9 , T_{10} , and T_{11} Cu-Al-Be SMAs.	43
Figure 4.6 Shape recovery ratio of Cu-Al-Be SMAs.....	45
Figure 4.7 Stress-strain Curves of Cu-Al-Be SMAs.....	46

Figure 4.8 Fracture morphology of Cu-Al-Be SMAs.....	47
Figure 4.9 X-ray diffractograms of B_{1Y} alloys.....	49
Figure 4.10 X-ray diffractograms of B_{21} and B_{31} alloys.....	50
Figure 4.11 X-ray diffractograms of B_{44} and B_{54} alloys.....	51
Figure 4.12 X-ray diffractograms of B_{62} and B_{72} alloys.....	51
Figure 4.13 Microstructures of Cu-Al-Be-B SMAs.....	53
Figure 4.14 SEM images of Cu-Al-Be-B SMAs.....	54
Figure 4.15 Thermogram – B_{1Y} SMAs.....	57
Figure 4.16 Thermogram – B_{11} , B_{21} and B_{31} SMAs.....	58
Figure 4.17 Thermogram – B_{44} , B_{54} SMAs.....	58
Figure 4.18 Thermogram – B_{62} , B_{72} SMAs.....	59
Figure 4.19 Shape recovery ratio of Cu-Al-Be-B SMAs.....	61
Figure 4.20 Stress strain curves of Cu-Al-Be-B SMAs.....	62
Figure 4.21 Fracture morphology of Cu-Al-Be-B SMAs.....	63
Figure 4.22 X-ray diffractograms of Cu-Al-Be-Ce SMAs.....	65
Figure 4.23 Microstructures of Cu-Al-Be-Ce SMAs.....	66
Figure 4.24 SEM images of Cu-Al-Be-Ce SMAs.....	67
Figure 4.25 Thermograms of Cu-Al-Be-Ce SMAs.....	71
Figure 4.26 Shape recovery ratio of Cu-Al-Be-Ce SMAs.....	72
Figure 4.27 X-Ray Diffractogram of Cu-Al-Be-Gd SMAs.....	74
Figure 4.28 Microstructures of Cu-Al-Be-Gd SMAs.....	75
Figure 4.29 SEM images of Cu-Al-Be-Gd SMAs.....	75
Figure 4.30 Thermograms – Cu-Al-Be-Gd SMAs.....	76
Figure 4.31 Shape recovery ratio of Cu-Al-Be-Gd alloys.....	78
Figure 4.32 Stress- strain curves of Cu-Al-Be-Gd SMAs.....	79
Figure 4.33 Fracture morphology of Cu-Al-Be-Gd SMAs.....	80
Figure 4.34 X-ray diffractograms of Cu-Al-Be-Mn SMAs.....	82
Figure 4.35 Microstructures of Cu-Al-Be-Mn SMAs.....	84
Figure 4.36 Thermograms of Cu-Al-Be-Mn SMAs.....	86
Figure 4.37 Shape recovery ratio of Cu-Al-Be-Mn Alloys.....	88
Figure 4.38 X-ray diffractograms of Cu-Al-Be-Zr SMAs.....	90
Figure 4.39 Microstructures of Cu-Al-Be-Zr SMAs.....	91

Figure 4.40 SEM images of Cu-Al-Be-Zr SMAs.	93
Figure 4.41 Thermograms of Cu-Al-Be-Zr SMAs.	94
Figure 4.42 Shape recovery ratio of Cu-Al-Be-Zr SMAs.	96
Figure 4.43 Stress-strain curves of Cu-Al-Be-Zr SMAs.	97
Figure 4.44 Fracture morphology of Cu-Al-Be-Zr SMAs.	99

List of Tables

Table 3.1 Elements and its range used in the investigation.	27
Table 3.2 Type of metals and their purity.....	28
Table 4.1 Elemental composition and designations of Cu-Al-Be SMAs	38
Table 4.2 Transformation temperatures, enthalpies, and hysteresis of Cu-Al-Be SMAs.	44
Table 4.3 Mechanical properties of ternary Cu-Al-Be SMAs.	46
Table 4.4 Elemental composition and designations of Cu-Al-Be-B SMAs.	48
Table 4.5 Transformation temperatures, enthalpies, and hysteresis of Cu-Al-Be-B SMAs.	60
Table 4.6 Mechanical Properties of Cu-Al-Be-B SMAs.	63
Table 4.7 Elemental composition and designations of Cu-Al-Be-Ce SMAs.....	64
Table 4.8 Transformation temperatures, enthalpies, and hysteresis of Cu-Al-Be-Ce SMAs	71
Table 4.9 Elemental composition and designations of Cu-Al-Be-Gd SMAs.	73
Table 4.10 Transformation temperatures, enthalpies, and hysteresis of Cu-Al-Be-Gd SMAs.	77
Table 4.11 Mechanical properties of Cu-Al-Be-Gd SMAs.	79
Table 4.12 Elemental composition and designations of Cu-Al-Be-Mn SMAs.	81
Table 4.13 Transformation temperatures of Cu-Al-Be-Mn SMAs.....	87
Table 4.14 Elemental composition and designations of Cu-Al-Be-Zr SMAs.	89
Table 4.15 Transformation temperatures, enthalpies, and hysteresis of Cu-Al-Be-Zr SMAs.	95
Table 4.16 Mechanical Properties of Cu-Al-Be-Zr SMAs.	96

ABBREVIATIONS

ASTM	- American society for testing material
ARB	- Accumulative roll bonding
BCC	- Body-centered cubic
DSC	- Differential scanning calorimeter
ECAP	- Equal channel angular pressing
EDS	- Energy dispersive spectrum
FCC	- Face centered cubic
ICP-OES	- Inductively coupled plasma optical emission spectrometer
PE	- Pseudo-Elasticity
REE	- Rare-earth element
SEM	- Scanning electron microscope
SME	- Shape memory effect
SMA	- Shape memory alloy
SMAHC	- Shape memory alloy hybrid composite
UTM	- Universal testing machine
XRD	- X-ray diffraction

ROMAN SYMBOLS

Al	- Aluminium
A_f	- Austenite finish temperature
A_s	- Austenite start temperature
Au	- Aurum
B	- Boron
Be	- Beryllium
Cd	- Cadmium
Ce	- Cerium
Co	- Cobalt
Cu	- Copper
Fe	- Iron
FeCl₃	- Ferric chloride
Ga	- Gallium
Gd	- Gadolinium
gms	- Grams
HCl	- Hydrochloric acid
Hf	- Hafnium
HNO₃	- Nitric acid
hrs	- Hours
In	- Indium
K	- Kelvin
La	- Lanthanum
m	- Minutes
M_f	- Martensite finish temperature
Mn	- Manganese
MPa	- Mega pascal
M_s	- Martensite start temperature
Nb	- Niobium
Ni	- Nickel
Pd	- Palladium

s	-	Seconds
Sc	-	Scandium
Tl	-	Thallium
Ti	-	Titanium
Tq	-	Quench temperature
V	-	Vanadium
wt.%	-	Weight Percentage
Y	-	Yttrium
Zn	-	Zinc
Zr	-	Zirconium

GREEK LETTERS

μm	-	Micron or Micrometer
η	-	Shape recovery ratio
θ_d	-	Angle after deformation
θ_r	-	Residual angle after recovery
β	-	Disordered austenite
β_1	-	Metastable austenite
β'_1	-	Martensite
γ'_1	-	Martensite
γ_2	-	Cu ₉ Al ₄
ΔH	-	Enthalpy difference

CHAPTER 1

INTRODUCTION

1.1 BACKGROUND OF STUDY

Over the past three decades, there have been significant efforts to study and avoid the critical aeroelastic problems of aircraft, such as instability and catastrophic structural failures due to severe vibrations (Dongi et al. 1996). Flutter is the dynamic aeroelastic instability phenomenon, happens due to the interactions of the inertial force, elastic force, and aerodynamic load. Flutter increases the amplitude of vibration, which causes high in-plane cyclic stresses and possible failure of the wing, which is very unsafe for aircraft structures. Moreover, when the vehicle flies in the supersonic region, the airflow not only produces the aerodynamic pressure but also raises temperatures on the vehicle surface. The temperature increase of the skin could induce the in-plane force and bending moment in the panel. The induced in-plane force may cause instability and complex behavior in the panel.

The current goals of the aviation industry are to (i) build lightweight structures using advanced composites, simple design with the least number of components, and (ii) to improve the efficiency and performance of aircraft by isolation/suppression of the unwanted vibrations on the aircraft. To meet these requirements, embedding/incorporating smart materials into the composite structures yields higher stiffness of the structure with the conjunction of various passive/active control strategies. These structures are termed as smart structures/adaptive structures. The smart materials have a high affinity to change shape, natural frequency, stiffness, buckling effect, damping, and other mechanical parameters with respect to change in electric, magnetic field or temperature.

Piezoelectric materials and Shape memory alloys are the two most commonly used smart materials in the aircraft structures for flutter suppression. Piezoelectric materials refer to substances that have the electromechanical coupling effect, i.e., an

electric charge will be produced when an external load is applied on a piezoelectric element, and conversely, a mechanical deformation will be generated by applying an electric field to the piezoelectric material. Shape Memory Alloys hold a peculiar property, shape memory effect, i.e., in low temperatures, it is possible to make relatively large deformation such as bending, twisting, compressing or stretching, and by heating the deformed SMA returns to its original shape.

Many researchers investigated aircraft control and flutter suppression using piezoelectric (Dongi et al. 1996; Fazelzadeh and Jafari 2008; Moon and Seok 2005; Parameswaran et al. 2015; Song and Li 2011) and shape memory alloys (Epps and Chandra 1997; Garafolo and Mchugh 2018; Rogers 1990; Xinyun et al. 2007). Piezoelectric materials exhibit rapid response and better performance; however, the limitations in the application require high excitation voltage for actuation, develops low forces at higher frequencies, and an increase in the number of piezo patches on the panel induces additional mass leads to bending (Garafolo and Mchugh 2018). The shape memory alloys are another class of smart material used to control flutter. SMAs are pre-strained and embedded in the structures acts as a flutter suppression element, and these structures are known as shape memory alloy hybrid composites (SMAHC). When the SMAHC deforms at low temperatures, an electric current is passed through SMA wires, generates heat by the property of electrical resistance, and the deformed SMA wires tends to revert to the parent state generates a large internal force, and this force is transmitted to the structure modifies /increases the equivalent stiffness of the structure. Besides, the limitations in the application of SMAs are martensite stabilization/deterioration of shape memory and an increase in transformation temperatures after a few functional cycles. Comparing the advantages and disadvantages, SMAs have many advantages such as simple, clean, lightweight, easy miniaturization, large force, high energy density, high power-to-weight ratio, flexible configuration, solid-state actuators, reduction in total part count and ease of inspection (Roy and Teh 2006). Therefore, SMAs are considered as the right candidate in shape control, flutter suppression, fatigue resistance, and vibration damping applications, utilizing the phase transformation of the alloy.

Past two decades, Nitinol (Ni-Ti) SMAs have been considered as actuators (in the form of fine wires) in the adaptive structure with prime importance, because of their superior properties, i.e., high strain recovery, better mechanical properties, biocompatibility, corrosion resistance, and thermal stability, though not feasible in real-time applications, because of slow response and degradation of shape memory effect after few functional cycles. Rapid response and long life of actuators are aimed at smart structures, dependent on transformation temperatures and thermal hysteresis. If the thermal hysteresis is wide, it takes a longer time for reverse phase transformation, and vice-versa leads to very slow response. However, overheating of the actuator causes degradation of shape memory effect and change in the properties of SMA. Ni-Ti SMAs possess transformation temperatures and hysteresis $< 100\text{ }^{\circ}\text{C}$ and $30\text{ }^{\circ}\text{C}$, respectively. The addition of Cu to Ni-Ti as a ternary element reduces the thermal hysteresis but lowers the transformation temperatures below to the room temperature.

1.2 LIMITATIONS OF STUDY

Besides the advantages of Ni-Ti and Ni-Ti-Cu SMAs, the fabrication and processing of SMAs are complicated and expensive. Melting of alloy and processing of actuators must be done in vacuum controlled atmosphere to avoid oxidation which deteriorates the characteristics and performance.

1.3 MOTIVATION

Literature unveils copper-based alloys, i.e., Cu-Zn and Cu-Al binary alloys too exhibit shape memory effect and pseudoelasticity. These SMAs are easy to fabricate and economical compared to the Ni-Ti group of SMAs. Addition of ternary element to Cu-Zn and Cu-Al alloys, i.e., Cu-Zn-Al, Cu-Al-Ni, Cu-Al-Mn, and Cu-Al-Be SMAs were developed (Horace and Norman 1970; Nickel 1957a; Otsuka and Shimizu 1970), and they exhibit good shape memory, strain recovery, pseudoelasticity, better damping and ease of modification of transformation temperatures made them as a strong alternative to Ni-Ti group SMAs. These features attracted and motivated to design a suitable and optimal elemental composition for the development of a novel Cu-Al based actuator with the desired and improved properties for flutter suppression/vibration isolation in smart structures.

1.4 ORGANIZATION OF THESIS

The purpose of this thesis is to design a suitable and optimal elemental composition for the development of a novel Cu-Al based actuator for smart structures to suppress/isolate the flutter in aerospace applications. To address the above, the thesis is composed of five chapters are as follows:

Chapter 1 introduces the background and limitations of the smart materials used in flutter suppression and motivation to design an optimal elemental composition for an actuator to meet the requirements.

Chapter 2 presents a comprehensive literature survey of smart materials and their types, characteristics of actuators, and the routes for modification/enhancement of properties viz. grain refinement, phase transformation temperatures, shape recovery, and mechanical properties. Further research gaps and the research objectives drawn from the study are presented.

Chapter 3 discusses the types of materials, methods, equipment, and methodology adopted in the present investigation to fabricate the alloys and their characterization.

Chapter 4 presents the results, interpretation, and discussion of the present research work.

Chapter 5. presents the conclusions drawn from the study and the recommendations for future work.

CHAPTER 2

LITERATURE SURVEY

2.1 INTRODUCTION

This chapter is concerned with the review of relevant literature. First, the literature on smart materials and shape memory alloys are reviewed. Second, the literature available on the improvement of grain refinement, mechanical properties, and shape memory characteristics is presented. Third, dependent phase transition temperatures on the alloying quaternary elements, elemental composition, and thermal treatments are presented. Finally, the literature on thermal hysteresis response is discussed. Further, based on the literature, the identification of the research problem and objectives of the research work are presented.

2.2 SMART MATERIALS

Smart materials are a new class of materials capable of sensing and responding to the change of its environment/external stimuli such as temperature, stress, light, magnetic, electrical, or chemicals. Smart materials are also known as responsive/intelligent/adaptive materials. These materials are of much interest in robotics, structural, biomedical, and aerospace industries (Dhanalakshmi et al. 2014; Kandagal and Venkatraman 2006; Oh et al. 2001; Suzuki and Kagawa 2010) for the improved performance of the system.

2.2.1 Types of smart materials

Smart materials are classified according to the kind of energy transformation and coupling between systems as shown in Figure 2.1

1. Type of energy transformation

- a. *Thermo-Mechanical*: Shape memory alloys.
- b. *Light-Mechanical*: Fibre optics.

- c. *Magneto-Mechanical*: Magnetostrictive materials, Magneto-Rheological fluids.
- d. *Electro-Mechanical*: Piezoelectric materials, Electrostrictive materials, Electro-Rheological fluids.

2. Types of Coupling

- a. *Direct coupling*: Either the mechanical or non-mechanical serves as the input, while the other serves as the output.
- b. *Indirect coupling*: Change in the electric field/magnetic field can indirectly coupled with mechanical behavior through a change in the viscosity of a fluid.

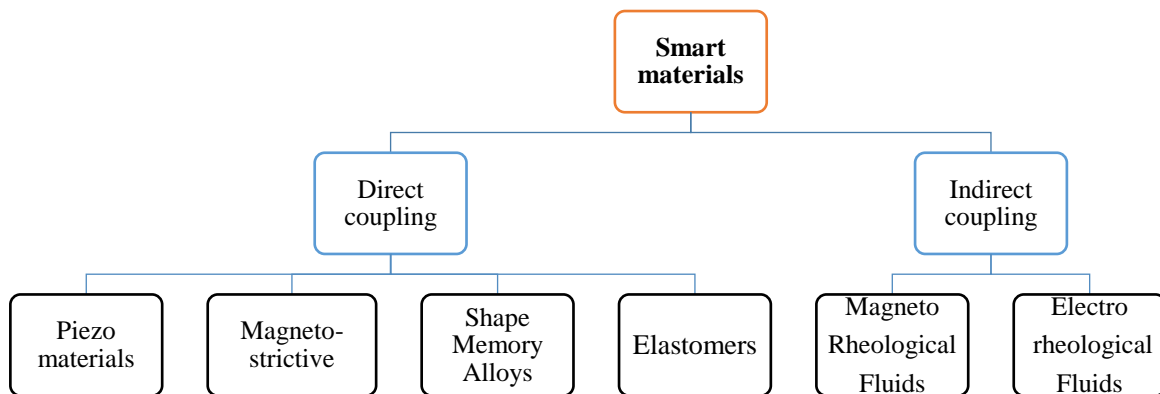


Figure 2.1 Smart Materials based on Energy Transformation

1. **Piezoelectric**: Piezoelectric materials undergo a mechanical change when it is subjected to a change in the electric/voltage field, and it is known as the piezoelectric effect. Piezo materials are also known as ferroelectric materials, *e.g.*, Lead Zirconate titanate, barium titanate, lithium niobate, and quartz
2. **Electro strictive**: Materials undergo a mechanical change when it is subjected to the square of the electric field and vice-versa, *e.g.*, Lead magnesium niobate(PMN), lead lanthanum zirconate titanate (PLZT) and Lead magnesium niobite -lead titanate (PMN-PT).
3. **Magneto strictive**: these materials change and induce mechanical strain, when it is subjected to a change in the magnetic field, *e.g.*, Fe-Al (Alfer), Fe-Ni, Co-Ni, Fe-Co, and ferrites.

4. **Shape Memory alloys:** Shape memory alloys (i.e., deformed material can be revert back to its original shape either by temperature gradient (shape memory effect) or load-removal (pseudoelasticity), e.g., Ni-Ti, Ni-Mn-Ga, Cu-Zn-Al, Cu-Al-Ni, Cu-Al-Mn, Cu-Al-Be, and Cu-Al-Fe.
5. **Elastomers:** Elastomers are also electroactive polymers made of dielectric materials undergo a change in physical state when it is subjected to change in the electric field. e.g., silicone, styrene-butadiene, etc.
6. **Rheological fluids:** Rheological fluids undergo a change in physical state when it is subjected to change in electric/magnetic fields. Change in the electric field is called Electrorheological fluids, and magnetic change is called Magnetorheological fluids.
e.g., Coal-water, Coal-oil.

2.3 SHAPE MEMORY ALLOYS

Shape memory alloys (SMA) are a group of materials possess a unique property, i.e., deformed material can be revert back to its original shape either by temperature gradient or load-removal (Duerig et al. 2013; Otsuka and Wayman 1999). Shape memory alloys undergo first-order, diffusionless crystallographic transition known as martensitic transition.

SMA's have two stable phases, i.e., austenite and martensite. The high-temperature phase is called the "austenite or parent phase" that has a face-centred cubic (FCC) crystal structure, and the low-temperature phase is called "martensite" has a crystal structure of body-centred cubic (BCC) in Ni-Ti and orthorhombic/Monoclinic in Cu-Al SMA's, as shown in Figure 2.2. Martensite is a relatively soft and twinned molecular structure; deforming/loading the twinned structure phase turns into a second form, i.e., detwinned structure. Austenite phase occurs at high temperatures, and it is the stronger phase of shape memory alloys. The start (s) and finish (f) temperatures of martensite (M) and Austenite (A) phases are represented by M_s , M_f , A_s and A_f , respectively.

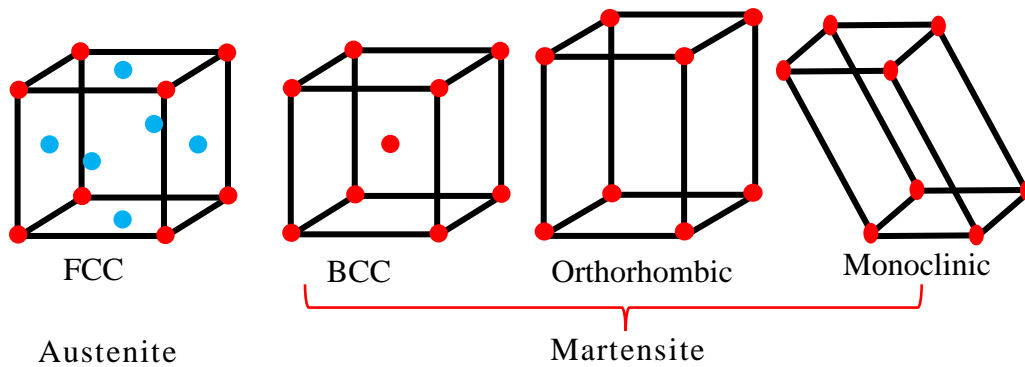


Figure 2.2 Phases and crystal structures

Shape memory alloys differ from conventional metals and alloys due to their unique properties, i.e., shape memory effect and pseudoelasticity, related with a crystallographically reversible martensitic phase transformation.

2.3.1 Shape memory effect (SME)

If the SMA quenched from the high-temperature phase, “austenite” to room/low-temperature forms the “martensite” phase in twinned structure. Applying load to twinned SMA transforms into a detwinned structure and heating the detwinned martensite above its austenite finish temperature reverts to the original phase (without residual strain) austenite is known as shape memory effect (Duerig et al. 2013).

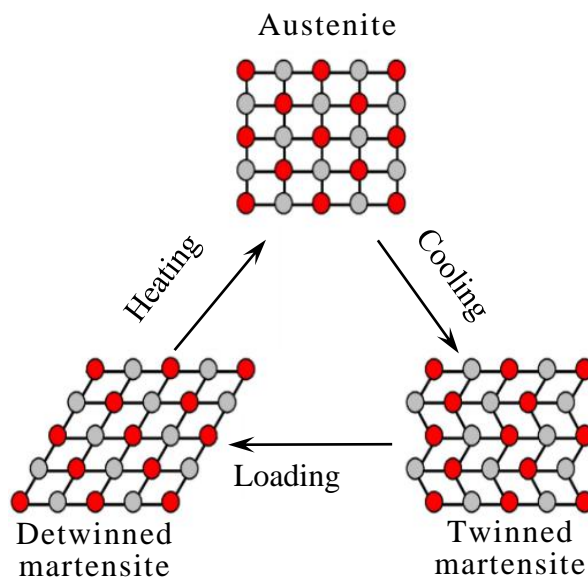


Figure 2.3 Shape Memory Effect

2.3.2 Pseudo-elasticity (PE)

If the alloy is loaded in austenite phase, it transforms to complete martensite and unloading reverts to original shape (austenite), and this is known as superelasticity or pseudo-elasticity (Duerig et al. 2013).

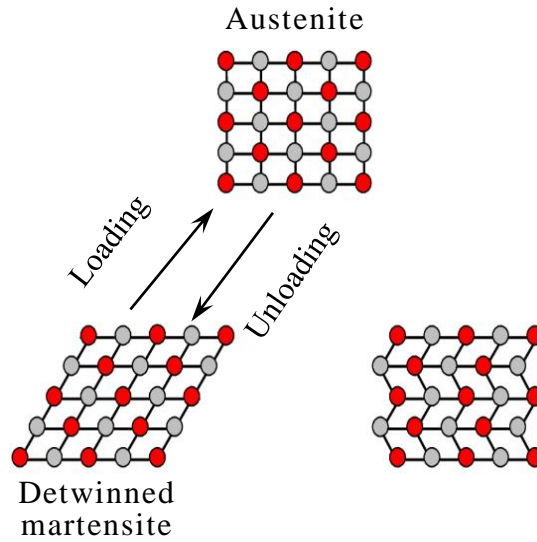


Figure 2.4 Pseudoelasticity.

2.4 TYPES OF SHAPE MEMORY ALLOYS

Shape memory alloys are classified according to the binary systems. Figure 2.5 illustrates the family tree of binary shape memory alloys and addition of a ternary element to the binary systems as shown in Figure 2.6

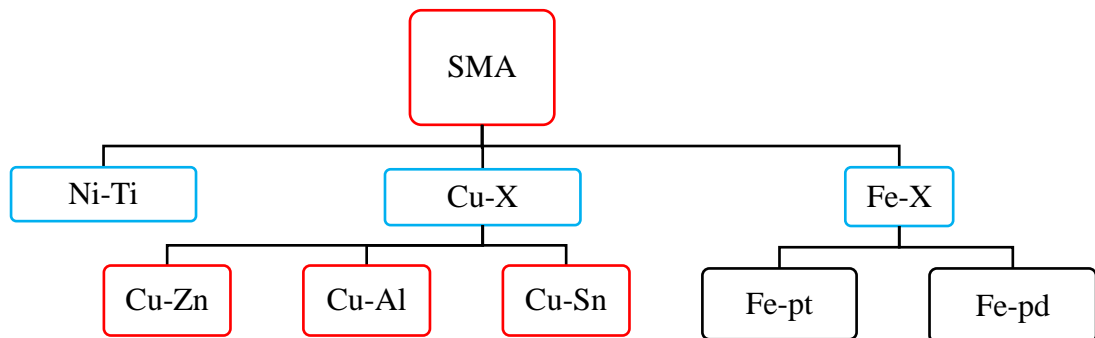


Figure 2.5 Types of SMAs.

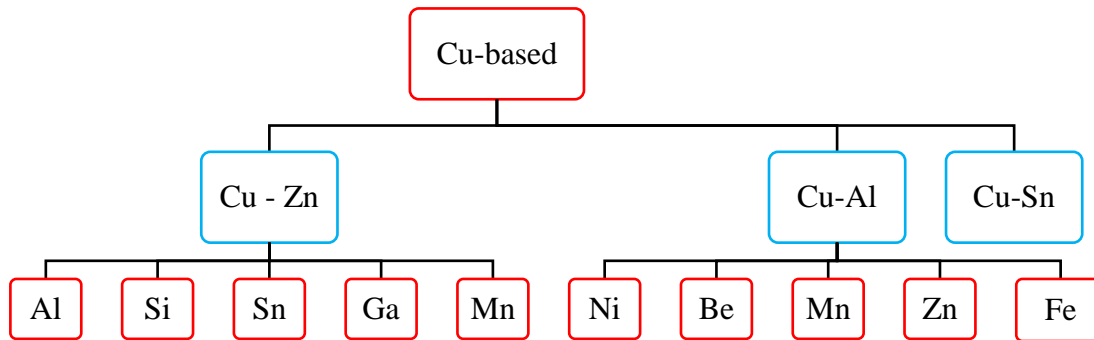


Figure 2.6 Types of Cu-based SMAs.

2.4.1 Ni-Ti

The origin of shape memory effect was found from the studies of Chang and Read in Au - 47.5 at% Cd alloy (Chang and Read 1951), followed by In-Tl alloy (Burkart and Read 1953) but these have not lead to any development due to lack of scientific interest. Buehler et al. (1961) discovered Nickel-Titanium SMA, and this was shortened as “Nitinol” derived from the combination of “Nickel –Titanium and in honor of Naval Ordnance Laboratories.” Nitinol SMAs exhibit good strain recovery and thermal stability. Researchers investigated the addition of ternary elements such as Cu, Zr, Hf, and Pd (Karaca et al. 2013; Olivier and Melton 1979; Ramaiah et al. 2013) to NiTi to improve the properties of SMA and observed good recoverable strains and functional life. Though the applications are limited because of difficulties in processing and expensive. An alternative to Ni-Ti-X based alloys, Cu based alloys were developed around, and from the 1960s by the addition of binary and ternary element and the classification these alloys are presented in Figure 2.6, and these are discussed in brief in the proceeding sections:

2.4.2 Cu-Zn-Al

Cu-Zn-Al alloys were the first Cu-based SMAs developed as an alternative to Ni-Ti because of inexpensive raw material and ease of production with the conventional melting apparatus. Horce et al. (1970) investigated the addition of Al to the β phase Cu-Zn alloy to validate the property of pseudoelasticity.

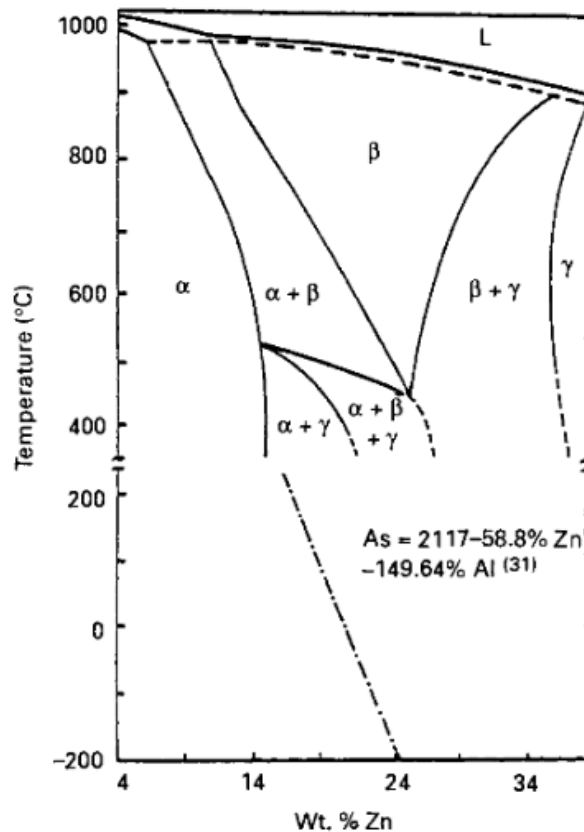


Figure 2.7 Pseudo binary Cu-Zn phase diagram. (Duerig et al. 2013)

Researchers (Guilemany and Gil 1990; Perkins 1974) developed and investigated SME/PE properties of Cu-Zn-Al SMAs by varying the elemental compositions, i.e., 62 - 86 % Cu, 10 - 28 wt.% Zn, and 3 - 10 wt.% Al, yields transformation temperatures in the range of -100 °C to + 100 °C. It is noticed that the increase in both Al and Zn decreases the transformation temperatures. Figure 2.7 presents the pseudo-binary phase diagram of Cu-Zn-Al at 6 wt.% of Al, and the alloys containing around 70 wt.% of Cu, 25 wt.% of Zn and 6 wt.% of Al have the martensite transformation temperatures near to room temperature and exhibits good SME. Though Cu-Zn-Al alloys exhibit good SME, the prime limitations of these alloys are coarse grains (Melton and Mercier 1979) leads to intergranular failure, susceptible to martensite stabilization at room temperature alters/varies the transformation temperatures and increases the thermal hysteresis (Cook and Brown 1978; DELAEY et al. 1984; Li and Ansell 1983), generates substructure dislocations (Perkins and Muesing 1983) with thermal cycling (Bujoreanu et al. 2011) limits repeatability of the phase

transformation, and the structure decomposes above the usage of 100 °C. As a result, the degradation of shape memory effect (SME) was noticed in Cu-Zn-Al which was ascribed to the high temperature stabilization of martensite.

2.4.3 Cu-Al

Greinger (1939) had noticed the martensite transformation in Cu-Al binary alloys, and Nagasawa et al. (1971) found SME in Cu-Al alloy containing 25 at.% Al, but not practically applicable due to the higher transformation temperatures, i.e., above 300 °C, and the formation of γ_2 (Cu_9Al_4) cubic intermetallic precipitate particles embrittle the alloy, as shown in Figure 2.8.

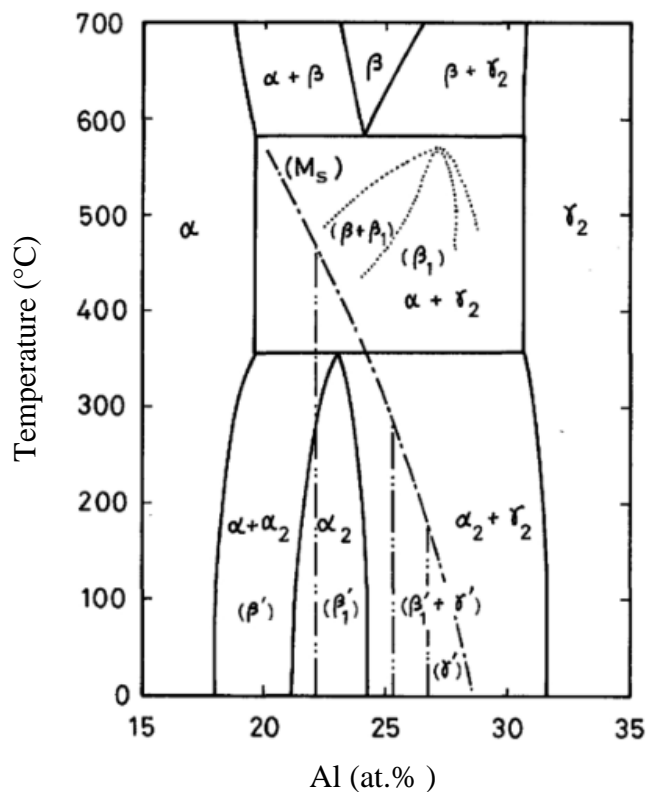


Figure 2.8 Cu – Al phase diagram (Noriyuki et al. 1977)

It is known that water quenching of a Cu-Al binary alloy could not completely prevent β and its ordered phase β_1 from decomposition to stable phases. Therefore, an element, such as Ni, Zn, and Mn was added into Cu-Al binary alloys as a third element to stabilize β and β_1 . and improving the shape memory properties and the literature is as follows:

2.4.4 Cu-Al-Ni

Addition of Ni to Cu-Al alloy efficiently slows down the diffusion of Cu and Al and suppresses the formation of γ_2 particles (Duerig et al. 2013; Lojen et al. 2005) and also observed the shift in the domain of the β phase to higher Al concentrations, as shown in Figure 2.9. Kurdjumov et al. (1949) investigated martensitic transformation in β Cu-Al alloys with the addition of Ni, and observed complete transformation without hysteresis in the range of -10 to 35 °C, and not lead to any development till 1970. For the first time, Otsuka et al. (1970) observed SME in Cu-14.2Al - 4.3Ni polycrystalline alloy, and the transformation temperatures lie around room temperature.

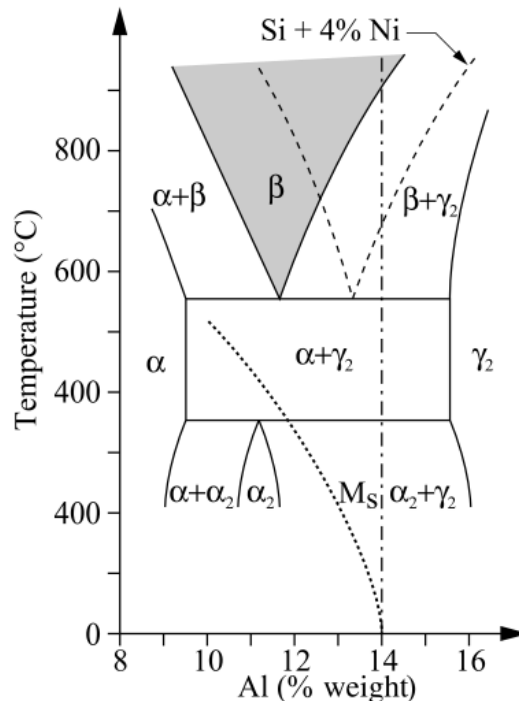


Figure 2.9 Pseudo binary Cu-Al-Ni phase diagram (Lexcelent 2013)

Researchers (Shimizu et al. 1978) (Agafonov et al. 1988) (Recarte et al. 2002) (Recarte et al. 2004) investigated Cu-Al-Ni SMAs by varying Al from 13 - 14.5 wt.% and 3 – 4.5 wt.% of Ni yields transformation temperatures from -150 to 250 °C. Cu-Al-Ni SMAs exhibits good SME and highest strain recovery with lower wt.% of Al and Ni, but the higher transformation temperatures limit the applications. Cu-Al-Ni SMAs with 14.5 ± 1 wt.% of Al and 3.5 ± 1 wt.% Ni exhibits transformation temperatures around the room temperature, but these alloys are not extensively used in applications

because of the increase in concentration of Al and Ni forms γ_2 particles at the grain boundaries embrittles the alloy and prevents martensite transformation. It is also observed all the ternary alloys possess coarse grains causes intergranular failure without the formation of second phase precipitates.

2.4.5 Cu-Al-Mn

The addition of Mn acted as a stabilizing element for the β and β_1 phase in Cu-Al alloy and also observed a shift in the domain of the β phase to lower concentration of Al, as shown in Figure 2.10. Alloying Mn lowers the eutectoid decomposition temperature to 410°C and suggests that the β phase in Cu-Al-Mn alloys might be more stable to diffusional decomposition than other copper-based alloys. Thus, it creates an interest in Cu-Al-Mn alloys.

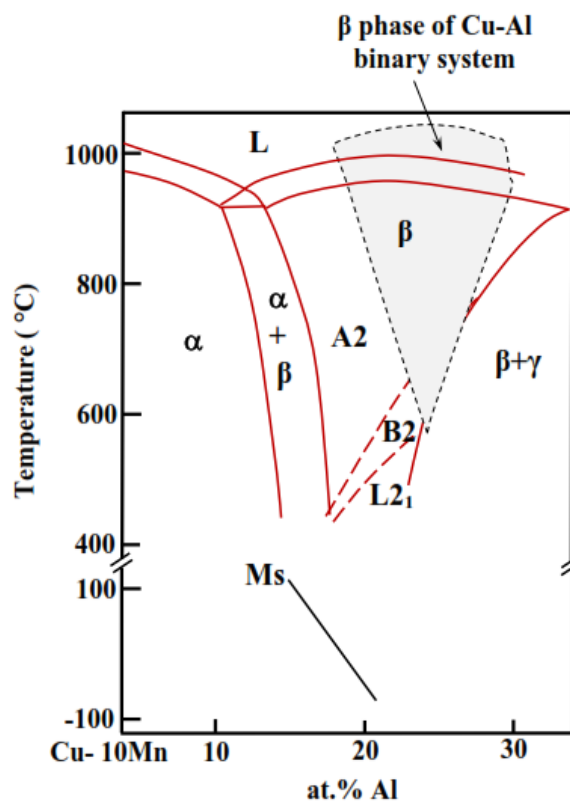


Figure 2.10 Pseudo binary phase diagram of Cu-Al-Mn (Sutou et al. 2001)

West et al. (1956) initially investigated the martensitic transformations on Cu-Al-Mn alloys and extended by Koster et al. (1966). Matushita et al. (1985) noticed manganese had a significant effect in improving the ductility of Cu-Al alloys. Lopez

Del Castillo et al. (1986, 1987), Blazquez et al. (1989), Bublei et al. (1990) and Zak et al. (1996) investigated the effect of variation in wt.% of Al and Mn in the range of 10 – 14 wt.% of Al and 1 – 12 wt.% of Mn on the martensitic transformations and transformation temperatures of Cu-Al-Mn alloys. From the investigations, the results revealed that the M_s temperature of Cu Al-Mn alloys became lower than that of Cu Al binary alloys with the addition of Al and Mn. Matushita et al. (1985) observed manganese lowered the M_s temperature of Cu-Al-Mn alloys by about 30 K per 1 wt% Mn and prevented precipitation of stable phases from the supercooled β phase, and the alloys yield transformation temperatures in the range of $-200\text{ }^\circ\text{C}$ to $+200\text{ }^\circ\text{C}$. Polycrystalline Cu-Al-Mn SMAs with higher Al contents with the β_2 or β_1 ordered structure are too brittle for cold working and possess very low fatigue strengths. The reason for the brittleness in polycrystalline alloys of these systems is generally attributed to large grain size, high degree of elastic anisotropy, and the grain boundary segregation of impurities (Dasgupta et al. 2018; Jain et al. 2016; Kainuma et al. 1996).

Kainuma et al. (1996) found that ductility can be improved by lowering the wt.% of Al in alloys (i.e., 8 – 9 wt.%) by decreasing the degree-of-order, and these alloys have higher transformation temperatures. An increase in the content of manganese $> 10\%$ or more, changes the type of ordering of the β' -phase, namely, DO3 is replaced by B2, results in maximum disordering ($\alpha = 0.5$) causes no shape recovery.

2.4.6 Cu-Al-Be

Nickel (1957) reported that the β phase region of the Cu-Al binary alloy system was extended to the lower Al side by the addition of Be. Prawdzik et al. (1966) have reported that the addition of Beryllium (Be) to the Cu-Al binary system decreases the transformation temperatures extremely to the room temperature or below. Higuchi et al. (1982) investigated the relationship between transformation temperatures and the element composition. They observed that the addition of 0.1 wt. % Be to the Cu-Al SMA lowers the phase transformation temperatures by $100\text{ }^\circ\text{C}$. This feature allows preceding alloy towards intermediate and low-temperature actuator applications. Belkahla et al. (1993;1991) studied the addition of beryllium in a small proportion modifies the equilibrium diagram for Cu-Al, the temperature of the eutectoid plateau is reduced, as shown in Figure 2.11. The addition of a small concentration of beryllium to

the eutectoid alloy close to Cu_3Al leads to a sharp decrease in the martensitic transformation temperatures. The eutectoidal temperature is lowered, but the temperature of β solution treatment remains the same, and above all, the curve of the transformation temperatures is brought down. Unlike the effect of nickel, beryllium in a low concentration does not affect the composition or the temperature of the time-temperature-transformation (TTT) diagram.

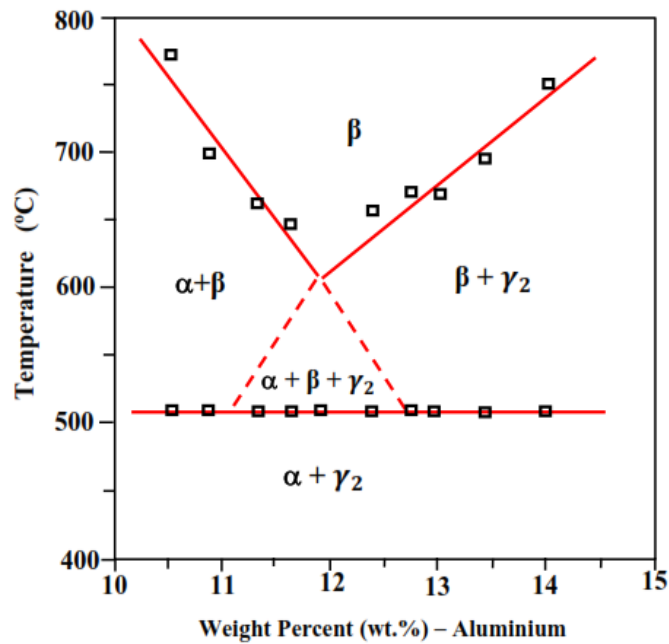


Figure 2.11 Quasi binary phase diagram of Cu-Al-Be.

(Belkahla et al. 1993)

However, utilization of Cu-Al-Be alloys is limited to single-cycle applications, due to the coarse grain size (Hsu et al. 2009; Montecinos 2015), high brittleness, intercrystalline failure, poor cold-workability, low thermal stability (Dunne et al. 2006), high elastic anisotropy (Xu et al. 2011) and short life cycle (Kustov et al. 2004a) (Balo and Ceylan 2002).

It is observed from the literature, Cu-Zn-Al, Cu-Al-Ni, Cu-Al-Mn, and Cu-Al-Be SMAs possess coarse grains that cause rapid failure in applications. To overcome the limitations, researchers have investigated various techniques to improve the ductility and shape memory properties of the alloy.

2.5 GRAIN REFINEMENT

As literature presents, the prime limitation of Cu-based SMAs is intergranular/brittle failure, attributes to coarse grains. Refinement of grains and increasing the grain boundary suppresses the brittle failure and improves ductility. Researchers investigated various routes for the refinement of grains, such as alloying/inoculation of grain refiners, thermal treatments *viz.* annealing at various temperatures and durations, quenching media, and advanced secondary processing routes *viz.* severe plastic deformation and melt spinning.

2.5.1 Grain Refiners

2.5.1.1 Boron

Boron attracts attention in grain refinement and plays as an effective grain refiner for Cu (Lozovoi and Paxton 2008), Mg (Suresh et al. 2009), Al (Wang et al. 2011), Cu-Al (Birol 2012) systems because of its advantages like small atomic radius, i.e., which acts as either substitutional or interstitial solid solution element, and de-embrittle element which enhances the cohesive strength of grain boundaries (Balart et al. 2016) and very small lattice disregistry. Boron combines with other metals to form metal borides such as AlB_2 , TiB_2 , and ZrB_2 forms nucleation sites in enhancing grain refinement.

Cu-Al alloys can be effectively grain refined with minimal addition, i.e., 0.02 – 0.05 wt.% of B with improved mechanical properties (Davis and Committee 2001) due to the lower lattice disregistry. Dong et al. (1994) (2002) investigated shape memory capacity and life of Cu-Al-Be alloy with addition of B, and noticed complete restoration in the water-quenched condition, whereas small residual deformation in the air-cooled condition, and there is no discussion on grain size refinement and mechanism. Zhang et al. (2009, 2010, 2011) studied the effect of boron and ECAP for grain refinement of Cu - 11.42 Al - 0.35 Be - 0.18 B alloy. After 8 passes of ECAP, grain size reduces to 2 μm with uniform distribution of precipitated phases, with the reduction in ultimate strength and strain. The shape recovery ratio of fine-grained Cu–Al–Be–B SMA was not better than that of the as-cast alloy. Lee et al. (1986a) investigated the addition of various borides to Cu-Zn-Al SMA and noticed good grain refinement with the AlB_2 compared to others. Bohong et al. (1991) observed

improvement in shape recovery of Cu–Zn–Al SMA with the addition of B. Sampath (2006a) didn't notice martensitic transformation with the addition of 0.2 wt.% of B, due to the formation of bulky precipitates inhibits the formation of martensite variants. Sutou (2006) and Koeda et al. (2005) observed the addition of B increases the damping efficiency of Cu-Al-Mn alloys. Sampath et al. (2009a) studied the effect of Boron (B) with Cu-Al-Mn and observed effective grain refinement with a reduction of about 80% in grain size with an increase in transformation temperatures. Sampath et al. (2015; 2009b) and Aydogdu (2016) observed good refinement with a decrease in SME and SE, with the addition of B to Cu-Al-Mn alloys.

Zhang et al. (2019) investigated different contents of boron (0.25 - 2.0 wt%) on Cu-13.0Al-4.0Ni alloy and observed that the microstructure and the shape memory effect were sensitive to the addition of boron, and the addition of boron enhanced the mechanical properties, but also greatly improved the shape memory effect of the alloy. Hussain et al. (2019) observed improvement in ductility more than four times than that of the base alloy Cu-Al-Ni. Besides, shape memory properties also improved significantly.

2.5.1.2 Chromium

Sutou et al. (1999) and Mallik et al. (2009) investigated addition of 0.5 – 2.0 and 0.9 – 3.0 wt.% of Cr, respectively, to Cu-Al-Mn alloy and observed refinement with fine precipitates in the parent β phase matrix due to the low solubility of Cr in the matrix. Candido et al. (2012) had carried out microstructural and mechanical tests on Cu-Al-Be alloy with chromium as a grain refiner, and the microscopic studies reveal that the grain size decreases to 100 μm from 1950 μm for 0.5 wt.% and 0 wt.%, respectively. Further, their investigation resulted in alloying with 0.2 wt. % of Cr exhibited higher tensile stress-strain and also the low martensitic transformation temperatures suitable for low temp applications. Dasgupta et al. (2015) studied the addition of 0.185 wt.% of Cr to Cu-Al-Mn alloy and observed that formation of complete martensite without precipitation.

2.5.1.3 Manganese

Sari (2010) observed a reduction of grain size from 1400 μm to 350 μm with the addition of 2.5 wt.% of Mn by the inhibiting effect on grain boundaries and observed an increase in ductility. Akash et al. (2018) observed an increase in the lifetime of morphs with the addition of 5 wt.% of Mn. Masamichi et al. (1989) observed no grain refinement with the addition of 0.1 - 1.0 wt.% of Mn and an increase in the super plasticity by suppressing the deteriorious O and S atoms at the grain boundaries. Morris et al. (1994) observed an improvement in thermoelastic and pseudoelastic properties with the addition of various wt.% of Mn. Saud et al. (2014c) studied the effect of Mn on Cu-Al-Ni alloys, observed an increase in ductility from 1.3 % to 3.6% with the addition of 0.7 wt.% of Mn.

2.5.1.4 Nickel, Niobium

Melo et al. (2009) Albuquerque et al. (2010a) (2010b) examined addition of Nickel and Niobium, observed that reduction in grain size from 1.5 mm to 200 μm , 1950 μm to 100.77 μm and an increase in strength from 350 to 750 Mpa and elongation from 6.9% to 8.2%. The strengthening effect is due to the formation of Nb rich precipitates which inhibits the grain growth. Santiago et al. (2019) studied the addition of Ni-Nb master alloy to Cu-Al-Be alloy and observed improvement in grain refinement with an increase in wt.% of the refiner.

2.5.1.5 Silver

Safaa et al. (2014b; a) studied influence of silver on the mechanical properties of Cu-Al-Ni shape memory alloys and observed that tensile strength, elongation, fracture stress-strain, yield strength are improved by the formation of AlAg_3 and AgAl_3 precipitates, and the shape memory effect and recovery ratio also improved.

2.5.1.6 Zirconium

Gil et al. (1999) studied the effect of Co, Mn, Si, and Zr grain refiners on kinetic growth of grains in Cu-Zn-Al alloys, subjected to different isothermic treatments. They observed that the growth exponent of Zr doped alloy is very low compared to other refiners. Matsuoka et al. (1983) and Lee et al. (1986b) examined the addition of Zr and Ti to Cu-Al-Ni alloys, discerned fine grain refinement and improved ductility with Zr

compared to Ti and increase in Ms temperatures with the increase in Zr content. Lee et al. (1986a) probed the effect of Zr on Cu-Zn-Al alloys and found that the maximum reduction in grain size for Zr doped alloys, without any modification in the shape memory effect. The influence of Zr doped Cu-Al-Ni alloy has been reported by Kim et al. (1990) and Roh et al. (1991), and the results unveil that refined grain with a significant increase in fracture strength and fracture strain. They also observed that the maximum shape recovery of 95 % occurred at 3 % strain, and decreases with an increase in the percentage of strains. Bhattacharya et al. (1993a) observed significant grain refinement with the doping of Zr. Hsu et al. (1996) investigated superplastic forming behavior on Cu-Zn-Al alloy with Zr and observed that the grain size decreases as annealing temperature lowers. Sampath et al. investigated the effect of Zr on Cu-Al-Ni (Sampath 2005), Cu-Zn-Al (Sampath 2006), and Cu-Al-Mn (2009a) alloys, noticed a significant improvement in grain refinement, ductility, and hardness with increase in wt.% of Zr, except in Cu-Al-Mn alloys. Shape recovery studies of the Zr doped alloys exhibit an increase in the percentages of shape recovery for Cu-Zn-Al. In contrast, it decreases in Cu-Al-Mn alloys, attributes to the relation between the size and width of martensite variants and its reorientation. Yang et al. (2016a) examined the effect of CuZr inoculant on Cu-Al-Mn alloy and discerned improved properties with the doping of inoculant.

2.5.1.7 Rare earth elements (REE)

Bhattacharya et al. (1993b) observed the addition of smaller amounts of mischmetal and yttrium reduces the coarsening of grains. The addition of rare earth metals reduces the grain size significantly, compared with transition metals. Liu (2007a; b) studied the effect of Dy and Y on properties of Ni-Ti shape memory alloy and observed the formation of secondary phases and increases with increase in addition, and also increase in transformation temperatures. Lu et al. (2009) studied the doping of Ce to Cu-Al-Mn SMA and observed Ce doping refines the grains and enhances the tensile strength, ductility, and damping. Yang et al. (2009) observed that the addition of Misch metal works effectively in the transformation from intergranular to ductile fracture attributes to fine grain refinement of Cu-Zn-Al. Xu et al. (2008a) studied 0.04

– 0.2 wt% of Gd in Cu-26Zn – 4Al (wt%) and observed a significant effect on grain refinement.

2.5.2 Thermal treatments

Thermal treatment, i.e., betatization/annealing, is another method to modify grain size, and the properties of shape memory alloys by several researchers and associated literature is as follows:

Adnyana et al. (1986) observed an increase in grain size with an increase in temperature and duration of solution treatment. Lee et al. (1986b) investigated the effect of solution treatment temperatures along with the addition of grain refiners and observed an increase in grain size with the increase in solution treatment. Lai et al. (1996) observed smaller grain sizes with lesser vacancy concentration for a shorter duration of betatization, i.e., 10 min. Gil et al. (1993;1991) observed an increase in grain size with an increase in temperature and duration. Wang et al. (2006) observed that the alloys predominantly consist of twins at relatively higher quenching temperature (T_q), but the content of twins gradually decreases as T_q decreases until completely disappearing at 700 °C quenching. With the further decrease of T_q , i.e., at 600 °C quenching, even no martensite can be seen. Montecinos et al. (2008) investigated the solution treatment of cylindrical, flat, and tensile specimens at various durations, i.e., 0 – 15min, and observed an increase in grain size with an increase in duration. Cylindrical specimens exhibit smaller grain sizes compared to other types. Zhang et al. (2009) studied two groups of Cu–Al–Bi–B specimens that were reheated to a certain temperature and followed with oil-quenching. One group of specimens held for 10 min at various reheating temperatures (T), where T=623, 673, 723, 773, 823, 873, 923, and 973 K, respectively. Other groups of specimens were held at 873 K with different time (t), where t=10, 20, 30, 40, 50, and 70 min, respectively. It was shown that the microstructure did not change significantly after quenching below 873 K, while the grain sizes were smaller than 50 μm after quenching at 873 K, and individual grain coarsening occurred above 923 K. Grains become bigger and inhomogeneous with the holding time more than 30 min. Therefore, the suitable procedure was considered for heating at 873 K holding for 10–30 min, followed by oil-cooling.

Montecinos et al. (2012) obtained an increase in grain size with an increase in the duration of betatization of samples at 800 °C. Canbay et al. (2013) studied the effect of annealing temperatures, i.e., 700 – 850 °C for 1 hour, and observed an increase in grain sizes with an increase in temperatures. Grain boundaries are not visible in the high solution treated samples. Haidar et al. (2018) investigated Cu-Al-Ni-Co SMAs at annealing temperatures of 400 and 500 C for 1hr and 3 hrs and observed that addition of cobalt, forms a new phase formed in the matrix on the needle-like and plate-like, which is typically known as γ_2 phase precipitates are Co rich, which is the combination of Co, Ni, and Al formed $Al_5Co_{22}Ni_3$, and the precipitates increased with increasing time.

2.5.3 Severe plastic deformation - Equal channel angular pressing (ECAP)

Several plastic deformation techniques are advanced secondary processing routes in the refinement of grain size to improve the mechanical properties, and the literature is as follows:

Zhang et al. (2009, 2010, 2011) have examined ECAP on Cu - 11.42 Al - 0.35 Be - 0.18 B alloy, apprehended grain size refined from 300 to 2 μ m with ultimate strength 460MPa and 2.7% elongation after eight passes. The shape recovery ratio of fine-grained Cu–Al–Be–B SMA was poor than as-cast alloy. However, after 20 thermal cycles, the fine-grained alloy possessed much better stability because the grain boundaries were purified, and the phase was refined. Moghaddam et al. (2014, 2017) studied the effect of accumulative roll bonding and equal channel rolling and post deformation annealing on two different Cu-Al-Mn SMAs. It is observed that after 5 ARB passes and subsequent annealing followed by water-quenching forms, thermoelastic martensite phase with refined grains with a strength of 780 MPa and 11% elongation with deeper dimples. The bonding quality of the interfaces improved significantly during the subsequent passes. For both alloys, transformation temperatures decreased after post-deformation annealing as a result of the increase in the elastic stored energy and the decrease in its dissipation. For the ECARed specimens, controlling annealing time at 890 °C led to the coexistence of bainitic and martensitic phases, which had superior mechanical strength. Severe plastic deformation techniques are highly impractical for bulk alloys (Zhang et al. 2009).

2.6 TRANSITION TEMPERATURES

Phase transition temperatures play a vital role in the selection/application of shape memory alloy in the requisite zone. The literature presents alloying quaternary element improves ductility, whereas the element modifies the transition temperatures, and also varying thermal treatment increases/decreases the phase transition temperatures, and the literature is as presented below:

2.6.1 Alloying elements

Higuchi et al. (1982) and Belkhala et al. (1993) observed variation in the transformation temperatures with the variation in the elemental composition of Cu, Al, and Be elements. Melo et al. (2009) observed the addition of Ni and Nb forms Nb rich precipitates increases the transformation temperatures. Mallik et al. (2009) investigated the addition of 0.9 – 3.0 wt.% Cr to Cu-Al-Mn alloy and observed a decrease in transformation temperatures about 15 °C with the addition of Cr as they tend to form fine precipitates of Cu_2CrAl , Cr_3Al . Huaping et al. (2011) and Xu et al. (2011) studied the effect of Ni and observed that the addition of Ni decreases the transformation temperatures compared to Ni and Be alone to Cu-Al alloy. Karagoz et al. (2013) and Canbay et al. (2014) investigated the effect of mass percentage of the alloying element on the transition temperature of Cu-Al-Ni and Cu-Al-Mn alloys respectively and observed that transformation temperatures could be controlled by varying wt. % of alloying elements in the alloy. Canbay et al. (2014) investigated the effects of vanadium (V), and cadmium (Cd) on transformation temperatures of Cu–Al–Mn shape memory alloy and observed that the addition of the V and Cd decreases the characteristic transformation temperatures. It was found that the Cd is more efficient than that of V. Santiago et al. (2019) studied the addition of Ni-Nb master alloy to Cu-Al-Be alloy and observed a decrease in transformation temperatures with increase in refiner. Sari (2010) addition of Mn decreases the transformation temperatures. Saud et al. (2014c) observed an increase in the transformation temperatures upto 0.7 wt.% of Mn and then decreases with increase. Yang et al. (2017) noticed decrease in the reversible martensitic transformation temperatures of Cu–Al–Mn SMAs with the increases both in the Mn and Al contents. The Cr addition in Cu–Al–Mn alloys also decreases the transformation temperatures with a lower rate than the effects of Mn or Al contents.

2.6.2 Effect of thermal treatments

Transformation temperatures and the thermal hysteresis can be modified by the variations in the thermal treatments, i.e., duration and temperatures of betatization/solution annealing by several researchers and literature is as follows:

Adnyana (1986) and Duerig et al. (2013) observed an increase in transformation temperatures with an increase in solution treatment/betatization temperature and duration. Jiao et al. (2010) reports the effect of solution treatment on the damping capacity and shape memory effect in a Cu-Al-Mn alloy at different temperatures for a constant period and observed that the shape memory effect increased with increasing the solution temperature.

2.7 RESPONSE - THERMAL HYSTERESIS

Huang et al. (2002) investigated the selection of shape memory alloys for actuator applications based on performance parameters such as transformation hysteresis, actuation stress, and strain, output work, heating and cooling speed, energy efficiency, damping and cost and presented hysteresis gap should be small for faster response because of slight temperature variation. Actuators with higher transformation temperatures, i.e., $A_f > 200$ °C require larger current for rapid actuation, whereas the cooling cycle takes more time compared to heating. Also, overheating SMA causes thermal fatigue, which hinders the function and reduces the life of the actuator. Mercier et al. (1979) noticed the reduction of thermal hysteresis in Ni-Ti by the addition of Cu replacing Ni. Tadesse et al. (2010) suggested a reduction in the cooling cycle improves the response of an actuator related to variation in the phase transformation temperatures. This is a significant improvement in the actuation capability of SMAs. Atli et al. (2010) observed that microalloying of Scandium to $Ti_{50.5} Ni_{24.5} Pd_{25}$ alloy displays a more stable shape memory response with smaller irrecoverable strain and narrower thermal hysteresis than the baseline ternary alloy. Bigelow et al. (2010) investigated and presented that addition and increase in wt.% of Pd to Ni-Ti narrows the thermal hysteresis. The addition of Hf/Zr widens the thermal hysteresis in Ni-Ti alloys in the range of 35-70 °C (Ramaiah et al. 2014).

2.8 IDENTIFICATION OF THE PROBLEM

The rapid response of actuators is much needed in suppressing the flutter/vibration of aerospace structures, depends on narrow thermal hysteresis. Along with narrow hysteresis, moderate transformation temperatures, longer functional life, and good mechanical properties are prime requisites in the application. All these properties required for the application of SMA actuators depends on the elemental composition and thermal treatments used in the processing of alloys.

All the ternary Cu-based SMAs fail rapidly in the application due to the coarse grains. Addition of grain refiners (i.e., B, Cr, Ni, Ti, Zr, Mn, and REE, etc.) and different betatization treatment modifies the grains, transformation temperatures, and also phases of the ternary alloys. It is observed that the same refiner behaves differently in two different ternary alloys depends on metal properties and treatments.

Among the class of Cu-based SMAs, these alloy actuators are restricted their usage in real-time applications because; (i) Cu-Zn-Al SMAs undergoes martensite stabilization at room temperature, (ii) Cu-Al-Ni SMAs fails brittle due to the secondary phase precipitates at the grain boundaries, and also higher transformation temperatures requires higher actuation currents (iii) Cu-Al-Mn SMAs possess high transformation temperatures owing to lower wt.% of Al.

2.9 RESEARCH GAPS

From the literature survey, it is learned that minor addition, i.e., 0.1 wt.% of beryllium to Cu-Al alloys, lowers the transformation temperatures by 100 °C and Cu-Al-Be SMA possesses excellent thermal stability, damping property and shape memory property in pseudo-elastic (SIM) applications. This has motivated us to investigate the quaternary addition to Cu-Al-Be shape memory alloys to improve the ductility, shape recovery, moderate transformation temperatures with narrow thermal hysteresis.

2.10 OBJECTIVES

The objectives of the present research work drawn from the study are as follows:

1. To investigate the effect of the elemental composition of Cu, Al, and Be on the microstructural, mechanical, and shape memory properties of SMA.
2. To investigate the effect of grain refiners boron and zirconium on the microstructural, mechanical, and shape memory properties of SMA.
3. To investigate the effect of rare earth elements (REE) cerium and gadolinium on the microstructural, mechanical, and shape memory properties of SMA.
4. To investigate the effect of manganese on the microstructural, mechanical, and shape memory properties of SMA.

2.11 CLOSURE

This chapter reported the comprehensive literature review on the smart materials and shape memory alloys. In addition, the literature related to the improvement of grain refinement, mechanical properties, phase transition temperatures, shape memory characteristics and narrow thermal hysteresis were presented. The proceeding chapter discusses the details of metals and elemental composition used in the investigation. Methodology for the preparation of alloys and the standards used for material characterizations are presented.

CHAPTER 3

MATERIALS AND METHODS

3.1 INTRODUCTION

This chapter discusses the details of metals and their range of elemental composition used in the investigation and methodology for the preparation of alloys/specimens in the three sections. First, the metals and their purity, and the preparation of master alloys have been discussed. Second, the methodology for the preparation of shape memory alloys and the specimens for characterization studies. Finally, the procedures and standards used for XRD, microstructure, morphology, grain size, shape recovery, and uniaxial tensile test studies are presented.

3.2 ELEMENTAL COMPOSITIONS

In the present investigation, Cu-Al-Be SMAs are selected as the nominal /base alloy. Alloys are investigated in between hypoeutectoid and hypereutectoid alloys, and to improve the grain refinement boron, zirconium, and rare earth elements *viz.* cerium and gadolinium are selected as grain refiners. To improve the ductility manganese is chosen as the quaternary element. The elemental composition range of the elements used to prepare the alloys are presented in Table 3.1.

Table 3.1 Elements and its range used in the investigation.

S.No	Metal	Range (wt.%)
1.	Copper (Cu)	Remaining
2.	Aluminium (Al)	11.00 - 12.00
3.	Beryllium (Be)	0.40 - 0.44
4.	Boron (B)	0.02 - 0.15
5.	Cerium (Ce)	0.05 - 0.20
6.	Gadolinium (Gd)	0.05 - 0.15
7.	Manganese (Mn)	0.10 - 1.00
8.	Zirconium (Zr)	0.05 - 0.40

3.3 METALS AND PURITY

The raw materials used in the present investigation are copper, aluminium and the master alloys, CuBe_4 , CuB_2 , Cu_9Gd_2 , CuMn_{30} , and $\text{Cu}_{51}\text{Zr}_{14}$ are as shown in Figures. 3.1-3.6. Master alloys were prepared using a vacuum arc remelting machine (Make: Edmund Buhler GmbH, Model: AM/0.5) in the form of small buttons and remelted for six times to ensure homogenized mixture and sliced into granules. Table 3.2 presents the purity of raw materials.

Table 3.2 Type of metals and their purity.

S. No	Metals	Purity (%)
1.	Copper	99.95%
2.	Aluminium	99.90 %
3.	Copper Beryllium - CuBe_4	99.99 %
4.	Copper Boron - CuB_2	99.99 %
5.	Copper Manganese – CuMn_{30}	99.99 %
6.	Copper Zirconium – $\text{Cu}_{51}\text{Zr}_{14}$	99.99 %
7.	Copper Gadolinium – Cu_9Gd_2	99.99 %
8.	Cerium	99.50 %

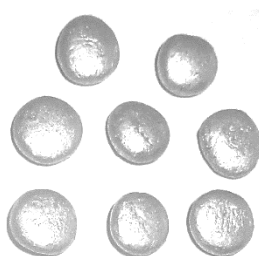


Figure 3.1 Aluminium buttons.

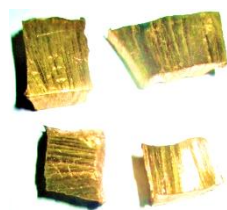


Figure 3.2 CuBe_4 master alloy.

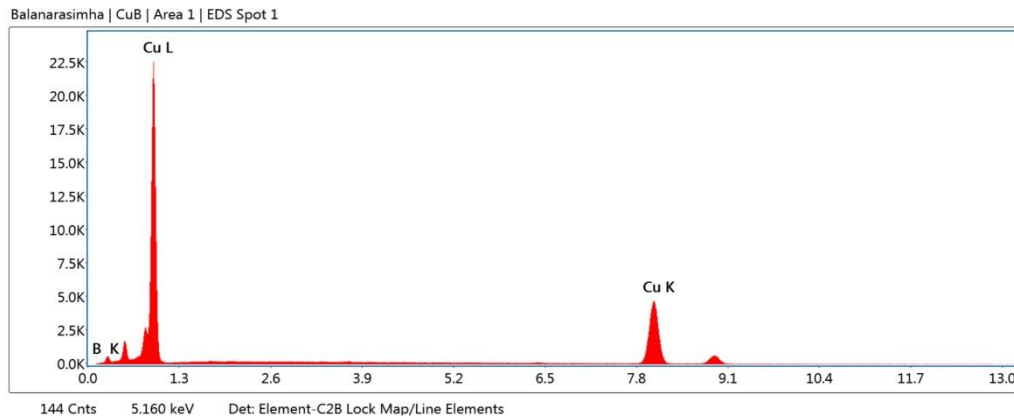


Figure 3.3 a) Photograph of CuB_2 Inoculant b) EDS of CuB_2 Inoculant

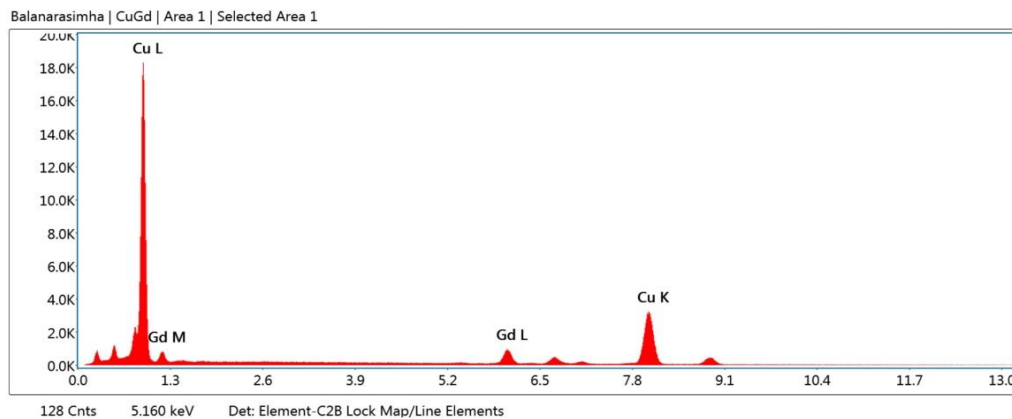


Figure 3.4 a) Photograph of Cu_9Gd_2 Inoculant b) EDS of Cu_9Gd_2 Inoculant.

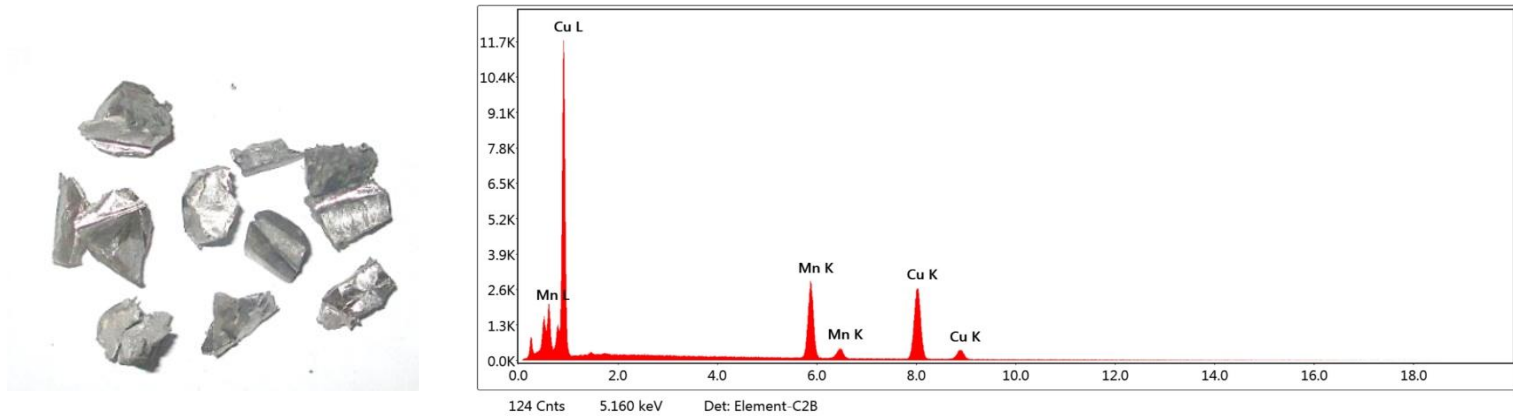


Figure 3.5 a) Photograph of CuMn_{30} Inoculant b) EDS of CuMn_{30} Inoculant

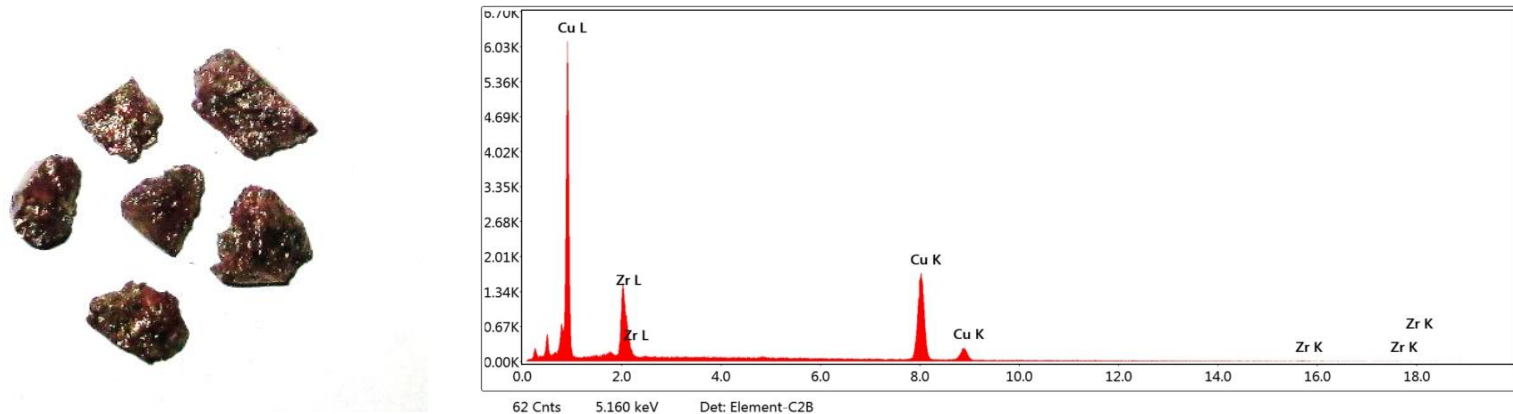


Figure 3.6 a) Photograph of $\text{Cu}_{51}\text{Zr}_{14}$ Inoculant b) EDS of $\text{Cu}_{51}\text{Zr}_{14}$ Inoculant.

3.4 METHODOLOGY

The experimental methodology carried out in the present investigation is, as shown in Figure 3.7. The procedures for the preparation of alloys and samples for microstructure, morphology, phases, transformation temperatures, shape recovery, and tensile studies have been discussed in the proceeding sections.

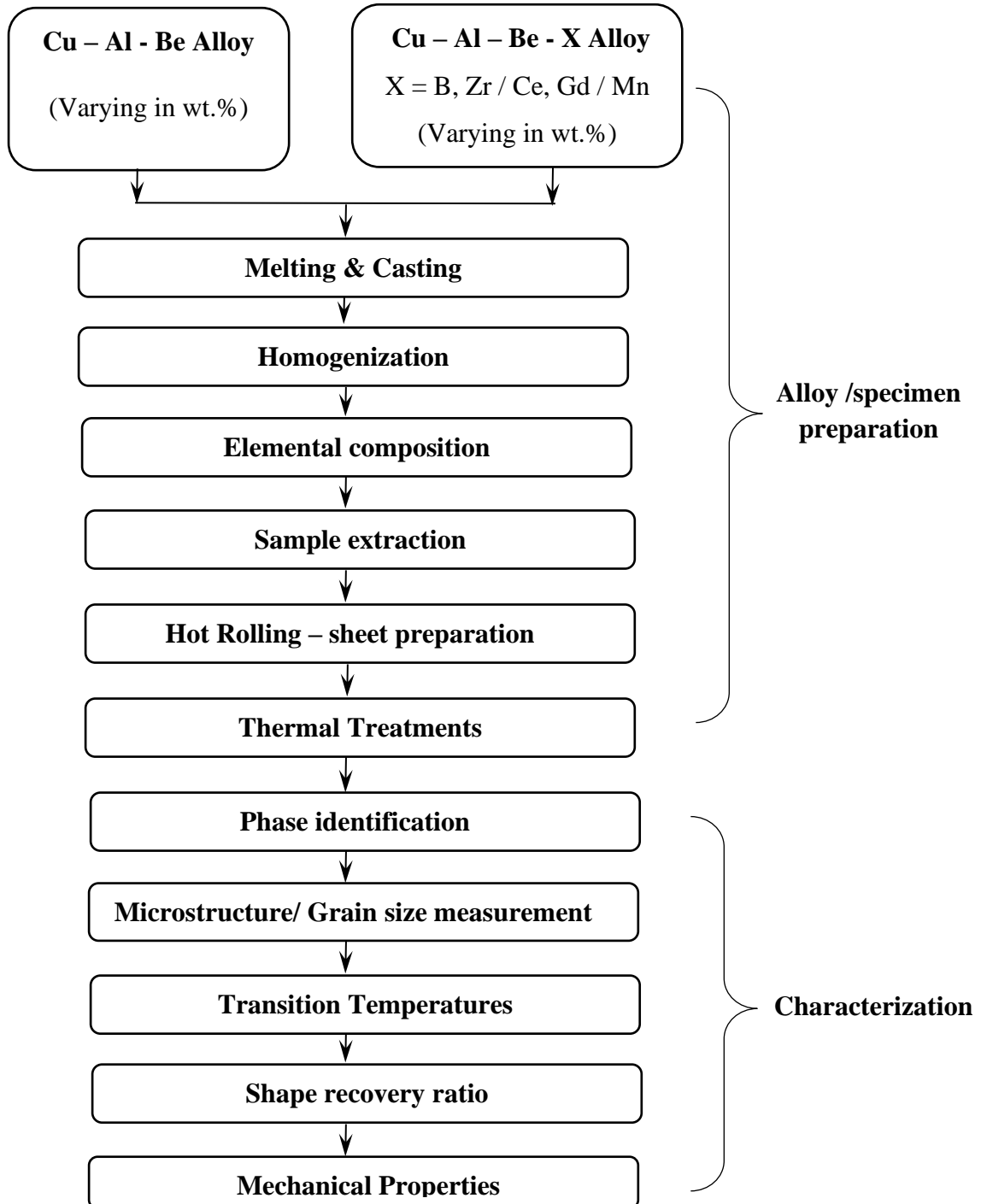


Figure 3.7 Flow chart of Methodology

3.4.1 Alloy preparation

3.4.1.1 Melting and casting

Initially, the mixture of raw material was weighed as per the nominal elemental compositions in terms of wt.% and melted in an isostatic graphite crucible under argon atmosphere using induction melting furnace is as shown in Figure 3.8. Melt was transferred into the preheated die steel mold of $110 \times 110 \times 3 \text{ mm}^3$ and cast in the form of the plate, as shown in Figure 3.10. The prepared alloys were homogenized at $800 \text{ }^\circ\text{C}$ for 4 hours in the muffle furnace, as shown in Figure 3.9, under argon atmosphere to ensure homogeneous distribution of elements in the matrix, and then dry quenched to room temperature to avoid cracking (Davis and Committee 2001).



Figure 3.8 Induction melting furnace with inert gas setup.



Figure 3.9 Muffle Furnace with inert gas setup.



Figure 3.10 Alloy Plate.

3.4.1.2 Sample preparation

Samples for microstructural, tensile, and shape recovery studies were extracted from the alloy plates using the wire electric discharge machine (WEDM). A portion of $150 \times 10 \times 3 \text{ mm}^3$ plates for shape recovery studies were hot-rolled at $800 \text{ }^\circ\text{C}$ using a multi-purpose rolling machine. These plates were rolled with a reduction of 0.5 mm at each step to a final sheet of 0.5 mm thickness with intermediate annealing for five minutes to relieve the working stresses.

3.4.1.3 Betatization/Annealing

Samples extracted from WEDM and rolling were betatized at $850 \text{ }^\circ\text{C}$ for 15 minutes under argon gas atmosphere to avoid oxidation and then quenched directly into the water at room temperature.

3.4.2 Characterization

Betatized and quenched samples were investigated for phase identification, microstructure, morphology, phase transformation temperatures, mechanical properties using various instruments, and procedures for grain size and shape recovery ratio. The detailed procedure for each study is discussed in the proceeding sections.

3.4.2.1 Elemental composition

The elemental composition of the homogenized SMAs was determined using an optical emission spectrometer (Model:MAXxLMF04, Make: AMETEK). Spark ignited at three different locations of the plate, and an average of three readings is considered as final. Inductively coupled plasma-optical emission spectroscopy (ICP-OES, Make: Agilent, Model: Agilent 5100) was used to determine the actual composition of rare earth elements. Initially, the samples were digested in the aquaregia of 10 ml, i.e., 8ml HCl and 2ml HNO₃, later the aquaregia was diluted with distilled water to 100 ml. The diluted samples were tested under the wavelengths of 396.153, 313.107, 413.764, 327.393, and 342.247 nm for Al, Be, Ce, Cu, and Gd, respectively.

3.4.2.2 Phase Identification (XRD)

Phases and crystal structure of the betatized and quenched SMAs were determined by X-Ray Diffractometer (Make: Rigaku, Model: Miniflex 600) at room

temperature. The specimen was placed with backing of adhesive tape in an aluminium (rectangular cut) holder and then placed on the sample stage. Then the stage was rotated from $2\theta = 20^\circ$ to 90° under $\text{CuK}\alpha 1$ monochromatic radiation ($\lambda = 1.54056 \text{ \AA}$) at 40 Kv and 15 mA.

3.4.2.3 Phase Transformation temperatures

Phase transformation temperatures of the prepared SMAs are determined using differential scanning calorimeter (DSC, Make: Perkin-Elmer, Model: 6000). The samples of mass between 20 to 30 mg were cut using a low-speed diamond saw and then sealed in an aluminium DSC pan with a lid. The sealed aluminium pan was placed in the chamber and heated from -40°C to 300°C at a scan rate of $2^\circ/\text{min}$, followed by cooling to -40°C . DSC tests comprises of 3 cycles i.e., heating, cooling and heating. The martensite and austenite phase transformation temperatures are noted from the first cooling and second heating cycle respectively.

3.4.2.4 Microstructure - Morphology

The microstructure of the betatized and quenched specimens are were examined by using a polarized optical microscope (Model: Zeiss, AxioLab, Make: Zeiss). At first, polish the surfaces of the alloy specimens with various grades of emery sheets, i.e., rough- 400, 800, fine – 1000, 1500, and Ultrafine 2000-grit, followed by velvet cloth polishing under saturated alumina ($1 \mu\text{m}$) suspension to obtain mirror finish. Then the surface is etched using a solution of 2g of FeCl_3 , 2 ml of HCl, and 95 ml of Methanol. The etched samples are thoroughly cleaned with acetone, distilled water and dried, to study the microstructure. The surface morphology, precipitate composition, and fracture mode was investigated using Scanning Electron Microscope (SEM, Make: Zeiss, Model: EVO MA18) attached with energy-dispersive X-ray spectroscopy (EDS Make: Oxford, Model: X-act)

3.4.2.5 Grain size Measurement

The average grain size of the SMAs was measured from the micrographs using the linear intercept method as per ASTM E 1382- semiautomatic and automatic image analysis.

3.4.2.6 Shape Recovery Ratio – Bend Test

The shape recovery ratio (SRR) of the alloys was measured by the bend test (Xu 2008b), as illustrated in Figure 3.11. The test procedure is as follows, the sheet at full martensite state ($\leq M_f$) was bent around a mandrel and unloaded viz. from A-A to A-B, this angle measured as θ_d . The deformed sheet was heated above 10 °C of the austenite finish temperature in the muffle furnace, and it tends to attain the original position with or without residual strain, i.e., A-C or A-A, respectively, this angle measured as θ_r .

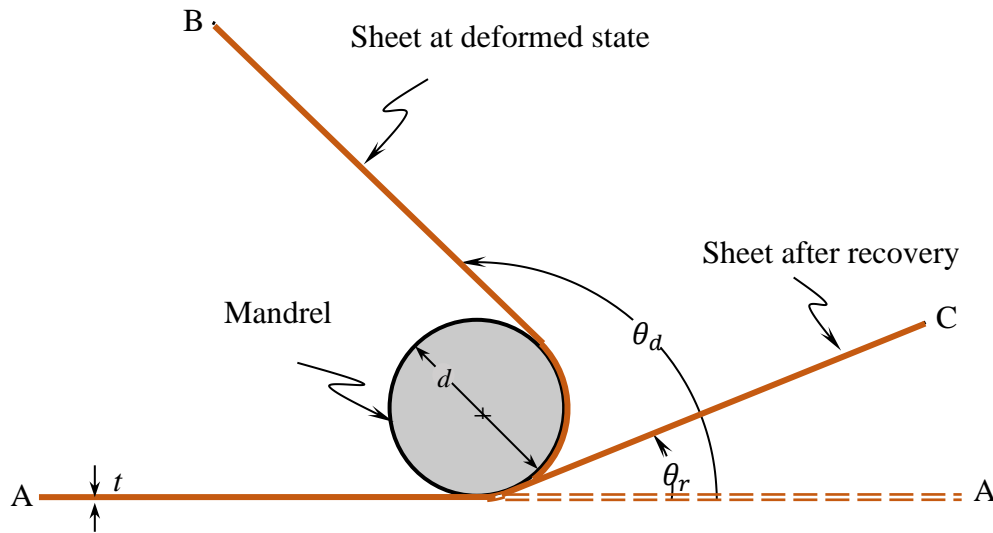


Figure 3.11 Bend Test.

The shape recovery ratio computed using Eq. (1).

$$\eta = \frac{\theta_d - \theta_r}{\theta_d} \quad (1)$$

where θ_d - angle after deformation and θ_r - residual angle after recovery

3.4.2.7 Mechanical Properties – Uniaxial tensile Test

Uniaxial tensile tests were performed using a universal testing machine (Make: Shimadzu, Model: AG-X Plus 100 kN) to determine the mechanical properties, i.e., yield stress, yield strain, ultimate stress, and ultimate strain. Figure 3.12 depicts the beta-tized and quenched tensile specimens. The tests were performed as per the ASTM E8 standard with 0.05 mm/min rate of loading at room temperature (martensite state).



Figure 3.12 Tensile Specimens

3.5 CLOSURE

This chapter reported the details of metals, purity and their range of elemental composition used in the investigation. In addition, the methodology for the preparation of alloys and specimens for characterization studies i.e., XRD, microstructure, morphology, grain size, shape recovery, and uniaxial tensile test studies are presented. The next chapter presents the results of effect of ternary and quaternary elements on the properties and their mechanisms.

CHAPTER 4

RESULTS & DISCUSSION

4.1 INTRODUCTION

The present chapter discusses the details of the elemental compositions of ternary and quaternary Cu-Al-Be-X (X=B, Ce, Gd, Mn, and Zr) SMAs used in the present investigation. The mechanisms of modification of phases, grain refinement, variation in transformation temperatures, and the shape recovery ratio of the alloys have been discussed. At first, Section 4.2 presents the results of ternary Cu-Al-Be SMAs. Secondly, the results of the quaternary element, i.e., boron, cerium, gadolinium, manganese, and zirconium modified alloys are presented in the Sections 4.3 – 4.7, respectively. Finally, the closure of the chapter provides suitable elements and their compositions for designing an actuator.

4.2 Cu-Al-Be – Ternary SMAs

In the present investigation, first ternary Cu-Al-Be SMAs were prepared by varying the wt.% of Al from hypoeutectoid to hypereutectoid composition, i.e., 11 – 12 wt.%, as shown in Figure 4.1, and Be from 0.40 to 0.44 wt.%.

Table 4.1 presents the actual elemental composition of the ternary Cu-Al-Be SMAs. Alloys are designated with a letter, “*T*” represents ternary alloy and subscript with numeral indicates the type of alloy.

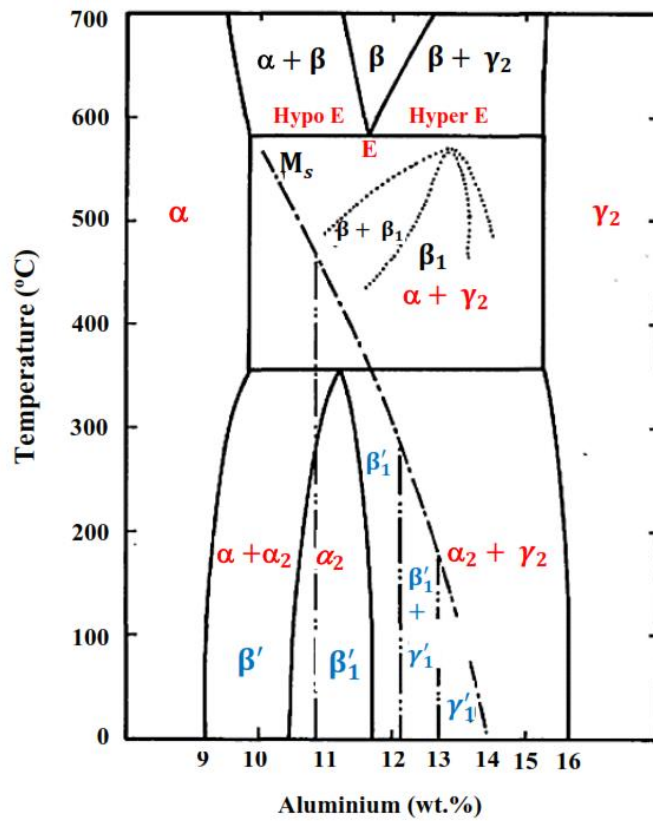


Figure 4.1 Cu-Al phase diagram (Noriyuki et al. 1977)

Table 4.1 Elemental composition and designations of Cu-Al-Be SMAs

S. No	Alloy	Actual composition(wt.%)		
		Cu	Al	Be
1.	T_1	88.60	11.00	0.40
2.	T_2	88.27	11.32	0.41
3.	T_3	87.96	11.62	0.42
4.	T_4	87.80	11.78	0.42
5.	T_5	87.58	12.00	0.42
6.	T_6	88.53	11.04	0.43
7.	T_7	88.13	11.44	0.43
8.	T_8	87.96	11.61	0.43
9.	T_9	87.67	11.90	0.43
10.	T_{10}	88.56	11.00	0.44
11.	T_{11}	87.71	11.85	0.44

4.2.1 XRD – Phases

The prepared ternary SMAs were betatized and rapid quenched to water at room temperature, as discussed in Section 3.4.1.3. Phases that exist in the alloys are determined by XRD and are presented in Figure 4.2. Diffractograms reveals that hypoeutectoid alloys (i.e., < 11.8 wt.% of Al) possess a mixture of “ α ” and β'_1 phases (Chentouf et al. 2009; Hussein 1982), and the eutectoid and hypereutectoid alloys (i.e., ≥ 11.8 wt.% of Al) forms complete β'_1 martensite . It is also observed that increase in wt.% of Be forms coexistence of $\beta'_1 + \gamma'_1$ martensite variants in the alloy. β'_1 martensite is of 18R layered configuration and has an orthorhombic crystal structure, γ'_1 martensite is of 2H configuration and has monoclinic structure, whereas α is FCC structure.

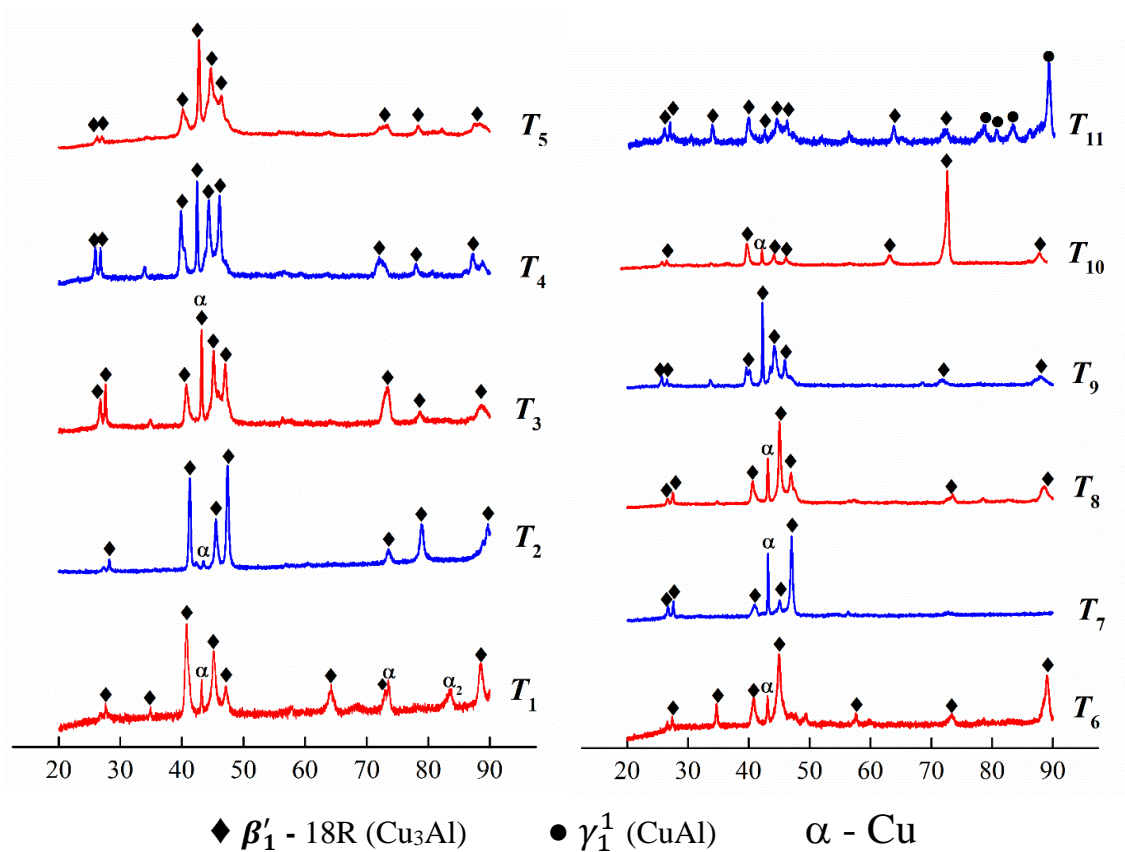


Figure 4.2 X-ray diffractograms of Cu-Al-Be SMAs.

4.2.2 Microstructure and morphology

Figure 4.3 depicts the microstructures of the Cu-Al-Be SMAs. It is evinced that all the alloys possess equiaxed and coarse grains in longitudinal and transverse directions. The average grain size of the alloys is $463.45 \mu\text{m} \pm 10 \mu\text{m}$.

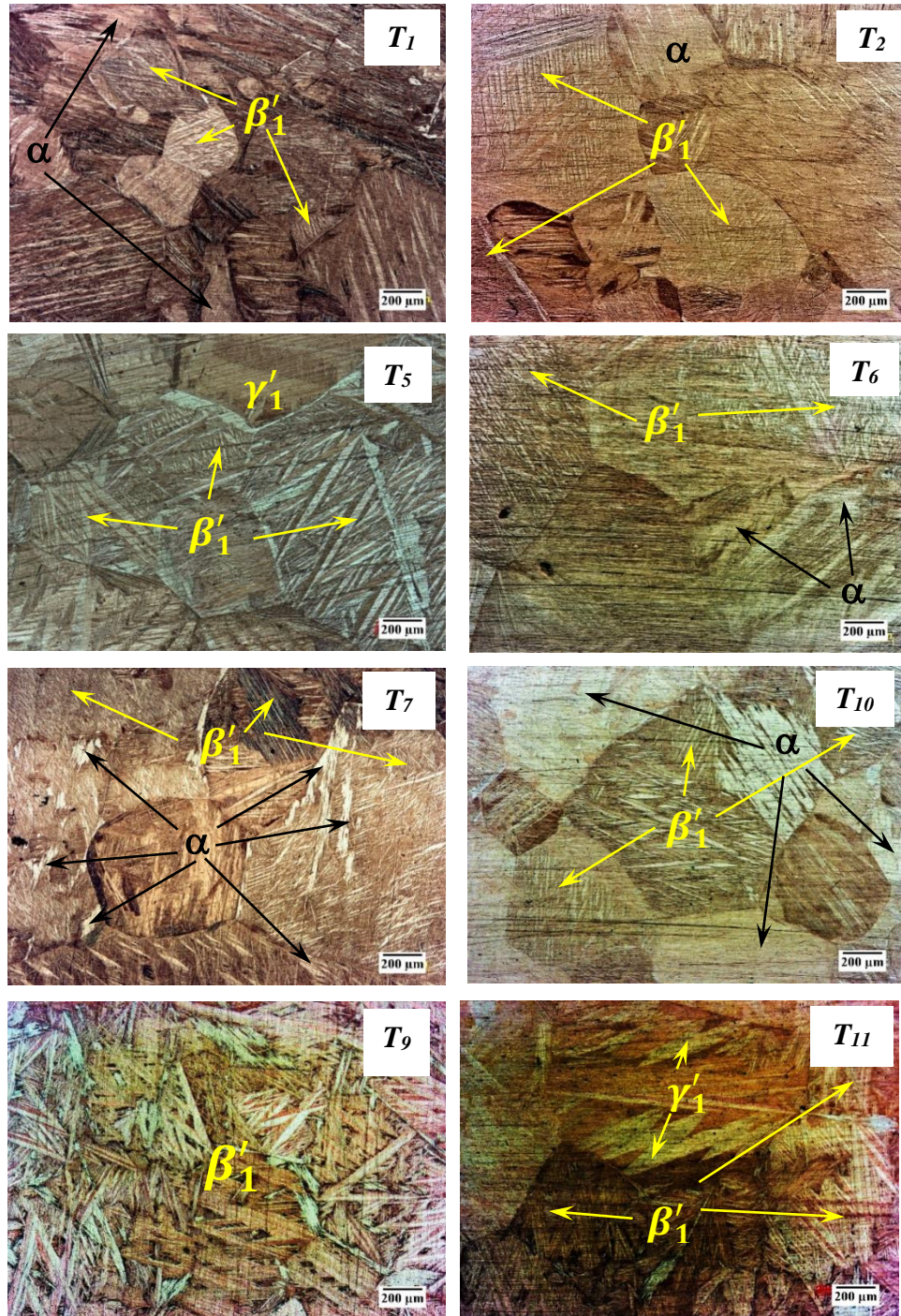


Figure 4.3 Microstructures of Cu-Al-Be SMAs.

Microstructures reveal that Cu-Al-Be SMAs with hypoeutectoid composition, i.e., Al < 11.8 wt. % exhibits a mixture of “ α ” and β'_1 martensite phases, whereas SMAs with hypereutectoid composition, i.e., Al \geq 11.8 wt.% exhibits complete martensite of β'_1 phase. Cu-Al-Be SMAs with hypereutectoid composition and increase in Be \geq 0.44 exhibit coexistence of martensites $\beta'_1 + \gamma'_1$ variants. “ α ” phase is of bright and bulky plate morphology, β'_1 martensite is in the form of fine and sharp needles and γ'_1 martensite is coarse and thick plates.

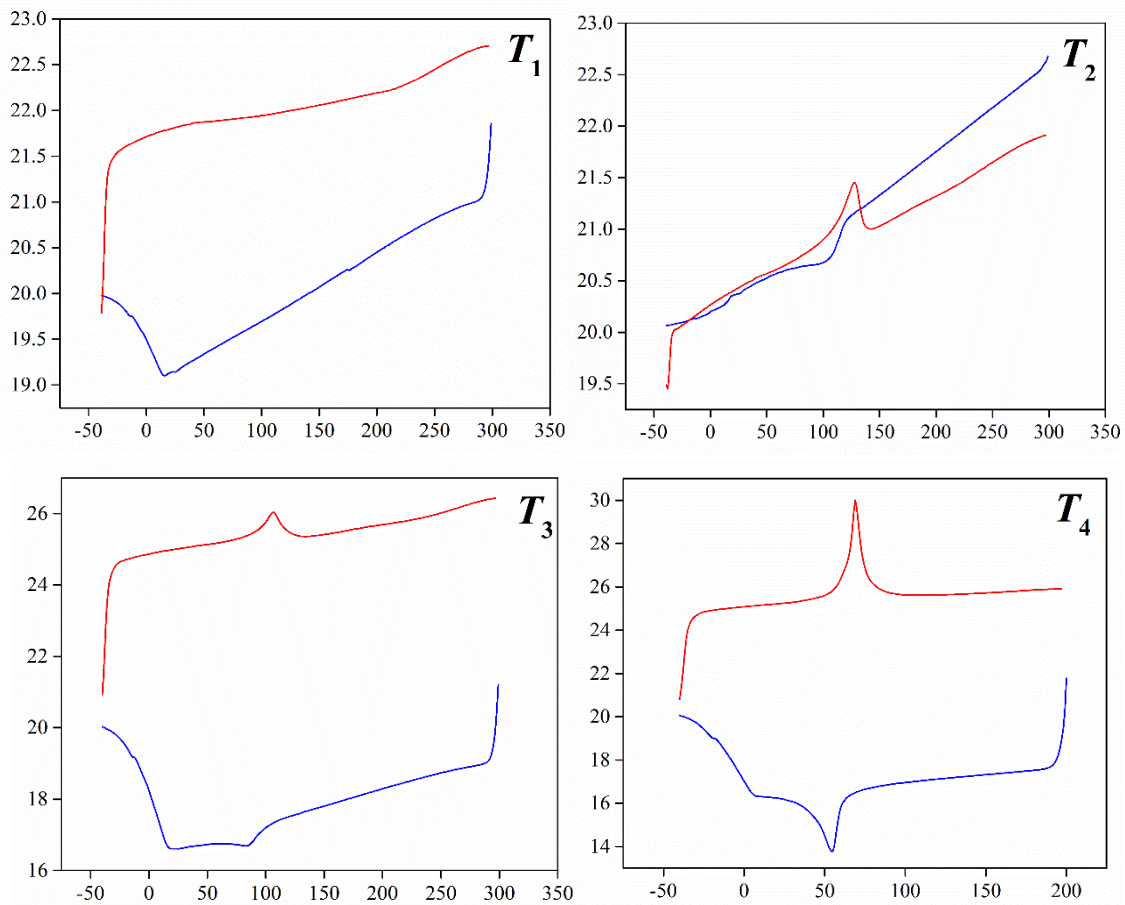
SMAs T_1 , T_6 and T_{10} exhibit major fraction of α -phase and a minor fraction of β'_1 martensite as shown in Figure 4.3a, d and f due to the lower wt.% of Al (i.e., 11), and increase in Al diminishes the α -phase with the growth of β'_1 martensite plates up to 11.8 wt.%, as shown in Figure 4.3g. It is also observed that the increase in Al increases the martensite fraction and modifies the morphology of martensite from needles shaped martensite plates to spear shape in a zig-zag configuration. SMA T_5 exhibits a major fraction of β'_1 martensite and a minor fraction of γ'_1 monoclinic martensite, as shown in Figure 4.3c, due to the increase in addition to 0.2 wt.% of Al. Increase in Be to 0.44 wt.% forms coexistence of martensites, as shown in Figure 4.3h.

It is worth noting from microstructures and diffractograms that, (i) the mixture of “ α ” and “ β'_1 ” phase forms till eutectoid composition, i.e., 11.8 wt.% of Al, in contrast, the same mixture forms < 11 wt.% of Al in Cu-Al alloys (Noriyuki et al. 1977), and the same observed in the studies of Cu-Al-Ni SMAs (Chentouf et al. 2009), (ii) SMAs with eutectoid composition and up to 0.43 wt.% of Be exhibit complete β'_1 martensite, whereas in Cu-Al alloys entire β'_1 phase forms from 11 wt.% of Al and (iii) SMAs with near to eutectoid composition i.e., 11.85 wt.% of Al and Be \geq 0.44 forms coexistence of $\beta'_1 + \gamma'_1$ martensites, in contrast the same mixture forms > 12.3 wt.% of Al in Cu-Al alloys (Noriyuki et al. 1977). It is confirmed that the phases shift towards the lower wt.% of Al than the actual region of Cu-Al alloys, and the shift is due to the addition of Be lowers the eutectoid plateau (Higuchi et al. 1982; Nickel

1957b). Whereas hypoeutectoid composition didn't exhibit any shift though with the increase in Be from 0.4 – 0.44 wt.%.

4.2.3 Phase transformation temperatures

The transformation temperatures, enthalpies, and hysteresis of betatized and quenched Cu-Al-Be SMAs are measured using DSC and enthalpy (ΔH) from the area under the curve, and the results are depicted in Figure 4.4 and 4.5, and tabulated in Table 4.2. The curve with red color represents reverse transformation, i.e., from martensite to austenite, with the addition of heat (endothermic reaction + ΔH) and curve with blue color represents forward transformation, i.e., austenite to martensite with the release of heat (exothermic reaction - ΔH). The transformation temperatures of the alloys were measured, adopting baseline tangent method, i.e., the intersectional points of tangents at the base and sides of the thermograms, as shown in the thermogram T_5 .



X axis – Temperature (°C) **Y axis** – Heat flow (mw)

Figure 4.4 Thermograms of T_1 , T_2 , T_3 , and T_4 Cu-Al-Be SMAs.

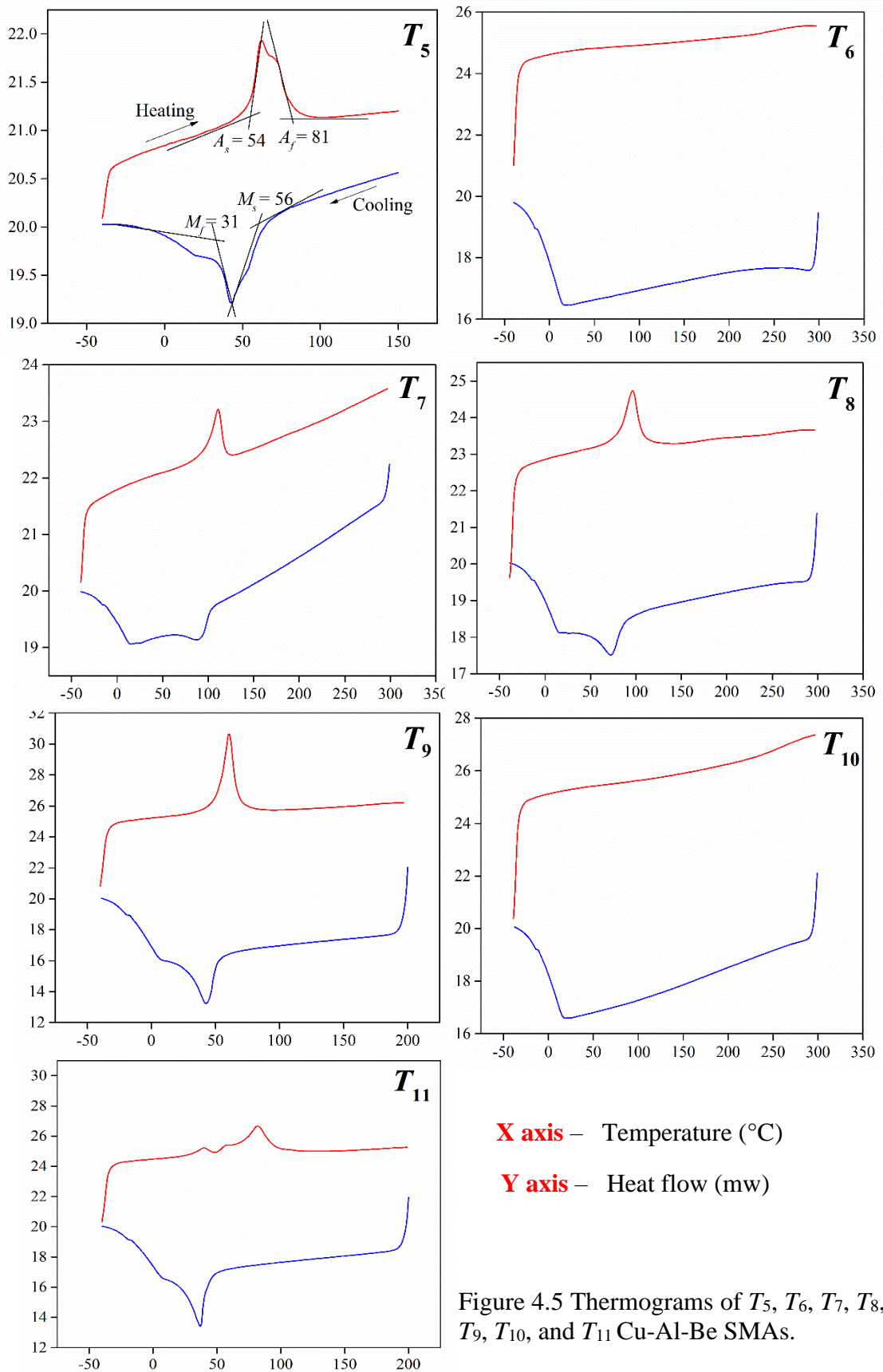


Figure 4.5 Thermograms of T_5 , T_6 , T_7 , T_8 , T_9 , T_{10} , and T_{11} Cu-Al-Be SMAs.

Table 4.2 Transformation temperatures, enthalpies, and hysteresis of Cu-Al-Be SMAs.

S. No	Alloy	M_f (°C)	M_s (°C)	$\Delta H_{A \rightarrow M}$ (J/g)	A_s (°C)	A_f (°C)	$\Delta H_{M \rightarrow A}$ (J/g)	Hysteresis ($A_f - M_s$) (°C)
1.	T_1	> 300						
2.	T_2	66	119	1.5804	107	136	1.9986	17
3.	T_3	61	98	-0.7157	91	119	1.5292	21
4.	T_4	41	60	-5.4488	64	75	5.8998	15
5.	T_5	31	56	-14.828	54	81	9.7952	25
6.	T_6	> 300						
7.	T_7	62	102	-1.8735	97	118	2.3862	16
8.	T_8	47	86	-2.671	79	108	3.7093	22
9.	T_9	26	51	-5.6625	52	68	6.53	17
10.	T_{10}	> 300						
11.	T_{11}	22	41	-8.7185	43	58	7.7565	17

Thermograms T_1 , T_6 , and T_{10} didn't exhibit any transformation until 300 °C indicate a very lower fraction of martensite as confirmed from microstructures and diffractograms, ascribed to very lower addition wt.% of Al, i.e., 11% though with the increase in Be from 0.4 to 0.44 wt.%. T_2 , T_3 , T_7 , and T_8 exhibit a rise in the curve and broader indicates that requires excessive thermal energy for transformation, whereas T_4 , T_5 , and T_9 exhibit a sharp peak that indicates the rapid transformation of martensite to austenite due to the composition of Al near to eutectoid. T_{11} exhibits two endothermic peaks represents double stage martensitic reverse transformation, i.e., the first endothermic peak in the lower temperature side represents the transformation of $\beta'_1 \rightarrow \beta_1$ and the second endothermic peak in the higher temperature side represents the transformation from $\gamma'_1 \rightarrow \beta_1$. It is also observed that an increase in wt.% of both Al and Be decreases the transformation temperatures, confirms from the Table and thermograms.

4.2.4 Shape recovery ratio

The shape recovery ratio of the Cu-Al-Be SMAs was measured by the bend test, and the results are depicted in Figure 4.6.

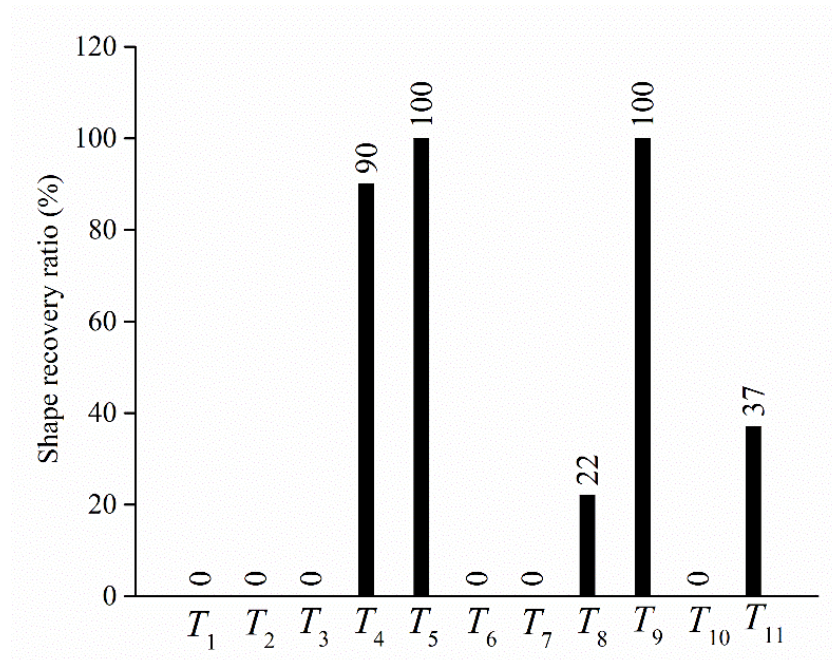


Figure 4.6 Shape recovery ratio of Cu-Al-Be SMAs.

T_1 , T_2 , T_3 , T_6 , T_7 , and T_{10} exhibits no recovery, whereas T_4 , T_5 , T_8 , T_9 , and T_{11} exhibits recovery of 90, 100, 22, 100, and 37%, respectively. Alloys didn't exhibit recovery (i) due to the mixture of " α " and β'_1 phases in the alloys as discussed in Section 4.2.2 and as shown in Figure 4.3, (ii) rapid quenching of alloys with lower wt.% of both Al and Be forms α plates reduces the recovery (Dong et al. 1994) and (iii) it is also noticed broader curves of thermograms indicates recovery with the excessive addition of heat (Balo and Ceylan 2002) and confirms from the DSC.

4.2.5 Mechanical properties

Mechanical properties, i.e., ultimate tensile strength, ductility, yield stress (0.2% Proof stress), and yield strain of the alloys, are determined by the uniaxial tensile tests as discussed in Section 3.4.2.7. The measured engineering stress-strain curves are depicted in Figure 4.7 and tabulated in Table 4.3. The mechanical properties are evaluated for the SMAs exhibit complete recovery, which serves function, i.e., T_5 and T_9 .

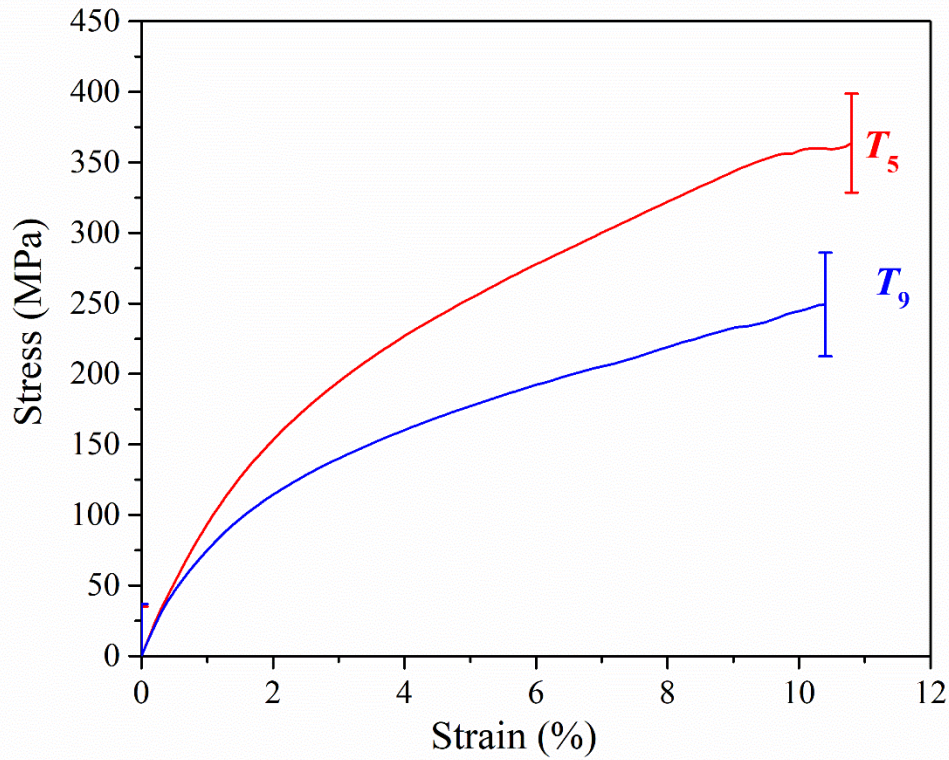


Figure 4.7 Stress-strain Curves of Cu-Al-Be SMAs.

Table 4.3 Mechanical properties of ternary Cu-Al-Be SMAs.

Alloy	Ultimate tensile strength (MPa)	Ductility (%)	Yield stress (0.2 %) (MPa)	Yield strain (0.2 %)
T_5	363 ± 35	10.80 ± 0.75	132.34 ± 8.40	1.60 ± 0.03
T_9	261 ± 36	10.40 ± 0.30	74.69 ± 22.61	0.93 ± 0.24

Stress-strain curves present T_5 has an ultimate tensile strength of 363 ± 35 MPa with the ductility of 10.80 ± 0.75 % fails in cleavage mode, as shown in Figure 4.8a. Increase in Be of 0.1 wt.%, i.e., T_9 has an ultimate tensile strength of 261 ± 36 MPa with the ductility of $10.40 \pm 0.30\%$ fails intergranular, as shown in Figure 4.8b. It is observed that an increase in Be decreases the tensile strength, ductility, yield stress, and yield strain. Fracture morphology (Figure 4.8) of both the alloys indicates that alloys fail brittle, i.e., separation occurs along crystallographic planes, has low cohesive

strength, and high stress concentration at the grain boundaries (Candido et al. 2012), attributes to coarse grains.

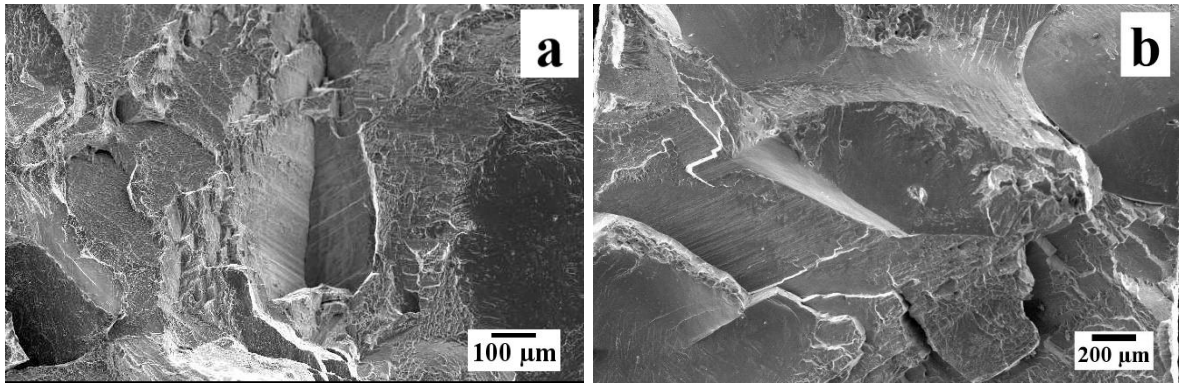


Figure 4.8 Fracture morphology of Cu-Al-Be SMAs.

4.3 Cu-Al-Be-B

Based on the literature survey, the addition of boron as quaternary element performs good grain refinement and more than 0.15 wt.% leads to poor shape recovery (Sampath 2006; Zhang et al. 2009). This section presents the effect of microalloying of boron, i.e., 0.02 – 0.15 wt.% to Cu-Al-Be SMA and its impact on microstructure, phases, transformation temperatures, and shape recovery ratio. The elemental compositions and their designations are tabulated in Table 4.4, and the alloys are designated as “B_{XY},” ‘X’ represents the type of alloy, ‘Y’ represents the wt.% of B. Y = 1, 2, 3, 4, 5 and 6 for 0.02, 0.04, 0.06, 0.08, 0.1 and 0.15 wt.% of B, respectively.

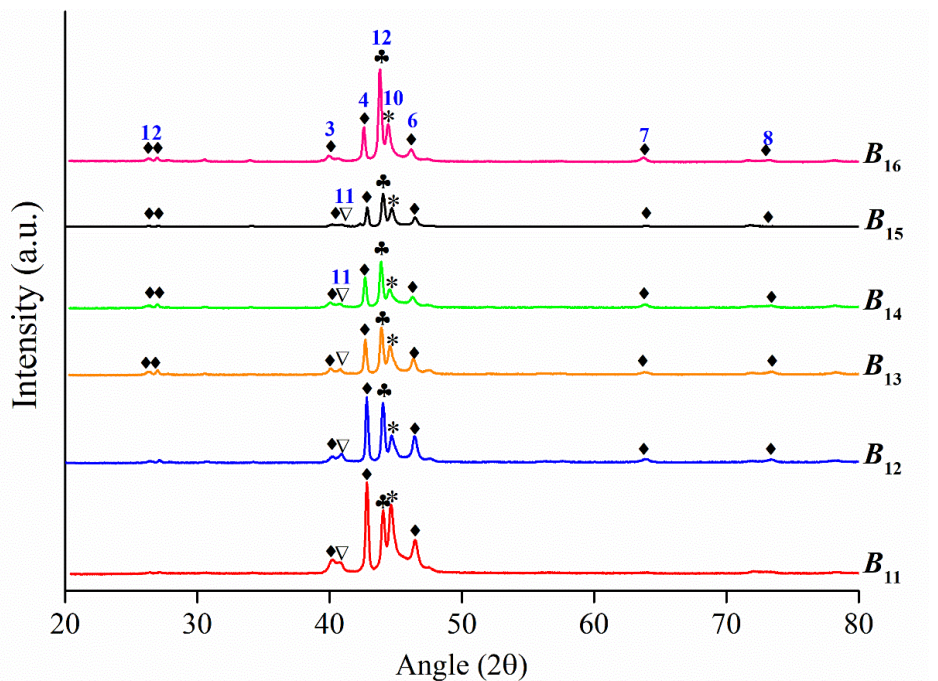
Table 4.4 Elemental composition and designations of Cu-Al-Be-B SMAs.

S. No	Alloy	Actual Composition (wt.%)			B (wt.%)
		Cu	Al	Be	
<i>Al, Be – constant, Boron - Increase</i>					
1.	B ₁₁	87.64	11.90	0.44	0.02
2.	B ₁₂	87.62	11.90	0.44	0.04
3.	B ₁₃	87.6	11.90	0.44	0.06
4.	B ₁₄	87.58	11.90	0.44	0.08
5.	B ₁₅	87.56	11.90	0.44	0.10
6.	B ₁₆	87.51	11.90	0.44	0.15
<i>Be, B – constant, Aluminium - Increase</i>					
7.	B ₂₁	87.67	11.90	0.41	0.02
8.	B ₃₁	87.57	12.00	0.41	0.02
9.	B ₄₄	87.89	11.60	0.45	0.08
10.	B ₅₄	87.57	11.90	0.45	0.08
<i>Al, B – constant, Beryllium - Increase</i>					
11.	B ₆₂	88.17	11.37	0.42	0.04
12.	B ₇₂	88.19	11.36	0.43	0.04
13.	B ₂₁	87.68	11.90	0.41	0.02
14.	B ₁₁	87.64	11.90	0.44	0.02

4.3.1 XRD - Phases

XRD was employed to study the existence of phases in the alloys, and the results are presented in Figures 4.9 – 4.12. Red, blue, orange, green, black and pink colored lines represent boron addition of 0.02, 0.04, 0.06, 0.08, 0.1 and 0.15 wt.%, respectively. Diffractograms reveals various phases present in the alloys, and refinement of grain size confirmed from their intensities, peak positions, and FWHM.

Figure 4.9 presents the diffractogram of B_{1Y} alloys. Diffractogram conveys that betatized and quenched alloys are of complete martensite phase of $\beta'_1(\text{Cu}_3\text{Al})$ and $\gamma'(\text{Cu}_{6.11}\text{Al}_{3.89})$, along with secondary phases of AlB_2 and $\text{AlB}_{25}\text{Cu}_{0.79}$. Secondary phases, i.e., AlB_2 and $\text{AlB}_{25}\text{Cu}_{0.79}$, are rich in boron and aluminium composition. The phases β'_1 , γ' , AlB_2 , $\text{AlB}_{25}\text{Cu}_{0.79}$ has of monoclinic (M18R), rhombohedral, rhombohedral and tetragonal structures. B_{1Y} series indicates refinement of grain size with an increase in boron confirms from the decrease in intensities and increase in FWHM of the peaks of M18R (P-3,4,6) and AlB_2 (P-11). It is also observed that the intensity of γ' martensite (P-9) increases with the increase in addition of B.



- ♦ β'_1 - 1 (111), 2 (0 1 11), 3 (2 0 2), 4 (0 0 22), 5 (12 10), 6 (20 12), 7 (0 3 17), 8 (2 1 28)
- ♣ γ' - 9 (3 0 6), # α_2 - 10 (2 2 1) * AlB_2 - 11 (1 0 1), ▽ $\text{AlB}_{25}\text{Cu}_{0.79}$ - 12 (2 0 2)

Figure 4.9 X-ray diffractograms of B_{1Y} alloys.

Diffractograms of B_{21} and B_{31} (Figure 4.10) discerns that the quenched alloys are in a state of martensite along with a new phase “ α_2 ” (P-10). The phase “ α_2 ” is of Cu_4Al composition with cubic structure, forms around the temperature between 350 – 200 °C (Noriyuki et al. 1977), quenched from high-temperature β (Cu_3Al) phase of the alloy. In this case, though the alloys are rich in aluminium and rapidly quenched from 850 °C to water at RT (30 °C), the phase “ α_2 ” formation may be due to the very low addition of Be, i.e., 0.41 wt.%, affects the cooling rate in the formation of martensite. It is also observed an increase in 0.1 wt.% Al from B_{21} to B_{31} , affects the martensite fraction confirm from their intensities of peaks.

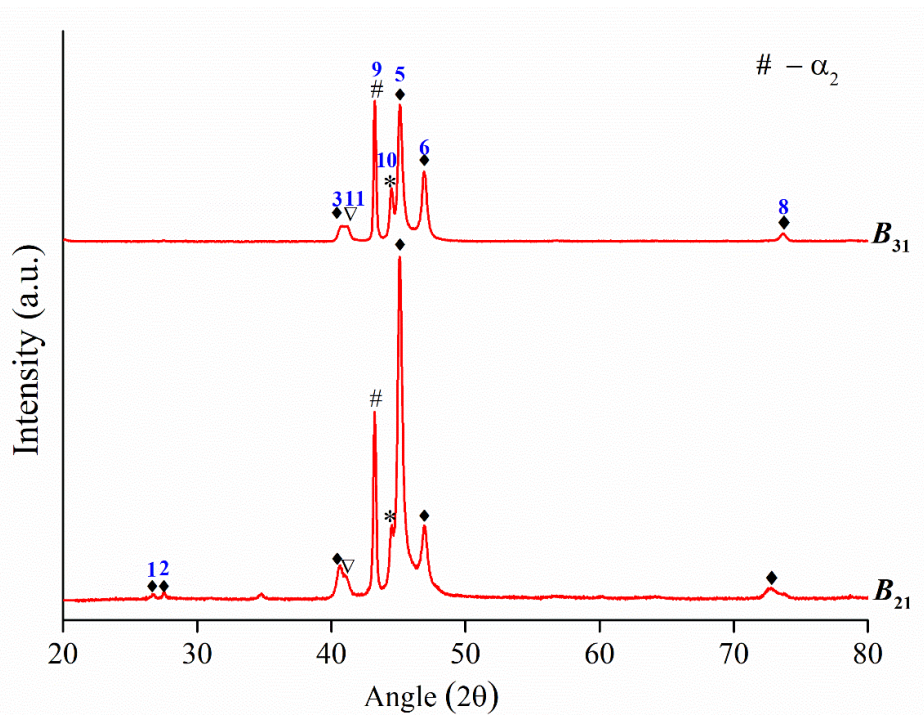


Figure 4.10 X-ray diffractograms of B_{21} and B_{31} alloys.

The diffractograms of B_{44} and B_{54} depicted in Figure 4.11 discern that the alloy B_{54} possesses and exhibits an additional two phases (peak 8, 12) viz. $\text{Al}_{3.89}\text{Cu}_{6.11}$ and $\text{AlB}_{25}\text{Cu}_{0.9}$ are of γ' rhombohedral martensite and boron rich secondary phase, compared to B_{44} . The existence of two phases attributed to increase in 0.3 wt.% of Al forms the mixture of two variants of martensites $\beta'_1 + \gamma'$ (Noriyuki et al. 1977; P.R. and Warlimontt 1963) and the affinity towards B forms boron rich $\text{AlB}_{25}\text{Cu}_{0.9}$ phase.

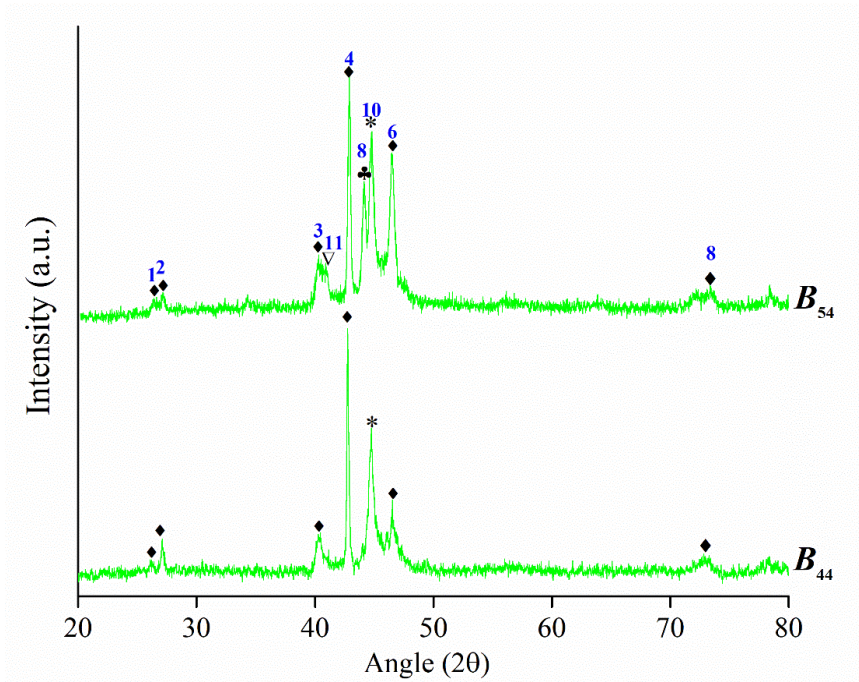


Figure 4.11 X-ray diffractograms of B_{44} and B_{54} alloys.

Diffractogram B_{62} and B_{72} (Figure 4.12) reveals martensite M18R and AlB_2 , without $AlB_{25}Cu_{0.9}$ and $Al_{3.89}Cu_{6.11}$ phases due to the very low addition of B (0.02) and the minimum addition of Al compared to former alloys.

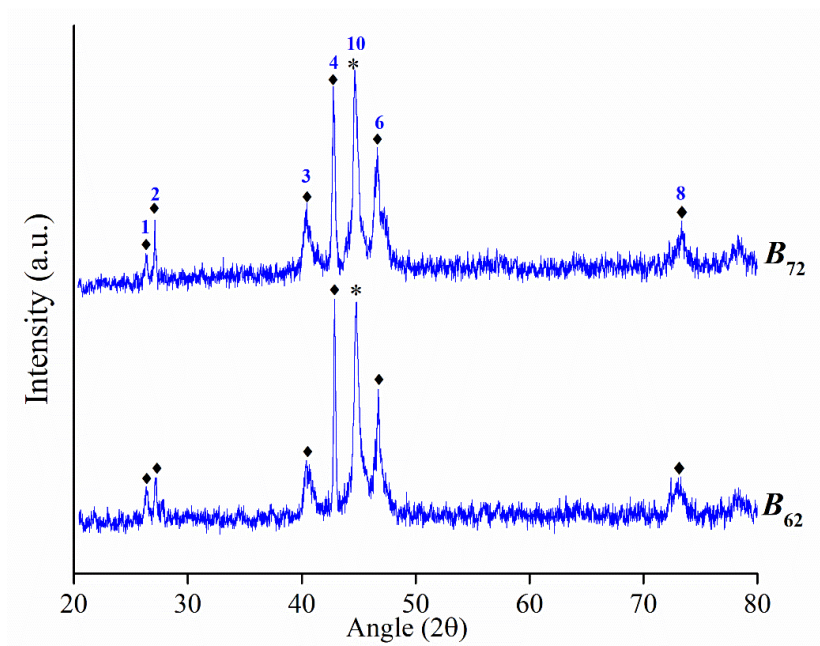


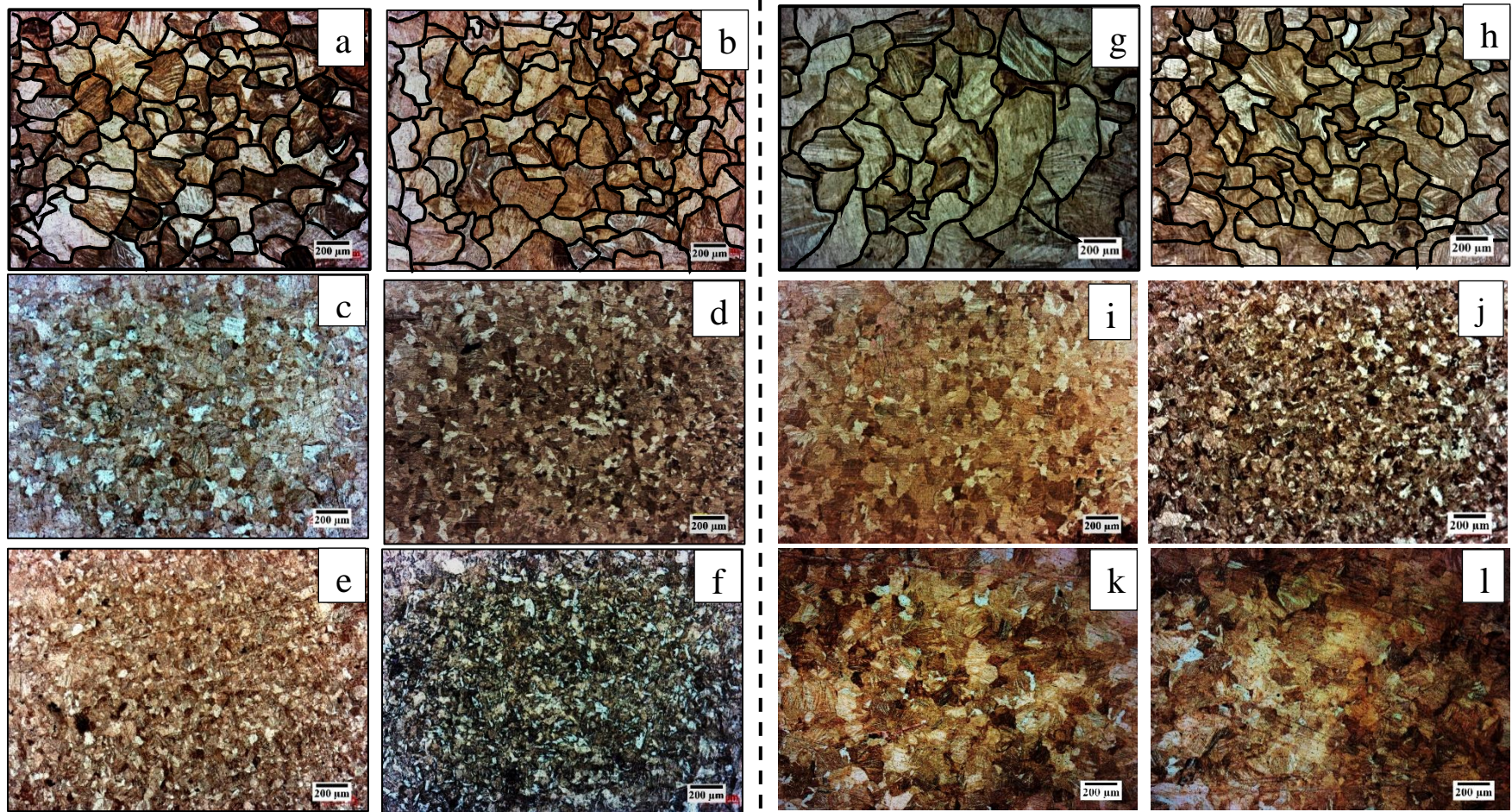
Figure 4.12 X-ray diffractograms of B_{62} and B_{72} alloys.

From the diffractograms of all the alloys, the salient observations are a) Addition of B to the matrix forms AlB_2 precipitates and along with an increase in Al forms $AlB_{25}Cu_{0.9}$ phases, i.e., rich in boron and aluminium. b) An increase in Al and Be increases the martensite fraction. c) Addition of Be < 0.42 wt.% forms phase “ α_2 ” d) Microalloying of boron confined only to grain refinement, without any phase formation/modification like Al and Be. e) it is worth noting that alloying boron modifies the martensite plate thickness, i.e., ternary SMA T_{11} (11.9 wt.% Al and 0.44 wt.% Be) exhibit coexistence of martensites $\beta'_1 + \gamma'_1$ with coarse martensite plates, whereas in the present case, the thickness reduces, as shown in Figure 4.14c. f) The prime martensite peak of all the alloys is (0 0 18) except in the series B_{21} and B_{31} (1 2 10), i.e., due to the lower addition of Be, i.e., < 0.42 wt.%. g) γ' martensite ($Al_{3.89}Cu_{6.11}$) and Al-B rich phase ($AlB_{25}Cu_{0.9}$) forms only above 11.8 wt.% of Al, has a higher affinity towards B forms these phases/precipitates attributes to the difference in electronegativity.

4.3.2 Microstructure and morphology

Microstructures of the betatized and quenched Cu-Al-Be-B modified alloys are depicted in Figure 4.13. Morphology of grains, grain boundaries, and the elemental composition of the phases are captured using SEM-EDS, as shown in Figure 4.14. Microstructures exhibit complete lath martensite at room temperature in the form of needles, and the grains were refined to various sizes for the variation in the elemental composition. It is worth noting to be observed that the grain boundaries of alloys are highly non-uniform/serrated (Figure 4.13) and confirmed with the existing literature (Hussain et al. 2019; Lee and Wayman 1986a; Morris 1992; Zhang et al. 2019).

The average grain size was calculated using ASTM E -1382 by taking an average of 20 horizontal and 20 vertical line measurements, because of the irregular/serrated grains. It is observed an increase in boron exhibits improved refinement in grain size to 134.7, 89.03, 73.33, 68.58, 51.64 and 40.19 μm for B_{11} , B_{12} , B_{13} , B_{14} , B_{15} , and B_{16} respectively, with minimal addition of B. The grain size of B_{21} , B_{31} , B_{44} , B_{54} , B_{62} , and B_{72} SMAs are 210.27, 139.85, 81.84, 36.97, 144.74 and 128.71 μm , respectively.



(a) B_{11} , (b) B_{12} , (c) B_{13} , (d) B_{14} , (e) B_{15} , and (f) $B_{16} - 50\times$

(g) B_{21} , (h) B_{31} , (i) B_{44} , (j) B_{54} , (k) B_{62} and (l) $B_{72} - 50\times$

Figure 4.13 Microstructures of Cu-Al-Be-B SMAs.

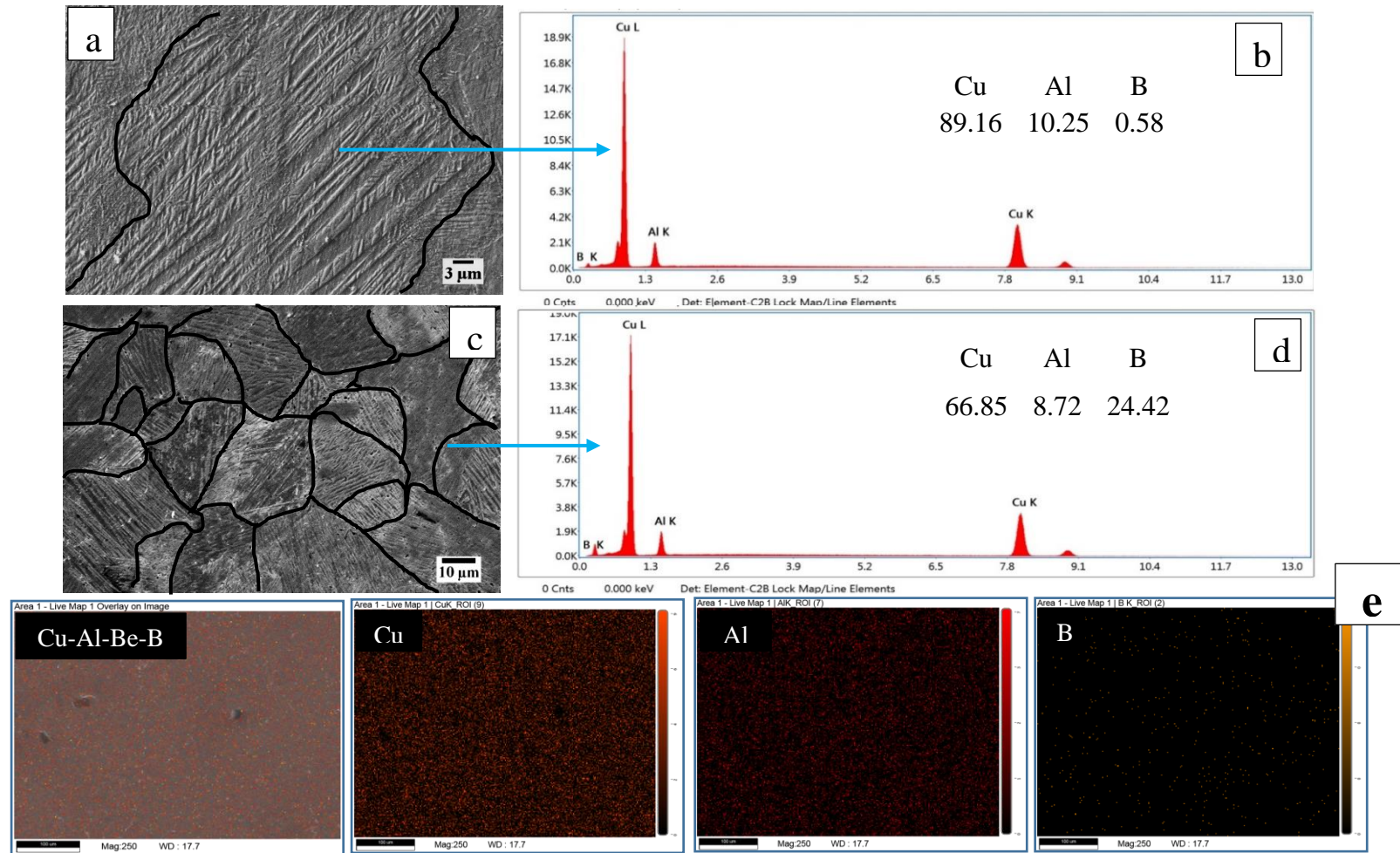


Figure 4.14 SEM images of Cu-Al-Be-B SMAs. (a) B_{11} (c) B_{16} , EDS spectrum: (b) B_{11} , (d) B_{16} , Elemental mapping : (e) B_{16}

Grain refinement mechanisms are as follows:

- i. *Heterogeneous nucleation* – Based on XRD results, it is observed that the addition of B to the alloy forms fine AlB_2 (aluminium diboride) phase/precipitates and dissolves in the solid solution (Lee and Wayman 1986a) confirmed from the SEM-EDS. AlB_2 forms due to the boron is a surface-active element and tend to diffuse throughout the matrix at the high temperature and segregate at the grain boundaries (Lozovoi and Paxton 2008) after quenching to room temperature due to its low solubility and very small atomic radius. In Cu, B has a solubility of 0.01 wt.% (Baker and Okamoto 1992), and in Al, it has no solubility forms $\text{Al}+\text{AlB}_2$ intermetallic particles by a peritectic reaction (Duschanek and Rogl 1994; Wang 2005) at room temperature. These AlB_2 particles/precipitates act as nucleant in the refinement of grains (Birol 2012; Suresh et al. 2009). It is also observed from SEM-EDS studies, that the accumulation of increased density of AlB_2 particles at the grain interfaces, inhibits the grain growth.
- ii. *Growth Restriction factor (GRF)* - It is observed, that B has a strong impact on grain refinement with minimal addition as shown in Figure 4.13, due to its highest growth restriction factor (GRF) in Cu (Balart et al. 2016) and Al (Chen et al. 2016; Wang et al. 2011) systems, followed by Be in Cu (Balart et al. 2016). High GRF (Q) in the alloy is due to the increase in constitutional undercooling increases the driving force for the nucleation at the solid/liquid interface, because of rejection of B in the grains and accumulates at the boundary.
- iii. *Lattice disregistry*: difference in the lattice misfit (disregistry) was a very small percentage, i.e., 12.59 % and 33.0 % between the matrix and the nucleant viz. “ $\text{Cu}_3\text{Al} - \text{B}$ ” and “ $\text{Cu}_3\text{Al} - \text{AlB}_2$ ”, respectively.

It is also important to present the factors for the formation of serrated boundaries, i.e., these are formed due to the non-homogeneous deposition of boron at the grain boundaries forms increase the density of borides “ AlB_2 ” at the interfaces of grains causes lattice distortion (Hong et al. 2012) and strain differences (Koul and

Thamburaj 1985). Serrated grains are observed in the Mg alloy systems doped with boron (Emadi 2014).

Figure 4.13 g-j depicts the microstructure of B_{21} , B_{31} , B_{44} , and B_{54} alloys, i.e., increase in Al and maintaining other elements constant. It is observed that the reduction in grain size from B_{21} to B_{31} and B_{44} to B_{54} is 210.27 μm to 139.85 μm and 81.84 μm to 36.97 μm , respectively. Improved grain refinement in both the series of alloys is due to the increase in the concentration of AlB_2 particles creates more nucleation sites, and it is confirmed from the diffractograms (Figures 4.10 and 4.11), i.e., an increase in the intensity of AlB_2 (P-11) of B_{31} and B_{54} compared to B_{21} and B_{44} . Figure 4.13 k,l depicts the microstructure of alloys with the increase in Be and maintaining other elements constant, and observed a reduction in grain size from 144.74 to 128.71 in B_{62} and B_{72} alloys, and from 210.27 to 134.7 in B_{21} and B_{11} alloys , respectively. It is observed that increase in 0.1% of Be doesn't affect the grain size much and confirmed from XRD (Figure 4.12), whereas 0.3 wt.% of Be exhibits improved refinement as reported in the literature (Ergen et al. 2013; Zhu et al. 2009).

Secondary electron images of B doped alloys and EDS spectrum reveals that the B is in lower concentration in the center of the grain and it increases towards grain boundaries as shown in the EDS spectrum of the alloys (Figure 4.14 a - d), due to the segregation of B while quenching as discussed in the grain refinement mechanism. The distribution of Cu, Al, and B in the alloy are captured using elemental mapping, as shown in Figure 4.14 e.

4.3.3 Phase transformation temperatures

Phase transformation temperatures of the Cu-Al-Be-B alloys are presented in the Figures 4.15 – 4.18, and thermograms are represented with colored lines to differentiate the wt.% of B and its effect on hysteresis. The results are tabulated in Table 4.5.

It is clearly understood from thermogram (Figure 4.15), and Table 4.5, that increase in wt.% of B increases the transformation temperatures slightly and its enthalpies up to 0.08 wt.%, confirmed with the rise and shift of curves (B_{11} - B_{41}) away from the ordinate, and above 0.08 wt.% the transformation temperatures decreases can

be seen with the fall and shift of curves towards ordinate. The variations in the transformation temperatures are due to variations in the elemental composition of the matrix and precipitates. Increase in transformation temperatures are due to the increase in the concentration of insoluble particles, i.e., B and AlB_2 particles in the matrix requires additional energy for phase transformation, and also increase in e/a ratio (Turabi and Vance 2016). Increase in boron to 0.1 wt% and 0.15 wt.% decreases transformation temperatures due to increased density of AlB_2 particles in the matrix depletes the Cu and Al, and increase B changes e/a ratio lowers the transformation temperatures (Zhang et al. 2019). An increase in wt.% of B increases the thermal hysteresis irrespective of transformation temperatures.

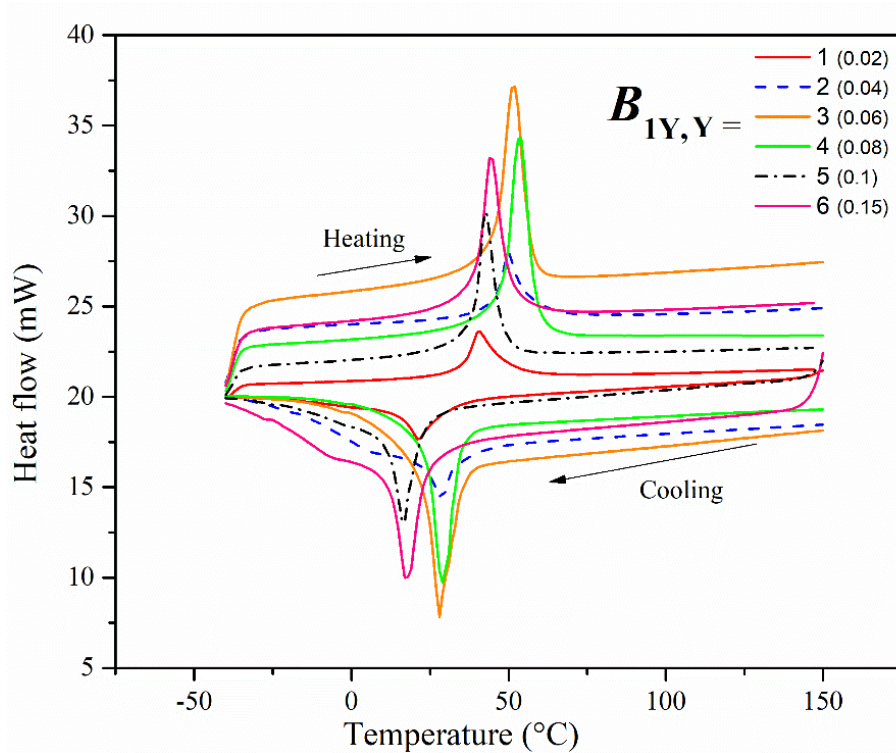


Figure 4.15 Thermogram – B_{1Y} SMAs.

Thermogram $B_{21} - B_{31}$ and $B_{44} - B_{54}$ (Figures 4.16, 4.17) presents that only increase in addition of Al decreases the transformation temperatures (Higuchi et al. 1982), i.e., curves B_{21} falls to B_{31} and B_{44} to B_{54} . shifts towards ordinate. Increase in 0.1 wt.% of Al from B_{21} to B_{31} reduces M_f , M_s , A_s and A_f by 10, 11, 12, 11 °C almost ~11 °C, without a change in thermal hysteresis, whereas increase in 0.3 wt.% of Al from

reduces M_f , M_s , A_s and A_f by 7, 20, 12, 18 °C with 3 °C reduction in thermal hysteresis as shown in Table 4.5.

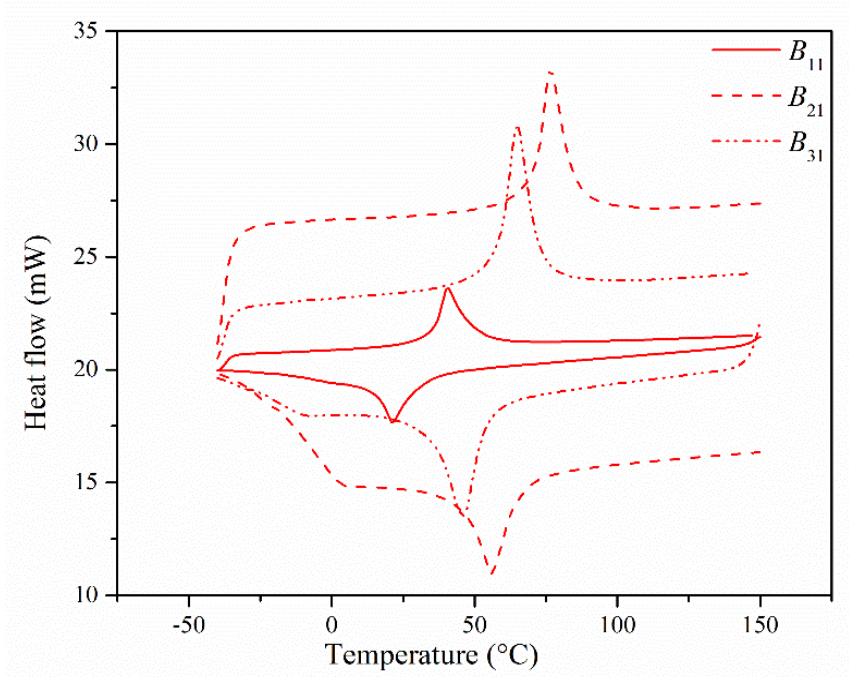


Figure 4.16 Thermogram – B_{11} , B_{21} and B_{31} SMAs.

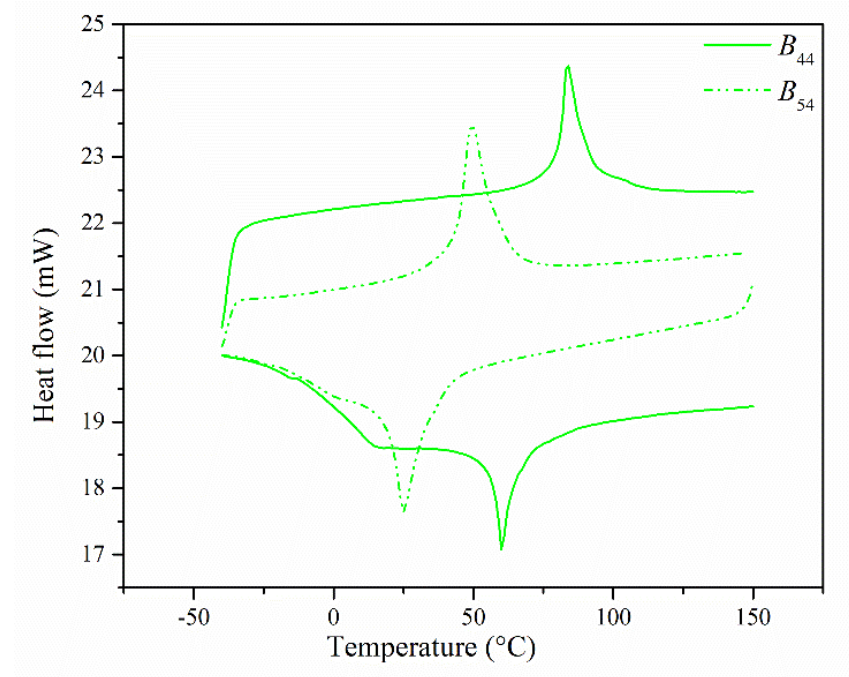


Figure 4.17 Thermogram – B_{44} , B_{54} SMAs.

Thermogram B_{62} , B_{72} (Figure 4.18), and B_{21} , B_{11} (Figure 4.16) present that only increase in Be, keeping other elements constant decreases the transformation temperatures. In the alloys B_{62} and B_{72} , increase in 0.1 wt.% of Be reduces M_f , M_s , A_s and A_f by 36, 30, 36, 33 °C with a slight increase in 2 °C of thermal hysteresis and shifts the curve towards ordinate, whereas in B_{21} and B_{11} alloys M_f , M_s , A_s and A_f reduces by 31, 35, 35, 35 °C, with fall and shift of curve towards ordinate.

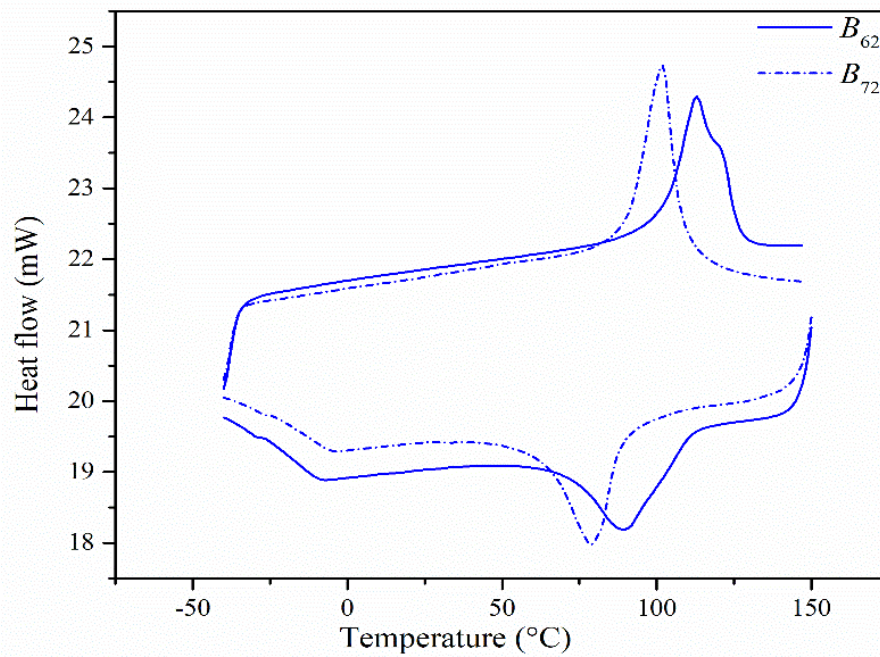


Figure 4.18 Thermogram – B_{62} , B_{72} SMAs.

Table 4.5 consists of temperatures, enthalpies, and hysteresis along with the amount of differences in transformation temperatures and hysteresis with the variation of wt.% of one element while keeping the remaining constant.

Table 4.5 Transformation temperatures, enthalpies, and hysteresis of Cu-Al-Be-B SMAs.

S. No	Alloy	M _f (°C)	M _s (°C)	ΔH _{A→M} (J/g)	A _s (°C)	A _f (°C)	ΔH _{M→A} (J/g)	Hysteresis (°C)
1.	B ₁₁	14	30	-6.2521	35	50	6.8865	20
2.	B ₁₂	22	34	-7.9965	45	56	7.6268	22
3.	B ₁₃	23	35	-16.5425	46	58	12.3201	23
4.	B ₁₄	24	34	-25.4059	49	59	14.0765	25
5.	B ₁₅	11	23	-11.7513	39	48	11.3864	25
6.	B ₁₆	12	23	-9.2654	39	51	10.3261	28
7.	B ₂₁	45	65	-7.2031	70	85	7.9448	20
8.	B ₃₁	35	54	-9.4016	58	74	10.5234	20
	Diff	10	11	2.1985	12	11	2.5786	0
9.	B ₄₄	56	64	-6.232	80	92	8.7203	28
10.	B ₅₄	20	34	-5.8253	44	59	7.3070	25
	Diff	36	30	0.4067	36	33	1.4133	- 3
11.	B ₆₂	69	108	-5.9189	101	127	7.3747	19
12.	B ₇₂	62	88	-6.6619	89	109	9.3347	21
	Diff	7	20	0.743	12	18	1.96	+ 2
13.	B ₂₁	45	65	-7.2031	70	85	7.9448	20
14.	B ₁₁	14	30	-6.2521	35	50	6.8865	20
	Diff	31	35	0.951	35	35	1.0583	0

4.3.4 Shape recovery ratio

The shape recovery ratio of the alloys was calculated by the bend test, and the results are presented in Figure 4.19.

The results depicted in Figure 4.19 convey only B_{1X} series, and B₅₄ alloys yield 100% recovery, and the rest exhibits poor recovery ratio. Complete recovery is due to the complete formation of martensite $\beta'_1 + \gamma'$ because of higher wt.% of Be and Al increases the martensite fraction. It is noticed that B₂₁ and B₃₁ yield 62.5% and 67.5% respectively, the poor recovery compared to the former alloys is due to the addition of

the lower amount of Be, i.e., 0.41 wt.% forms partial α_2 phase along with martensite and are not suitable for memory applications, because of the mixture of phases didn't exhibit shape recovery. But a slight increase in recovery, i.e., 5%, is noticed in B_{31} due to the 0.1% increase in Al, increases martensite fraction. In the alloys B_{44} and B_{54} , it is understood that, though an increase in addition of 0.45 wt.% of Be, the poor recovery is due to the difference of 0.3 wt.% of Al decreases the martensite fraction. B_{62} and B_{72} yield the lowest recovery ratio of the alloys, i.e., 38 % and 38.5 % due to the very low addition of Al, i.e., 11.3 wt.%, decreases the martensite fraction. B_{21} exhibits 100% recovery compared to B_{21} , i.e., 62.5% due to lower addition of Be, i.e., 0.41 wt.% Be. From the shape recovery ratio studies, it is concluded that alloys more than 0.41 wt.% of Be and 11.8 wt.% Al exhibits rapid and complete shape recovery suitable for actuator applications.

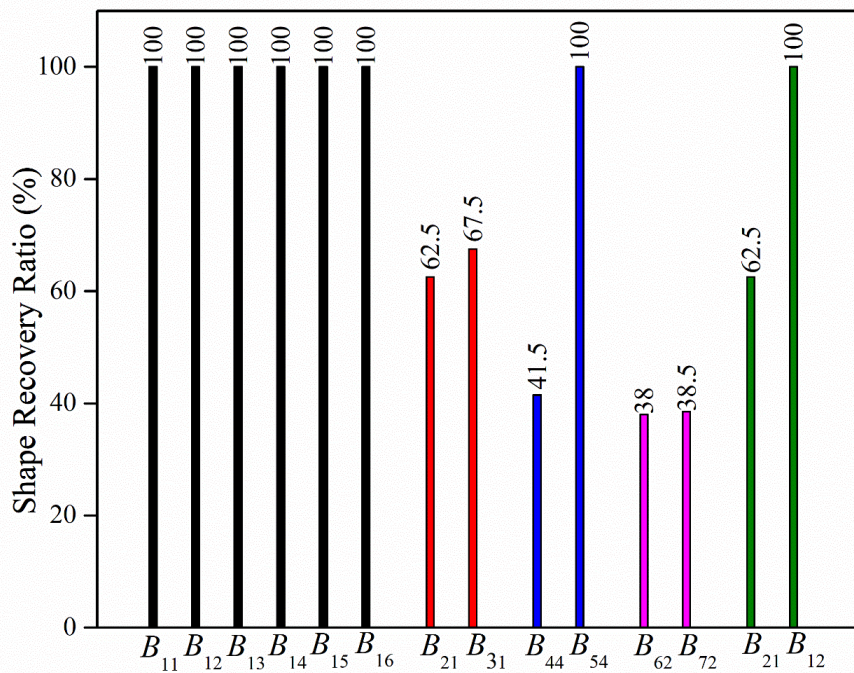


Figure 4.19 Shape recovery ratio of Cu-Al-Be-B SMAs.

4.3.5 Mechanical properties

Mechanical properties, i.e., ultimate tensile strength, ductility, yield stress, and yield strain of the boron modified Cu-Al-Be SMAs, are presented in Table 4.6 and also depicted in Figure 4.20.

Stress-strain curves show that an increase in B increases the tensile strength and ductility, attributes to (i) refined grains increases in the length of the grain boundary, takes more deviations for the propagation of the crack and requires more energy to move the dislocations(Yang et al. 2016a). (ii) increased cohesive strength at the grain boundaries due to the segregation of AlB₂.

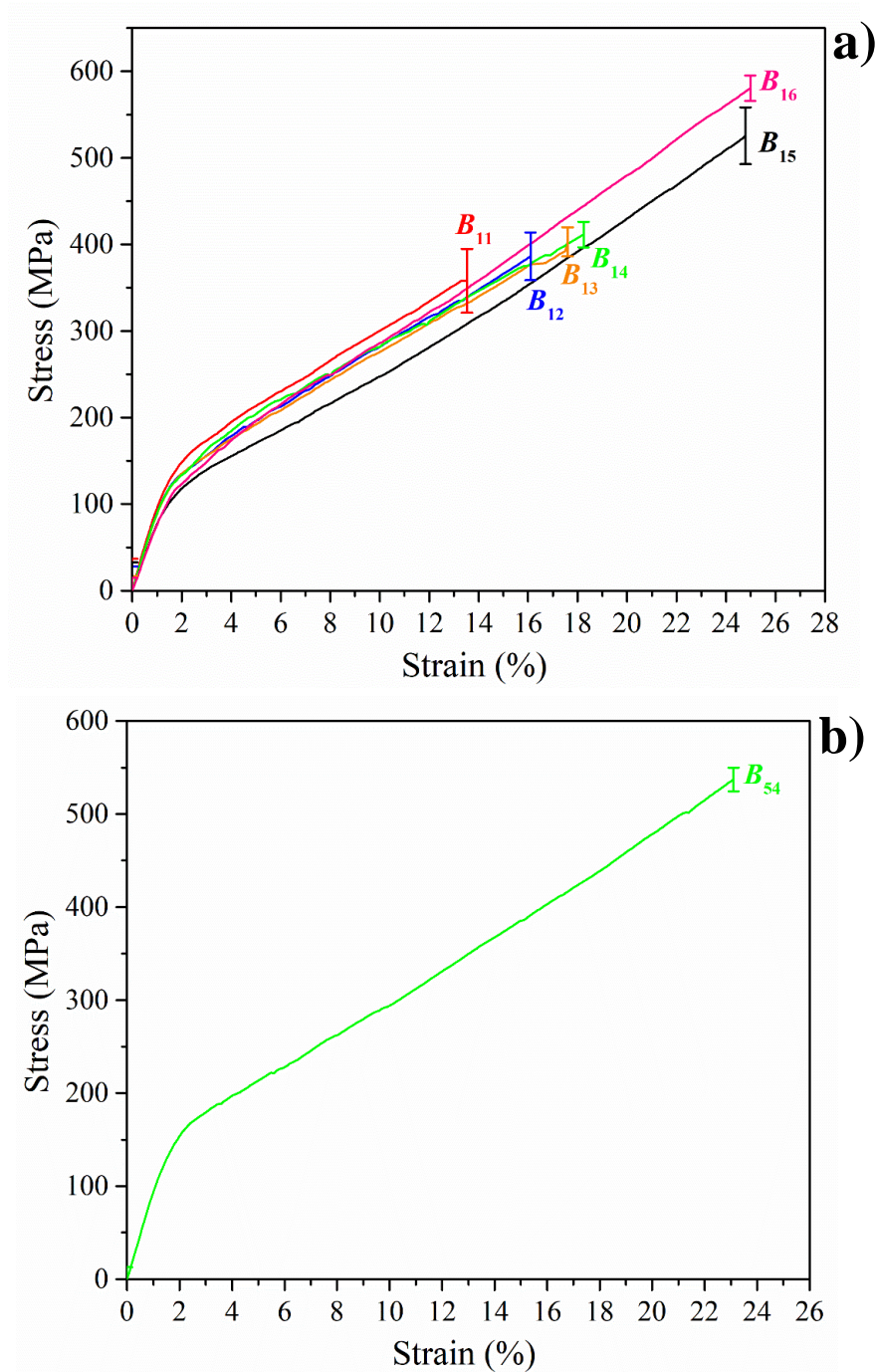


Figure 4.20 Stress strain curves of Cu-Al-Be-B SMAs.

Table 4.6 Mechanical Properties of Cu-Al-Be-B SMAs.

Alloy	Ultimate tensile strength (MPa)	Ductility (%)	Yield stress (0.2 %) (MPa)	Yield strain (0.2 %)
<i>B</i> ₁₁	358.14 ± 36.87	13.53 ± 2.08	106.80 ± 0.39	1.15 ± 0.06
<i>B</i> ₁₂	386.37 ± 27.64	16.12 ± 1.52	110.07 ± 0.35	1.31 ± 0.04
<i>B</i> ₁₃	403.01 ± 16.64	17.59 ± 1.49	109.79 ± 0.27	1.34 ± 0.02
<i>B</i> ₁₄	411.48 ± 12.23	18.24 ± 1.22	108.13 ± 0.16	1.29 ± 0.03
<i>B</i> ₁₅	521.65 ± 32.74	24.79 ± 0.68	104.10 ± 5.03	1.56 ± 0.16
<i>B</i> ₁₆	580.67 ± 12.67	24.98 ± 0.32	116.54 ± 4.37	1.72 ± 0.06
<i>B</i> ₅₄	537.19 ± 11.83	23.1 ± 0.36	137.53 ± 3.98	1.65 ± 0.04

Fracture morphology of boron modified SMAs exhibit a unique/different pattern as shown in Figure 4.21. The morphology/pattern resembles as elongated dimples/flutes, and the mechanism is not so clear and still investigation.

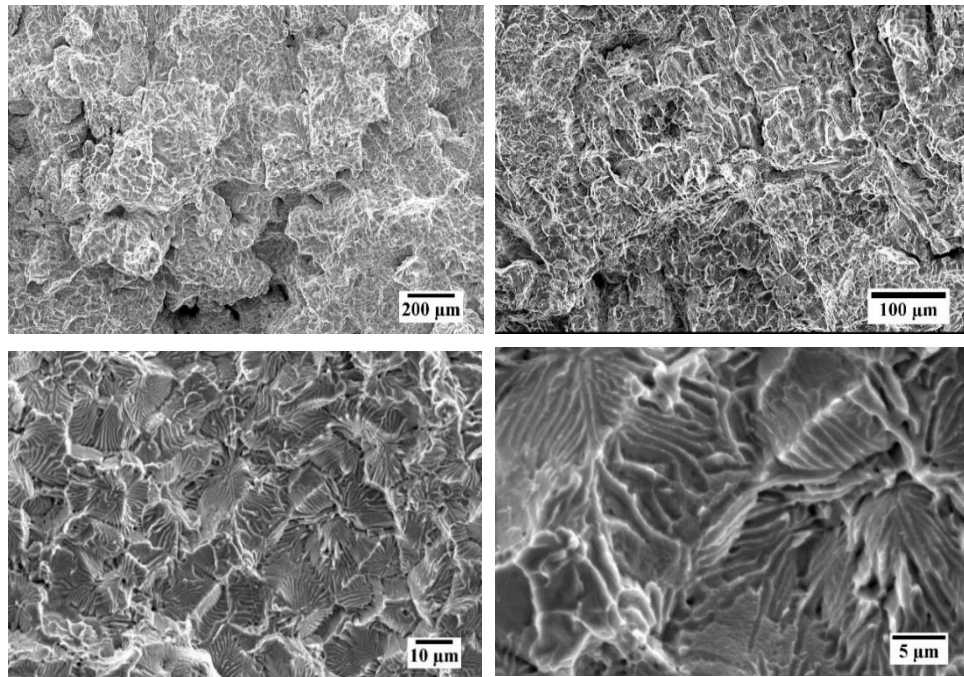


Figure 4.21 Fracture morphology of Cu-Al-Be-B SMA - *B*₁₆

4.4 Cu-Al-Be-Ce

Literature survey presents alloying cerium refines grains (Lu et al. 2009) and improves mechanical properties and increase in alloying of cerium forms rich fraction of secondary phase precipitates. This section presents the effect of inoculation of rare earth element cerium, i.e., 0.02 - 0.2 wt.% to Cu-Al-Be SMAs. Also, the effect of Ce on microstructure, phases, transformation temperatures, and shape recovery ratios are presented with detailed mechanisms. The elemental compositions and their designations are tabulated in Table 4.7, and the alloys are designated as “C_{XY},” ‘X’ represents the type of alloy, ‘Y’ represents the wt.% of cerium. Y = 1, 2, 3, 4,5,6 for 0.05, 0.1,0.15 and 0.2 wt.% of Ce, respectively. In this section, hypereutectoid alloys with cerium as grain refiner were presented.

Table 4.7 Elemental composition and designations of Cu-Al-Be-Ce SMAs.

S. No.	Alloy	Actual composition (wt.%)			Ce (wt.%)
		Cu	Al	Be	
1.	C ₁₀	87.58	12.00	0.42	0
2.	C ₁₁	87.53	12.00	0.42	0.05
3.	C ₂₃	87.52	11.90	0.43	0.15
4.	C ₃₃	87.95	11.45	0.45	0.15
5.	C ₃₄	87.88	11.47	0.45	0.20
6.	C ₄₁	87.58	11.90	0.47	0.05
7.	C ₅₄	87.33	12.00	0.47	0.20
8.	C ₆₃	87.61	11.80	0.49	0.15
9.	C ₆₄	87.61	11.80	0.49	0.20
10.	C ₇₂	87.43	12.00	0.52	0.10
11.	C ₇₄	87.48	12.00	0.52	0.20

4.4.1 XRD - Phases

Figure 4.22 depicts the diffractograms of the Cu-Al-Be-Ce SMAs. Colored lines, orange, brown, red, blue, and green, indicate 0, 0.05, 0.1, 0.15, and 0.2 wt.% of Ce, respectively. Diffractograms present betatized and quenched alloys are either completely martensite β'_1 (\blacklozenge -18R), or austenite β_1 (\heartsuit - DO₃) at room temperature, along with Al-rich precipitates, i.e., γ_2 (\bullet - Cu₉Al₄). Hypereutectoid alloys (Al \geq 11.8 wt.%) with \leq 0.49 wt.% of Be are completely martensite of β'_1 variants and a further increase in Be to 0.52 wt.% transforms martensite to metastable austenite β_1 . Addition and increase in Ce forms Al-rich or γ_2 (\bullet - Cu₉Al₄) precipitates confirmed from the intensity of the peak “ \bullet .”

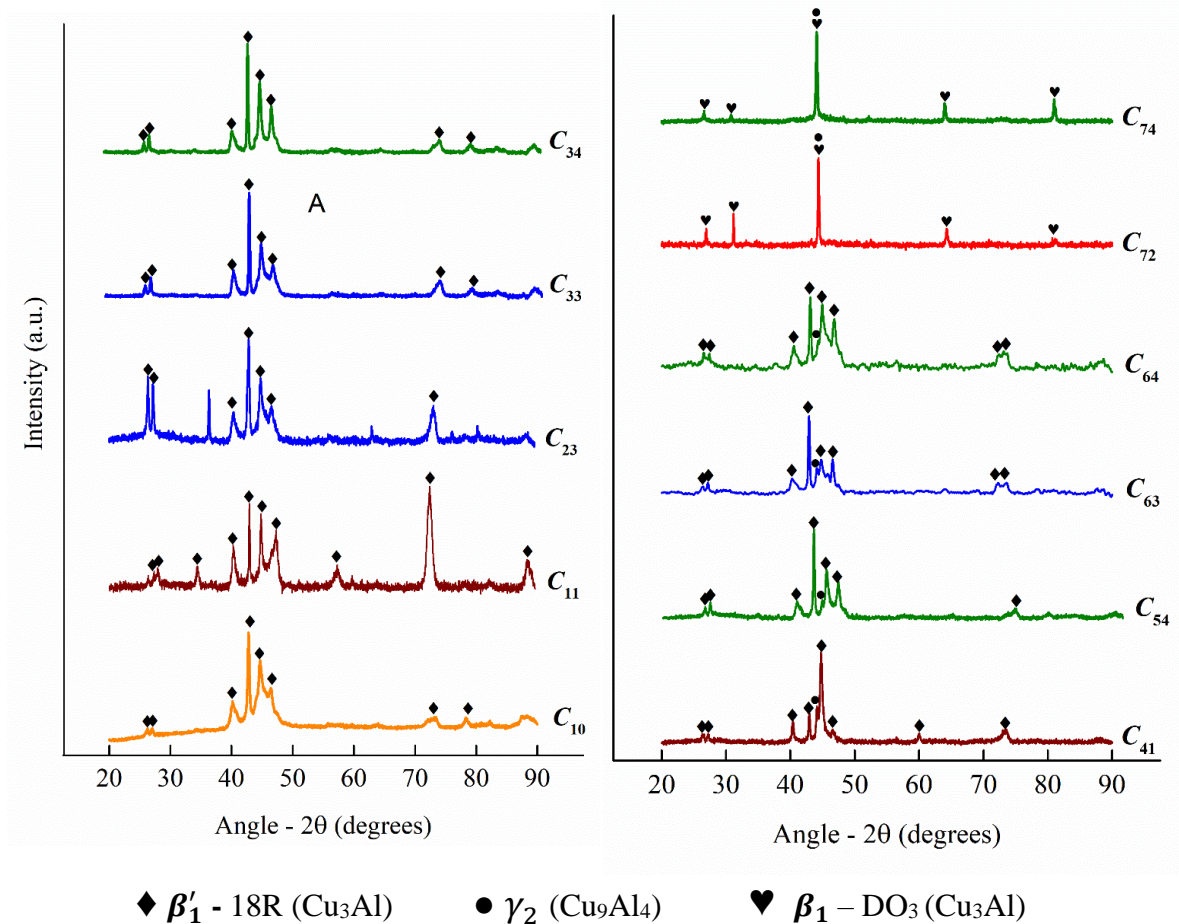
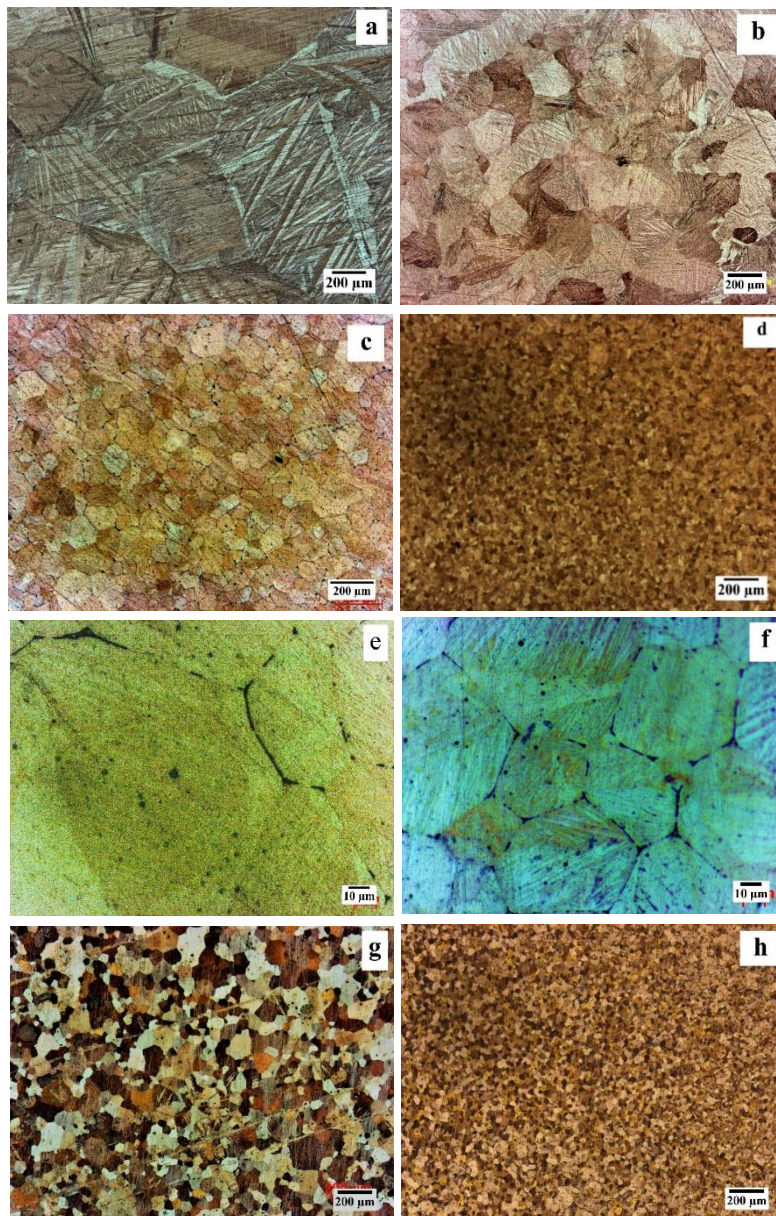


Figure 4.22 X-ray diffractograms of Cu-Al-Be-Ce SMAs.

4.4.2 Microstructure and morphology

Figure 4.23 depicts the microstructures of the alloys, including refinement of grains and grain boundary defects. Figure 4.24 presents the morphology, secondary phase particles present in the matrix, and at the grain boundaries along with their elemental composition obtained from EDS.



50X - (a) C_{10} , (b) C_{11} and C_{41} , (c) C_{23} , C_{33} and C_{63} , (d) C_{34} , C_{54} and C_{64} , (g) C_{72} , and (h) C_{74} ; 500X - (e) C_{63} and (f) C_{64} .

Figure 4.23 Microstructures of Cu-Al-Be-Ce SMAs.

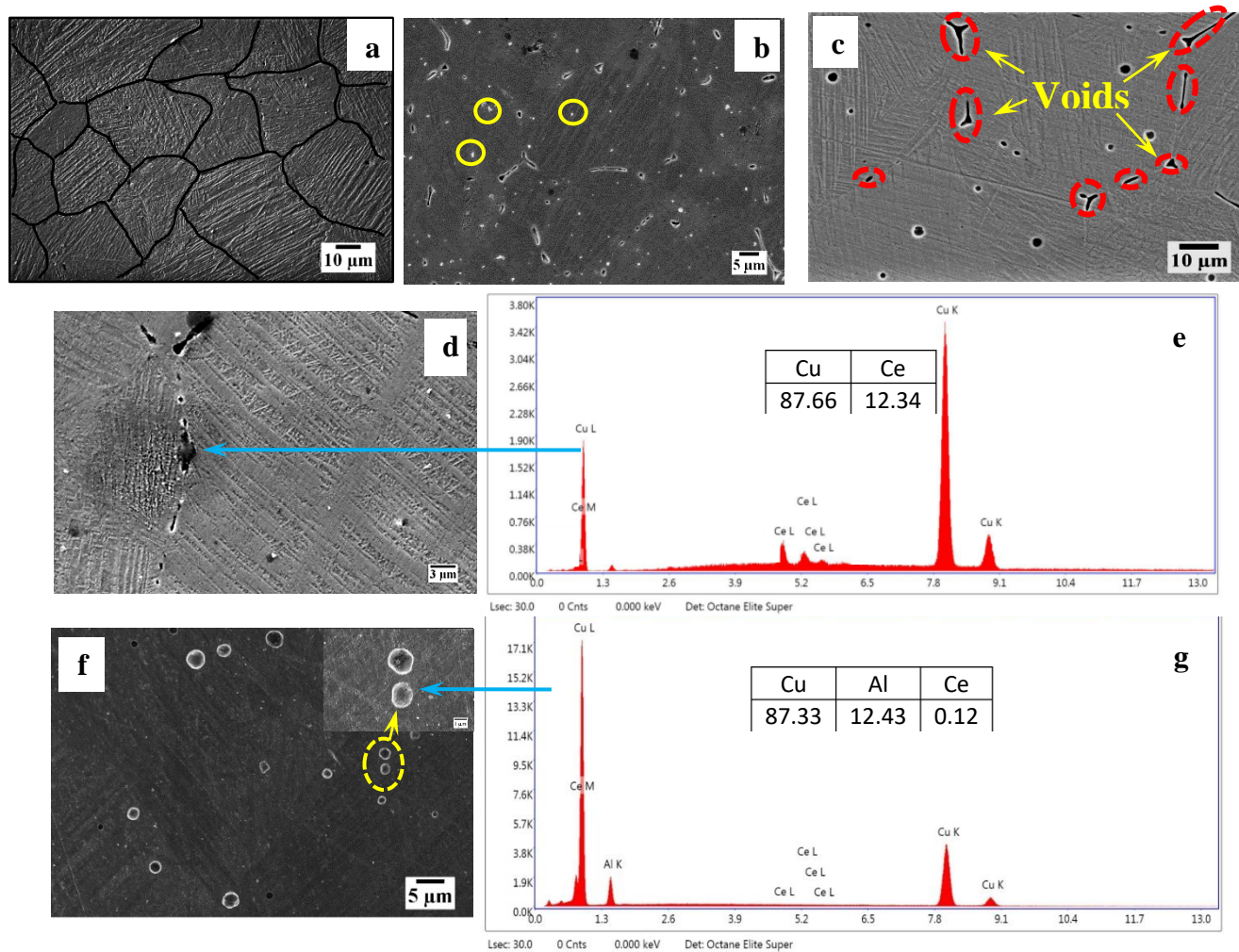


Figure 4.24 SEM images of Cu-Al-Be-Ce SMAs. (a) C_{11} , (b) C_{34} , (c) C_{63} , (d) C_{33} and (f) C_{64} , EDS spectrums: (e) C_{33} and (g) C_{64} .

Addition and increase in Ce refine the grains, and the grain sizes were determined from the micrographs using the linear intercept method. C_{10} exhibit coarse grains (Figure 4.23 a) with an average grain size of $463.45 \pm 10 \mu\text{m}$. Alloying Ce of 0.05 wt.% in both C_{11} and C_{41} , reduces the grain size to $135 \pm 12 \mu\text{m}$ and exhibit serrated grains (Figure 4.23 b and Figure 4.24 a). An increase in Ce to 0.1 wt.% refine the grain size to $85 \pm 12 \mu\text{m}$ and has bimodal grains (Figure 4.23 g) in C_{72} . Further, an increase in Ce to 0.15 wt.% in C_{23} , C_{33} , and C_{63} decrease the grain size to $75 \pm 10 \mu\text{m}$ (Figure 4.23 c). An increase in Ce to 0.2 wt.% refines the grain size to $25 \pm 10 \mu\text{m}$, and are nearly equiaxed grains (Figure 4.23 d and h) in C_{34} , C_{54} , C_{64} , and C_{74} . The percentage of reduction is 0, 70.87, 82.73, 83.8 and 94.6% for 0, 0.05, 0.1, 0.15 and 0.2 wt.% of Ce, respectively.

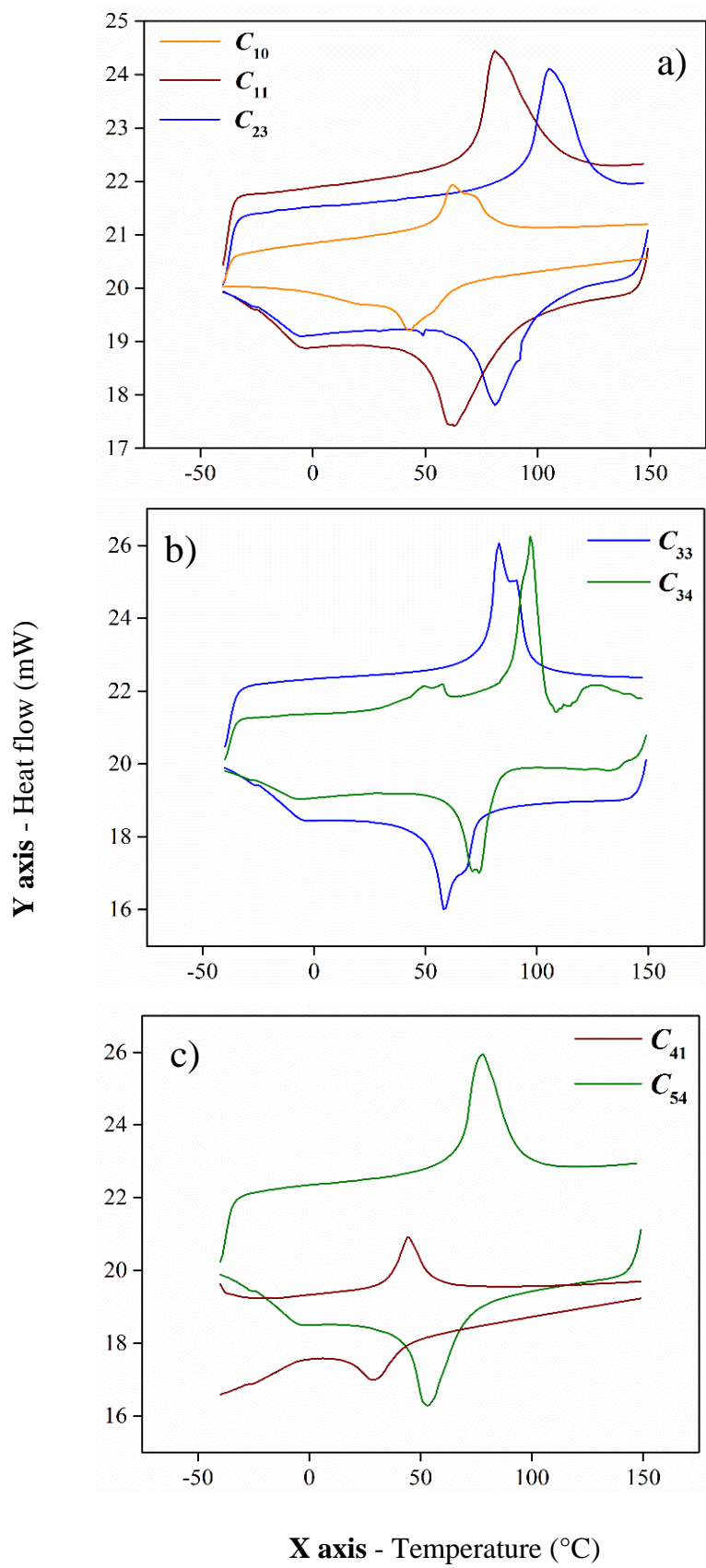
Salient observations from the microstructures and secondary electron images are addition and increase in Ce exhibit grain refinement, serrated to equiaxed grain transition, the formation of Al-rich secondary phase particles, viz. γ_2 - Cu₉Al₄ precipitates and void coalescence at the boundaries attributes to:

- (i) **Grain refinement:** The maximum solid solubility of cerium in copper is 0.05 wt.% (Duisemaliev and Presnyakov 1964) and 0.01 wt.% in Al (K.A. Gschneidner and Calderwood 1988). Thus, the alloyed/inoculated cerium particles are highly insoluble in the matrix and accumulate at the grain boundaries owing to the larger difference in the atomic radius of Cu, Al, Be, and Ce. A minor fraction of Ce at the grain boundaries forms CeO₂ (Figure 4.23 e, f, and Figure 4.24 d) particles due to its active chemical properties and high affinity at elevated temperatures. Thus the insoluble Ce and CeO₂ particles at the grain boundaries inhibit grain growth (Guniputi and Murigendrappa 2018).
- (ii) **Serrated to equiaxed transition:** Increase of Ce to 0.05 and 0.1 wt.% forms serrated (Figure 4.23 b and Figure 4.24 a) and bimodal grains (Figure 4.23 g), respectively, due to the addition of lower wt.% causes inhomogeneous distribution and irregular segregation of insoluble Ce along the grain boundaries, as observed in the boron modified alloys (Narasimha and Murigendrappa 2020).

- (iii) **Secondary phase particles:** Insoluble particles of Ce react with Al, which is highly electronegative and trivalent, forms Al-rich precipitates in the matrix. It is worth noting from diffractograms and secondary electron images of alloys that Al-rich precipitates increase their size with an increase in wt.% of Al followed by Ce and Be. Aluminium rich precipitates are very fine and bright particles of size ranging between 0.1 - 0.2 μm (encircled regions in Figure 4.24 b) in C_{11} to C_{34} , whereas precipitate size grows as γ_2 - Cu_9Al_4 of size ranging between 1 – 3 μm (encircled regions in Figure 4.24 f) in C_{41} to C_{74} and confirms from the presence of peak “●” in the diffractograms of C_{41} to C_{74} compared to C_{11} to C_{34} .
- (iv) **Micro voids:** Insoluble CeO_2 particles at the grain boundaries/junctures form microvoids (encircled regions in Figure 4.24 c) while quenching. An increase in Ce increases the fraction of voids due to enriched Ce particles at the boundaries.

4.4.3 Phase transformation temperatures

Figure 4.25 depicts the thermograms of the betatized and quenched Cu-Al-Be-Ce SMAs, and Table 4.8 presents the transformation temperatures, enthalpies, and hysteresis. Alloying and increase in Ce increases the transformation temperatures, as shown in thermograms (Figure 4.25 a, b, and d) and Table 4.8, and also observed that though variation in 0.1 wt.% of Al in C_{41} and C_{54} exhibit an increase in temperatures. Higher the increase in wt.% of Ce, larger the rise in transformation temperatures. Increase in wt.% of Al decreases the transformation temperatures in both Cu-Al and Cu-Al-Be SMAs, whereas the present investigation reveals an increase in transformation temperatures, attributes to alloying Ce forms precipitates of “ γ_2 ” (Cu_9Al_4) in the grains, as discussed in Section 4.4.2, which reduces Al in the matrix. Increase in Be decreases the transformation temperatures can be observed from C_{54} and C_{74} and also from Figure 4.25 d. Increase in Ce, increase the hysteresis, and the same can be seen from the thermograms.



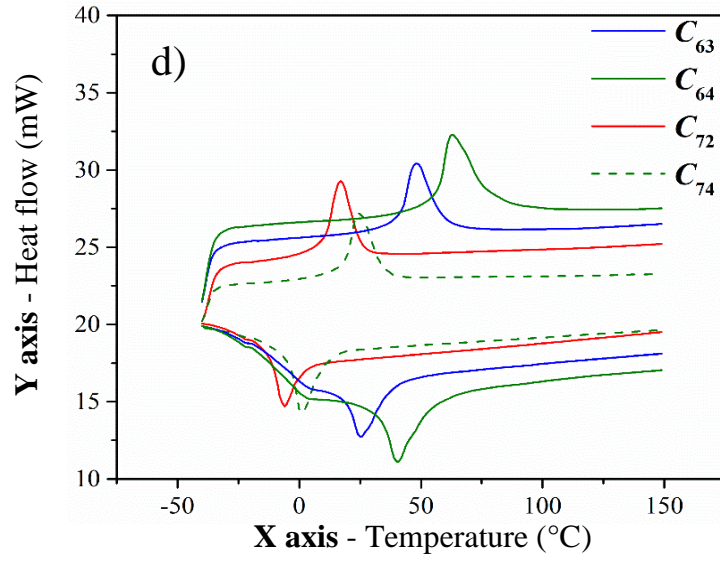


Figure 4.25 Thermograms of Cu-Al-Be-Ce SMAs.

Table 4.8 Transformation temperatures, enthalpies, and hysteresis of Cu-Al-Be-Ce SMAs

S. No	Alloy	M_f (°C)	M_s (°C)	$\Delta H_{A \rightarrow M}$ (J/g)	A_s (°C)	A_f (°C)	$\Delta H_{M \rightarrow A}$ (J/g)	Hysteresis (°C)
1.	C_{10}	31	56	-14.8280	54	81	9.7952	25
2.	C_{11}	50	80	-6.3558	73	104	7.6577	24
3.	C_{23}	69	95	-5.7393	95	124	7.1737	29
4.	C_{33}	52	73	-6.4432	78	96	8.1424	23
5.	C_{34}	63	80	-5.2719	92	103	6.4814	23
6.	C_{41}	17	42	-6.9546	37	55	9.3387	13
7.	C_{54}	44	66	-5.9550	68	93	6.9015	27
8.	C_{63}	18	36	-9.9631	41	59	10.5309	23
9.	C_{64}	32	52	-7.6686	57	79	10.7477	27
10.	C_{72}	-12	2	-6.2615	10	26	7.1283	24
11.	C_{74}	-5	11	-10.5162	19	33	9.5488	23

4.4.4 Shape recovery ratio

The shape recovery ratio of the alloys was measured by the bend test, and the results are depicted in Figure 4.26.

. Alloys with $Ce \leq 0.05$ wt.% exhibits complete recovery and alloys with an increase in $Ce > 0.05$ wt.% shows deterioration in the shape recovery ratios. Reduction in the recovery ratio is due to the pinning effect viz. enriched precipitates of Ce, CeO_2 particles (Figure 4.24d) at grain boundaries, and precipitates of “ γ_2 ” (Figure 4.24f) in the matrix hampers the movement of plates (Kustov et al. 2004b). It is also observed that microvoids (Figure 4.23e and Figure 4.24c) at the grain boundaries/junctures will lead to the decohesion of grains in the strained condition of an actuator while functioning. Typically, the decohesion propagates throughout the boundary and leads to fatal failure of the actuator in the real-time applications. However, alloys C_{33} and C_{34} exhibit the least recovery as compared to the rest, due to the lesser wt.% of Al forms a lower fraction of martensite.

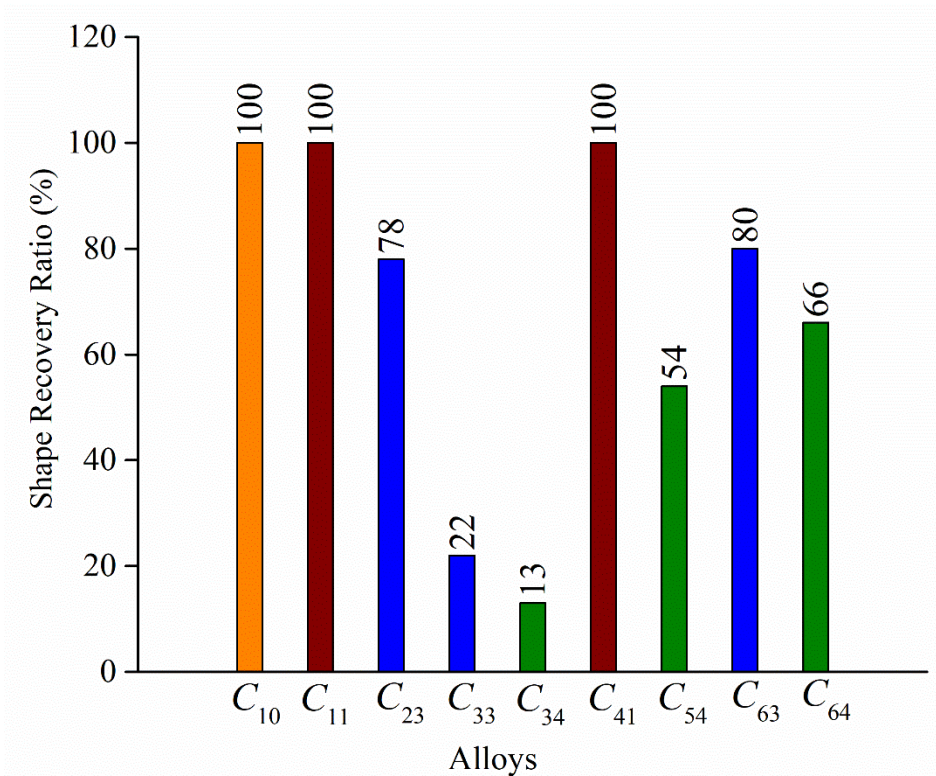


Figure 4.26 Shape recovery ratio of Cu-Al-Be-Ce SMAs.

4.5 Cu-Al-Be-Gd

Literature survey presents alloying gadolinium improves mechanical properties (Zhang et al. 2016), and this section presents the effect of inoculation of rare earth element gadolinium, i.e., 0.05 - 0.15 wt.% to Cu-Al-Be SMA T_5 . Also, the effect of Gd on microstructure, phases, transformation temperatures, and shape recovery ratios are presented with detailed mechanisms. The elemental compositions and their designations are tabulated in Table 4.9.

Table 4.9 Elemental composition and designations of Cu-Al-Be-Gd SMAs.

S. No.	Alloy	Actual composition (wt.%)			Gd (wt.%)
		Cu	Al	Be	
1.	T_5	87.58	12.00	0.42	0
2.	G_1	87.69	11.86	0.41	0.04
3.	G_2	87.67	11.84	0.41	0.08
4.	G_3	87.51	11.95	0.42	0.13

4.5.1 XRD - Phases

Figure 4.27 depicts the X-ray diffractogram of Cu-Al-Be-Gd SMAs. It is confirmed from peaks of (\diamond), the alloys primarily consist of β'_1 and small amount of γ_1^1 martensite. It is observed that the addition of Gd up to G_2 increases in peak width (FWHM) with decreases in intensity, attributes to refined crystallite size. Further, it is noticed that an increase in Gd gives rise to peaks of Al_4Cu_5Gd (*) precipitate phases with an increase in intensity. The intermetallic phase Al_4Cu_5Gd (*) has no crystal structure as confirmed from the ICDD 00-042-1047 datasheet (A.P. Prevarskii and Kuzma 1988; Riani and Perrot n.d.)

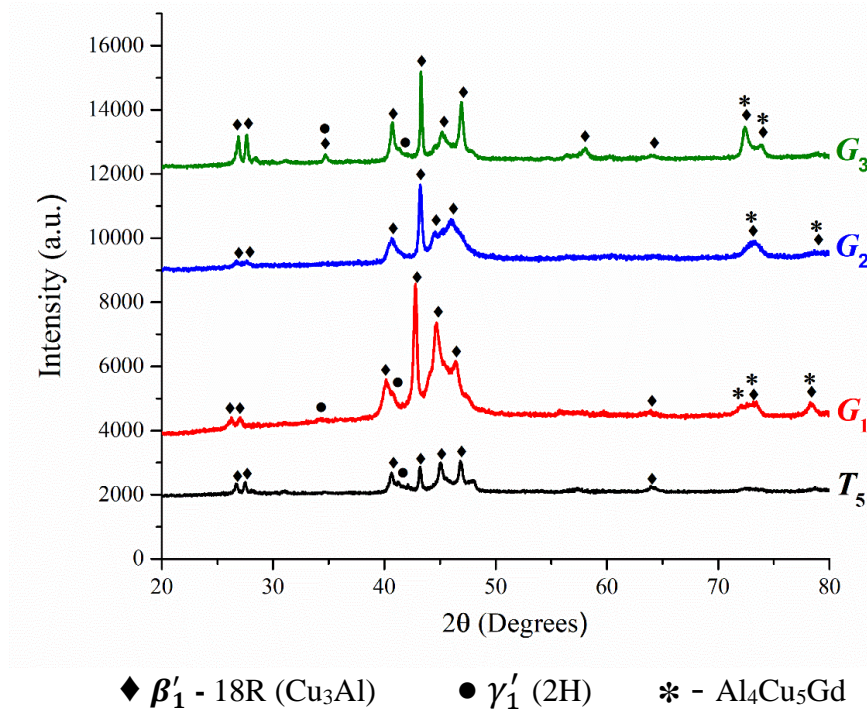
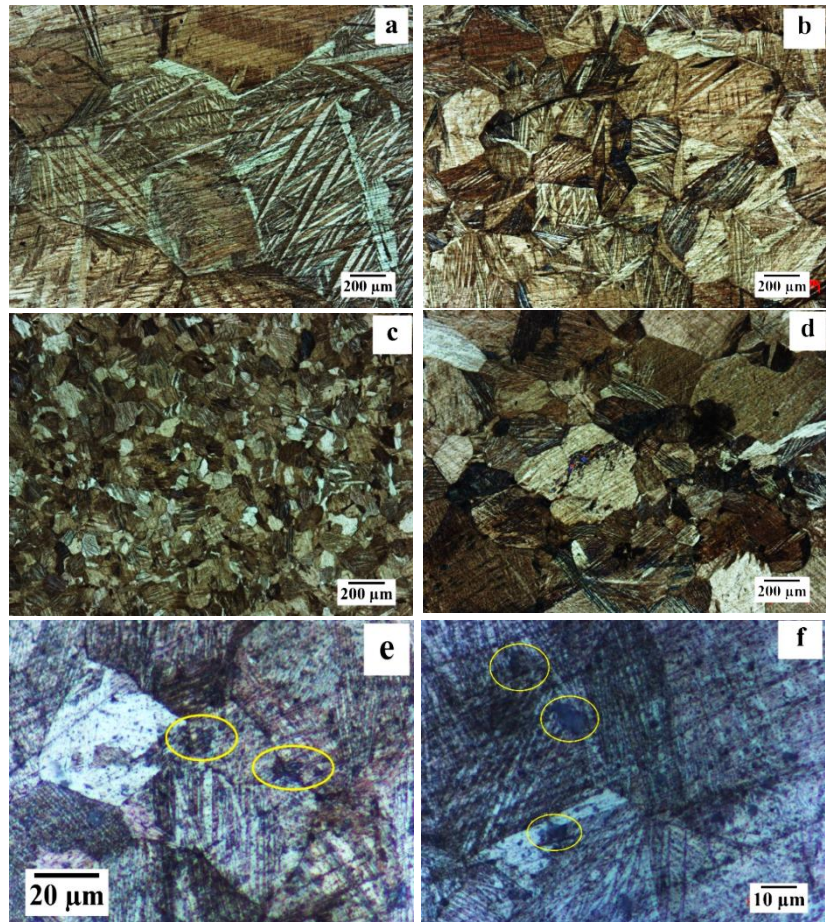


Figure 4.27 X-Ray Diffractogram of Cu-Al-Be-Gd SMAs.

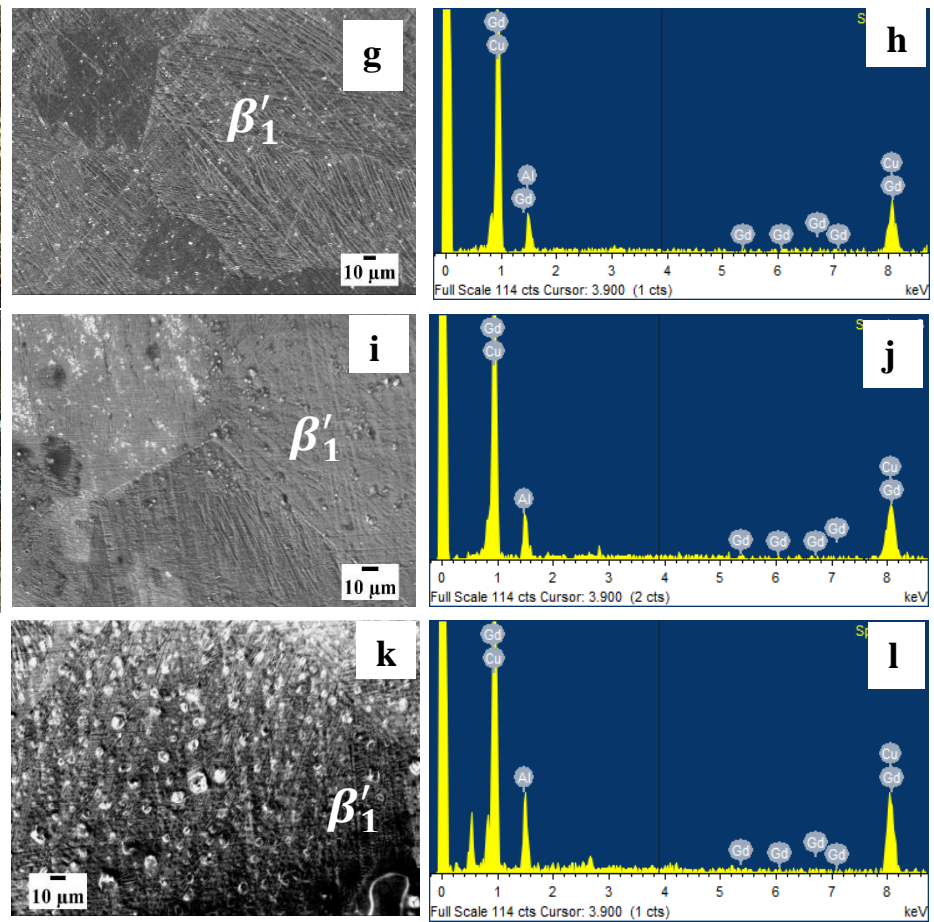
4.5.2 Microstructure and morphology

Figure 4.28 depicts the microstructure of Cu-Al-Be-Gd SMAs and evinced that all the alloys possess equiaxed grains in longitudinal and transverse directions. G_0 has coarse grains, as shown in Figure 4.28 a with an average grain size of $463.45 \pm 10 \mu\text{m}$, and the addition of Gd decreases the grain sizes to $217.23 \mu\text{m}$ and $81.80 \mu\text{m}$ for 0.04 and 0.08 wt. %, respectively, as shown in Figure 4.28 b and c. Further, it is seen that the grain size increased to $214.61 \mu\text{m}$ as the Gd increases more than 0.1 wt.%. The percentage reductions of grain size are 53.12 %, 82.34 %, and 53.69 % for G_1 , G_2 , and G_3 alloys. It is seen that increase in gadolinium up to 0.08 wt. % forms very fine precipitates in the alloy matrix, further addition of Gd is highly insoluble and forms big precipitates (black layer in the ellipse) and agglomerates at the grain boundary presented in Figure 4.28 e and f. The SEM images of betatized and quenched Cu-Al-Be-Gd SMAs are presented in Figure 4.29. An increase in gadolinium increases the size, and the fraction of Gd enriched precipitates ($\text{Al}_4\text{Cu}_5\text{Gd}$) can be seen as white dots and globules, as shown in Figure 4.29a, c, and e. The EDS analysis observed that the increase in the intensity of peaks with the increase of precipitates from Figure 4.29b, d, and f.



(a) $G_0 - 50\times$, (b) $G_1 - 50\times$, (c) $G_2 - 50\times$, (d) $G_3 - 50\times$, (e) $G_3 - 100\times$ and (f) $G_3 - 500\times$.

Figure 4.28 Microstructures of Cu-Al-Be-Gd SMAs.



Morphology:(g) G_1 , (i) G_2 and (k) G_3 , and EDS: (h) G_1 , (j) G_2 and (l) G_3 .

Figure 4.29 SEM images of Cu-Al-Be-Gd SMAs.

The grain refinement mechanism is attributed to the following two processes:

- i. Heterogeneous nucleation – diffusion of fine particles of gadolinium in the alloy acts as nucleation sites, in turn, increases the number of grains.
- ii. Insoluble gadolinium – ascribed to the differences in the atomic radius of the elements, viz. larger the radius of Gd is arduous to dissolve in the smaller radii of Cu-Al-Be matrix, agglomerates at the grain boundary inhibit the grain growth.

4.5.3 Phase transformation temperatures

DSC studies yield the forward and reverse martensitic transformation temperatures of the alloys as shown in Figure 4.30, and their associated enthalpies as presented in Table 4.10 .

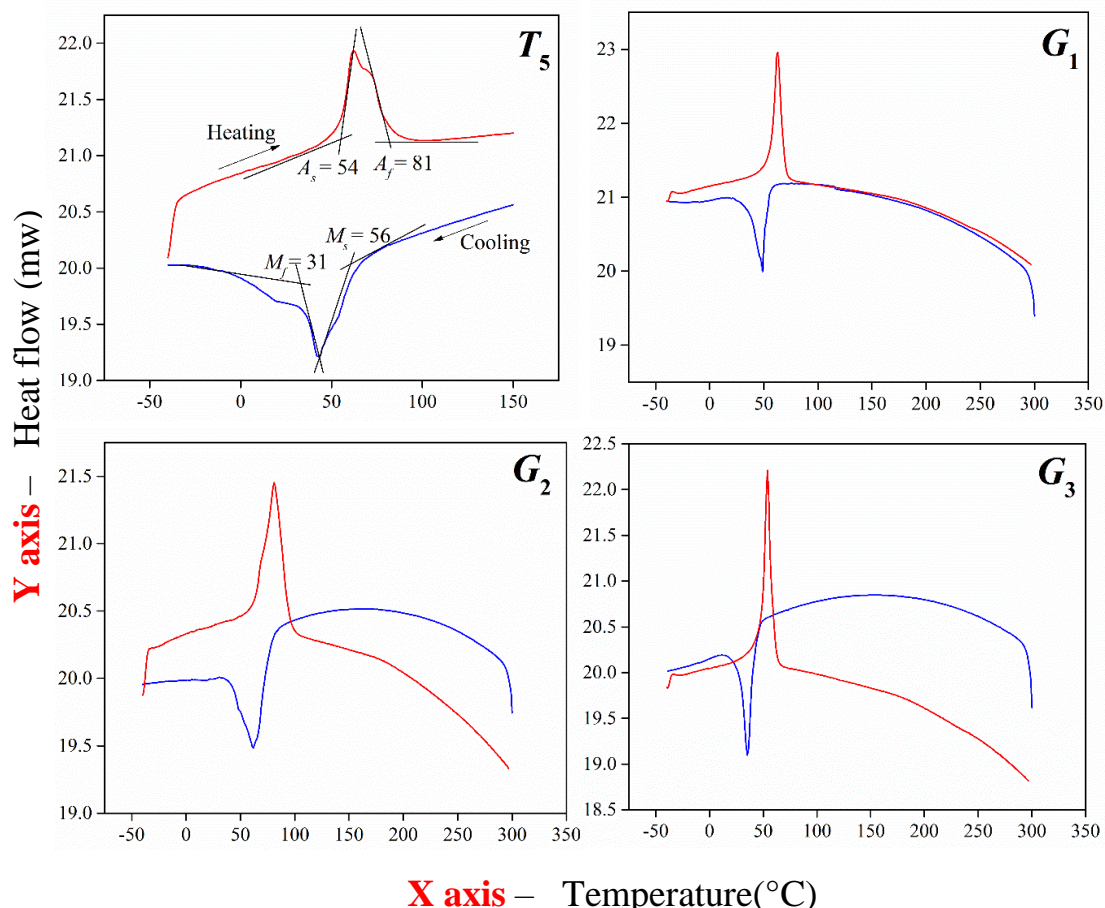


Figure 4.30 Thermograms – Cu-Al-Be-Gd SMAs.

Table 4.10 Transformation temperatures, enthalpies, and hysteresis of Cu-Al-Be-Gd SMAs.

S. No	Alloy	M_f (°C)	M_s (°C)	$\Delta H_{A \rightarrow M}$ (j/g)	A_s (°C)	A_f (°C)	$\Delta H_{M \rightarrow A}$ (j/g)	Hysteresis (°C)
1.	T_5	31	56	-14.8280	54	81	9.7952	25
2.	G_1	41	51	- 5.7165	56	80	+ 8.0929	29
3.	G_2	39	74	- 6.4361	63	96	+ 11.4664	29
4.	G_3	27	40	- 6.0064	49	58	+ 8.4527	22

The results indicate that the addition of gadolinium increases the transformation temperatures up to 0.08 wt. % and then decreases. It is also noted that the values of enthalpy in forward transformation were higher than the reverse transformation, because of the addition of energy is more in the forward transformation than reverse transformation. Variations in transformation temperatures and enthalpies are due to depletion of Be, increase of Al, and formation of insoluble Gd precipitates and intermetallics alter the elemental composition. It is also noted that the thermal hysteresis of T_5 is narrow compared to G_1 , G_2 , and G_3 , not suitable for the rapid response applications (Ramaiah et al. 2014).

4.5.4 Shape recovery ratio

The shape recovery ratio of the T_5 , G_1 , G_2 , and G_3 alloys was investigated experimentally by the bend test and presented in Figure 4.31. It is noticed that the shape recovery ratios were decreased with an increase in gadolinium, the reduction in recovery attributes to the following mechanisms:

- i. Pinning effect - enriched precipitates of gadolinium or intermetallics (Al_4Cu_5Gd) hampers the martensite plates movement (Kustov et al. 2004b), requires additional energy for phase transformation (Ozkul et al. 2017).
- ii. Disordered lattice due to precipitates (Xu 2008c).

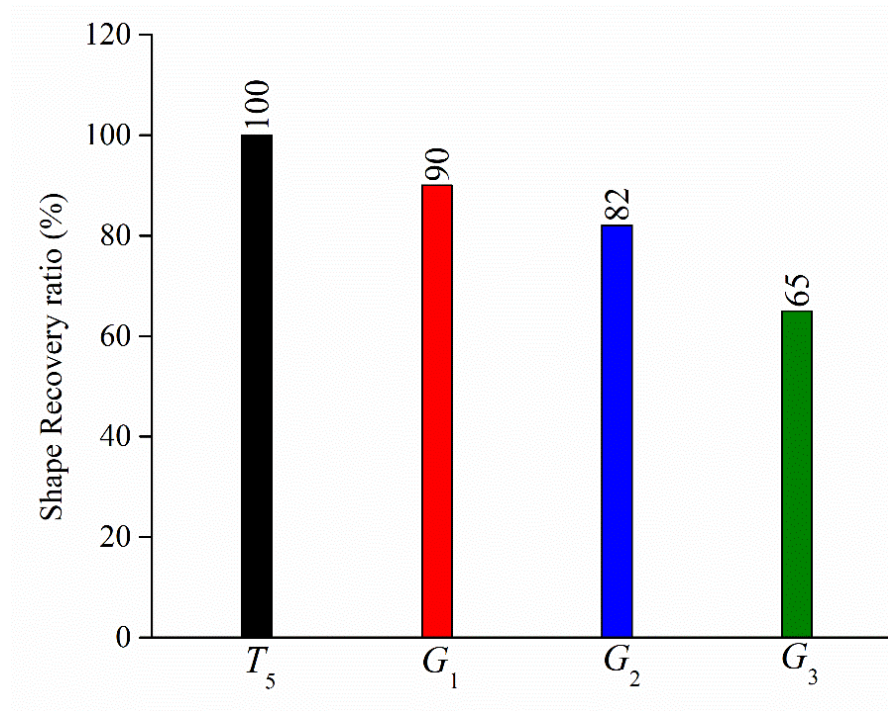


Figure 4.31 Shape recovery ratio of Cu-Al-Be-Gd alloys

4.5.5 Mechanical Properties

Stress-strain curves obtained from the monotonic tensile tests of the alloys are presented in Figure 4.32, and the values are tabulated in Table 4.11. Curve T_5 unveils that alloy without grain refinement has an ultimate tensile strength of 363 ± 35 MPa with the ductility of $10.80 \pm 0.75\%$ till fracture. Curve G_1 and G_2 represent an increase in tensile strength to 433 ± 7 and 577 ± 6 MPa, and ductility 18.99 ± 1.75 and $20.92 \pm 2.06\%$ with the increase in gadolinium of 0.04 and 0.08 wt. % respectively, attributes to grain refinement increases the grain boundary area (Yang et al. 2016b), and the precipitates (Candido et al. 2012; Melo et al. 2009) in the matrix requires more energy to move the dislocations. The curve G_3 indicates a drop in tensile strength and ductility to 301 ± 9 MPa and $11.85 \pm 0.18\%$, respectively, due to agglomeration of enriched gadolinium at the grain boundary, causes decohesion leads to weakening of grain boundary transforms ductile to brittle fracture, as presented in fracture surface of alloys Figure 4.33 d.

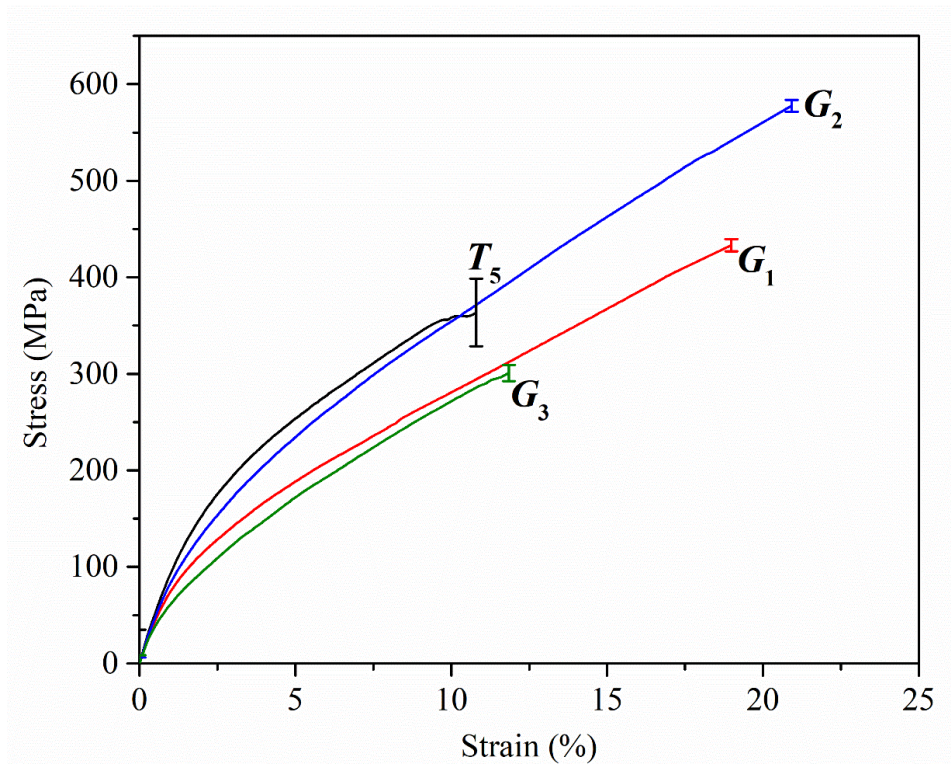


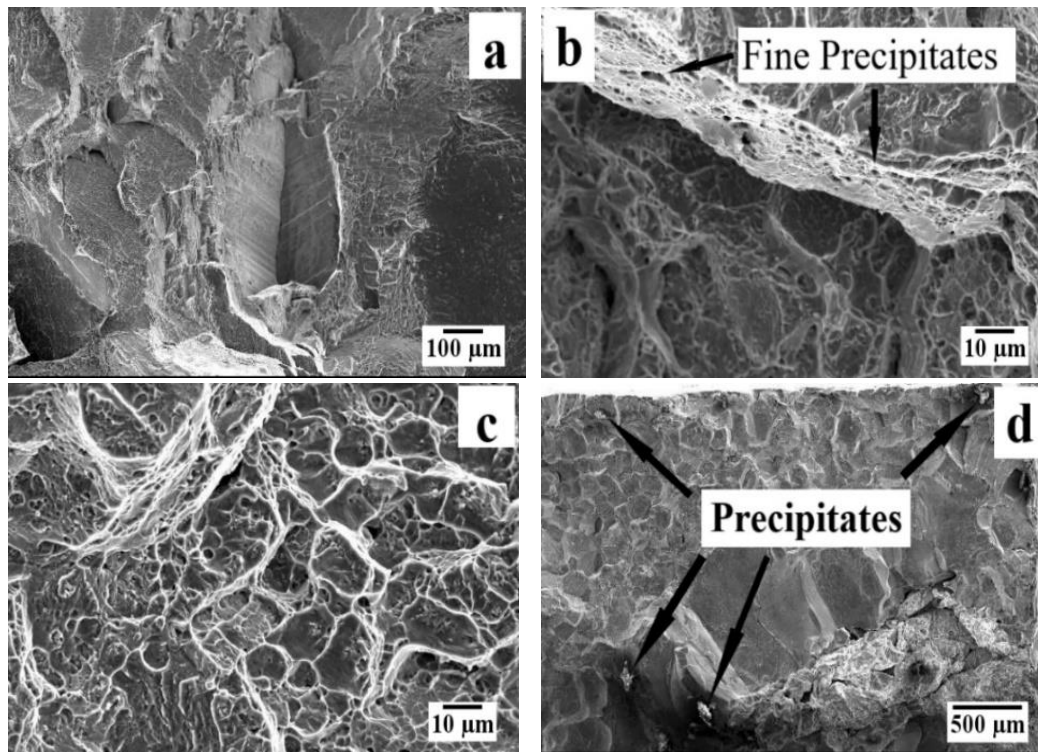
Figure 4.32 Stress- strain curves of Cu-Al-Be-Gd SMAs.

Table 4.11 Mechanical properties of Cu-Al-Be-Gd SMAs.

Alloy	Ultimate tensile strength (MPa)	Ductility (%)	Yield stress (0.2 %) (MPa)	Yield strain (0.2 %)
T_5	363 ± 35	10.80 ± 0.75	132.34 ± 8.40	1.60 ± 0.03
G_1	433 ± 7	18.99 ± 1.75	66.64 ± 4.48	0.84 ± 0.05
G_2	577 ± 6	20.92 ± 2.06	77.82 ± 6.76	0.88 ± 0.11
G_3	301 ± 9	11.85 ± 0.18	50.72 ± 3.18	0.73 ± 0.02

Figure 4.33 presents the fracture morphology of Cu-Al-Be-Gd SMAs, reveals that the type and root of failure. It is clearly observed that G_0 fails in cleavage mode, as shown in Figure 4.33 a. Fractured surface of G_1 alloy indicates quasi cleavage failure as shown in Figure 4.33 b, viz. fracture takes place within grains due to the fine Gd enriched precipitates. Increase of gadolinium in G_2 alloy completely transformed to ductile fracture with the coalescence of microvoids (dimples) as shown in Figure 4.33

c, due to the precipitates, further addition of Gd causes ductile to brittle transition, G_3 alloy fails quickly in an intergranular mode attributes to the agglomeration of gadolinium precipitates weakens the grain boundary as shown in Figure 4.33 d.



(a) T_5 , (b) G_1 , (c) G_2 , and (d) G_3

Figure 4.33 Fracture morphology of Cu-Al-Be-Gd SMAs.

4.6 Cu-Al-Be-Mn

Based on the literature survey, alloying manganese improves ductility (Masamichi et al. 1989; Matsushita et al. 1985) of Cu-Al SMAs. The proceeding subsections present the effect of alloying of manganese from 0.1 – 1.0 wt.% to eutectoid and hypereutectoid Cu-Al-Be SMAs only. Also, the effect of Mn on microstructure, phases, transformation temperatures, and shape recovery ratios are presented with detailed mechanisms. The elemental compositions and their designations are tabulated in Table 4.12, and the alloys are designated as “ M_X ,” ‘M’ represents the type of alloy, ‘X’ represents the wt.% of manganese. X = 1, 2, 3, 4, and 5 for 0.1, 0.2, 0.3, 0.5 and 1.0 wt.% of Mn, respectively.

Table 4.12 Elemental composition and designations of Cu-Al-Be-Mn SMAs.

S. No	Alloy	Actual composition (wt.%)			Mn (wt.%)
		Cu	Al	Be	
1.	M_1	87.36	12.00	0.41	0.23
2.	M_2	87.02	12.20	0.41	0.37
3.	M_3	86.71	12.30	0.41	0.58
4.	M_4	86.58	12.00	0.42	1.00
5.	M_5	86.42	12.10	0.42	1.06
6.	M_6	87.55	11.90	0.43	0.12
7.	M_7	87.12	11.90	0.43	0.55
8.	M_8	86.73	11.84	0.43	1.00
9.	M_9	87.21	12.23	0.43	0.13
10.	M_{10}	87.32	11.90	0.45	0.33

4.6.1 XRD - Phases

Figure 4.34 depicts the diffractograms of betatized and quenched Cu-Al-Be-Mn SMAs. Colored lines red, blue, brown, green, and orange represents 0.1, 0.2, 0.3, 0.5, and 1.0 wt.% of Mn, respectively. Diffractograms reveals M_1 possess β'_1 martensite,

whereas M_2, M_6, M_7 and M_9 exhibit coexistence of martensites, $\beta'_1 + \gamma'_1$ i.e., a mixture of orthorhombic and monoclinic variants. M_3, M_4, M_5 , and M_8 exhibit pure austenite β_1 of DO₃ order.

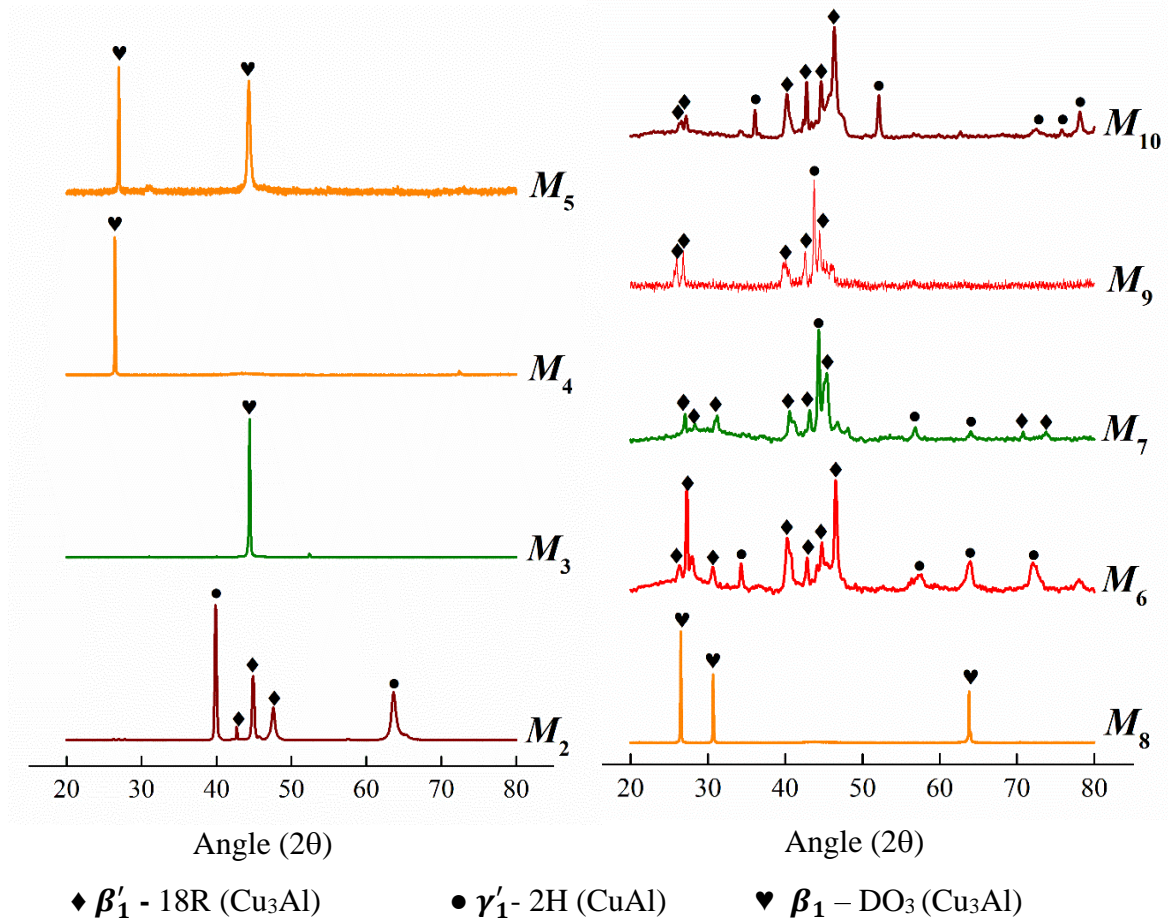


Figure 4.34 X-ray diffractograms of Cu-Al-Be-Mn SMAs.

In general, the coexistence of martensites formation takes place above 12.3 wt.% Al in Cu-Al alloys, as shown in Figure 4.1, whereas the salient observations from the XRD analysis are as follows:

- (i) Addition of 0.1 wt.% of Mn in M_6 exhibit the mixture of martensites formation at 11.9 wt.% of Al, in contrast, ternary SMA T_9 with same elemental composition (11.9Al, 0.43Be) exhibit only β'_1 martensite.
- (ii) M_2 exhibit the mixture of martensites at 0.41 wt.% of Be, whereas B_{23} SMA at 0.41 wt.% of Be exhibit mixture of α and β'_1 martensite phases are due to the increased addition of both Al and Mn.

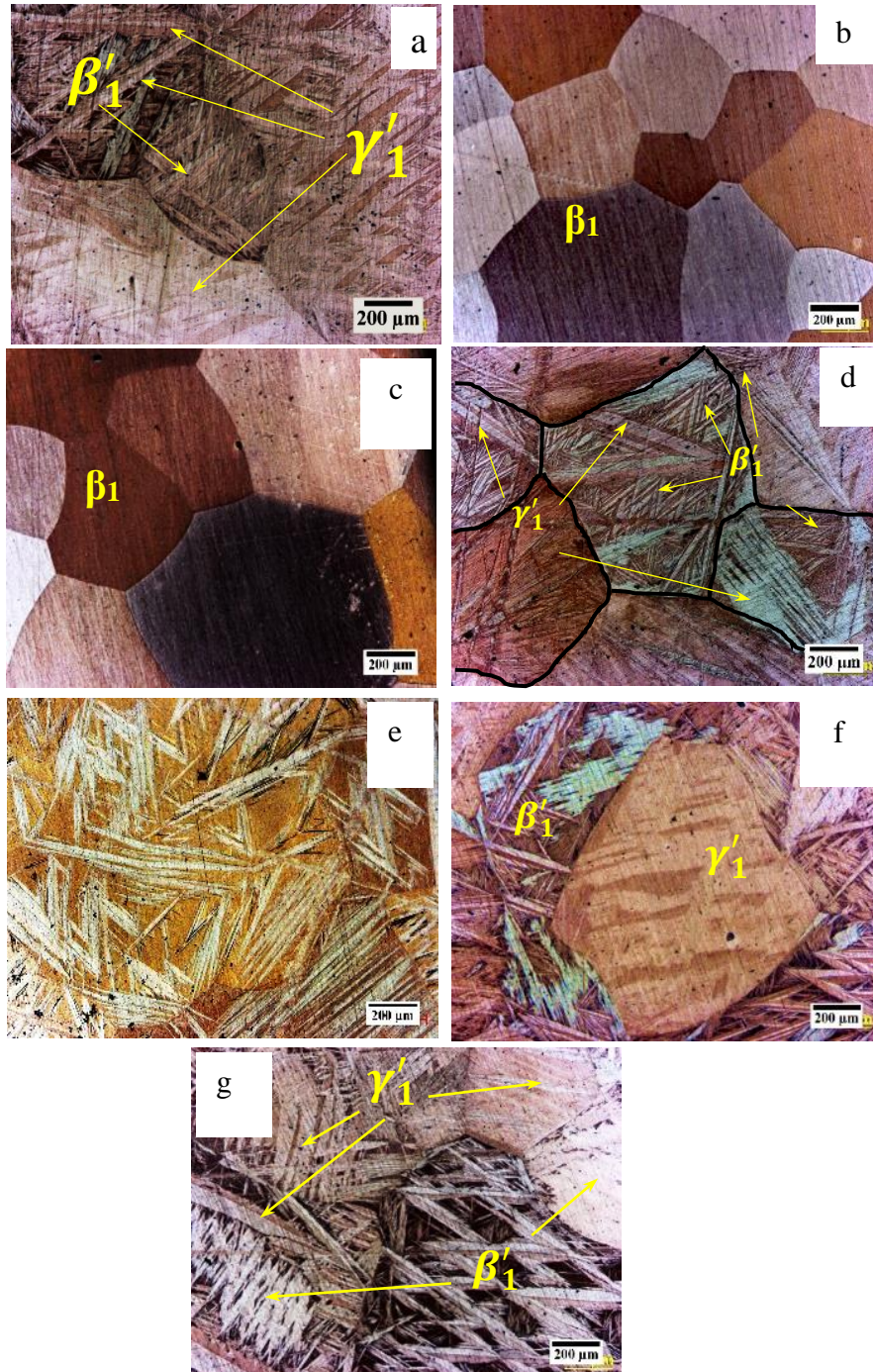
- (iii) An increase in Mn to 0.55 wt.% in M_7 increases the fraction of monoclinic martensite and confirms from XRD (Figure 4.34) and microstructure(Figure 4.35).
- (iv) Addition of 1.0 wt.% of Mn in M_4 exhibit pure austenite, whereas ternary alloy T5 with same elemental composition exhibit pure β'_1 martensite. M_3 and M_5 also exhibit pure austenite instead of a mixture of martensites as in Cu-Al alloy, due to the increased addition of both Al and Mn.
- (v) SMAs with ≤ 0.55 wt.% of Mn forms martensites of either β'_1 or coexistence of β'_1 and γ'_1 , and > 0.55 wt.% of Mn forms metastable austenite " β_1 ".
- (vi) Minor change in wt.% of Be didn't exhibit phase, and martensite modification and Mn plays a significant role in the modification of phases followed by Al and Be.

From the XRD analysis, It is worth noting that shift in the domain of mixture of martensites morphology (Figure 4.1) to lower Al concentration is due to the addition of Mn (Sutou et al. 2001) as seen in ternary Cu-Al-Mn system (Figure 2.10) followed by Be (Higuchi et al. 1982) and Al. The coexistence of martensites occurs in a narrow composition range, solely depends on the elemental composition and the quenching medium temperature as observed in Cu-Al-Ni (Van Humbeeck et al. 1987) and Cu-Zn-Al-Ni-Mn (J.H. Yang et al. 1987) SMAs.

4.6.2 Microstructure and Morphology

Figure 4.35 shows the microstructures of betatized and quenched Cu-Al-Be-Mn SMAs, and it is evident that the grains are coarse and bimodal. An increase in Mn didn't exhibit significant grain refinement (Masamichi et al. 1989). The average grain sizes of the SMAs are 537.25 ± 10 , 470.35 ± 13 , 547.27 ± 20 , 460.28 ± 13 , 590.23 ± 13 , 573.65 ± 13 , 327 ± 20 , 593.28 ± 13 , 584.32 ± 11 and 596.14 ± 14 μm for M_1 , M_2 , M_3 , M_4 , M_5 , M_6 , M_7 , M_8 , M_9 , and M_{10} respectively. Microstructures of M_1 , M_2 , M_6 , M_7 , M_9 , and M_{10} exhibit the coexistence of martensites, i.e., $\beta'_1 + \gamma'_1$ (Figure 4.35 a, d, e, f, and g) as confirmed from Section 4.6.1. An increase in Al, i.e., ≥ 11.8 wt.% increases the fraction of β'_1 martensite and it is predominant compared to γ'_1 as shown in Figure 4.35c, e, f, and h, and confirms from the intensities of X-ray diffractograms (Figure

4.34). Besides, M_3 , M_4 , M_5 , and M_8 with ≥ 0.55 wt.% of Mn are of pure austenite (Figure 4.35 b and c) of DO₃ order confirms from the X-ray diffractograms (Figure 4.34).

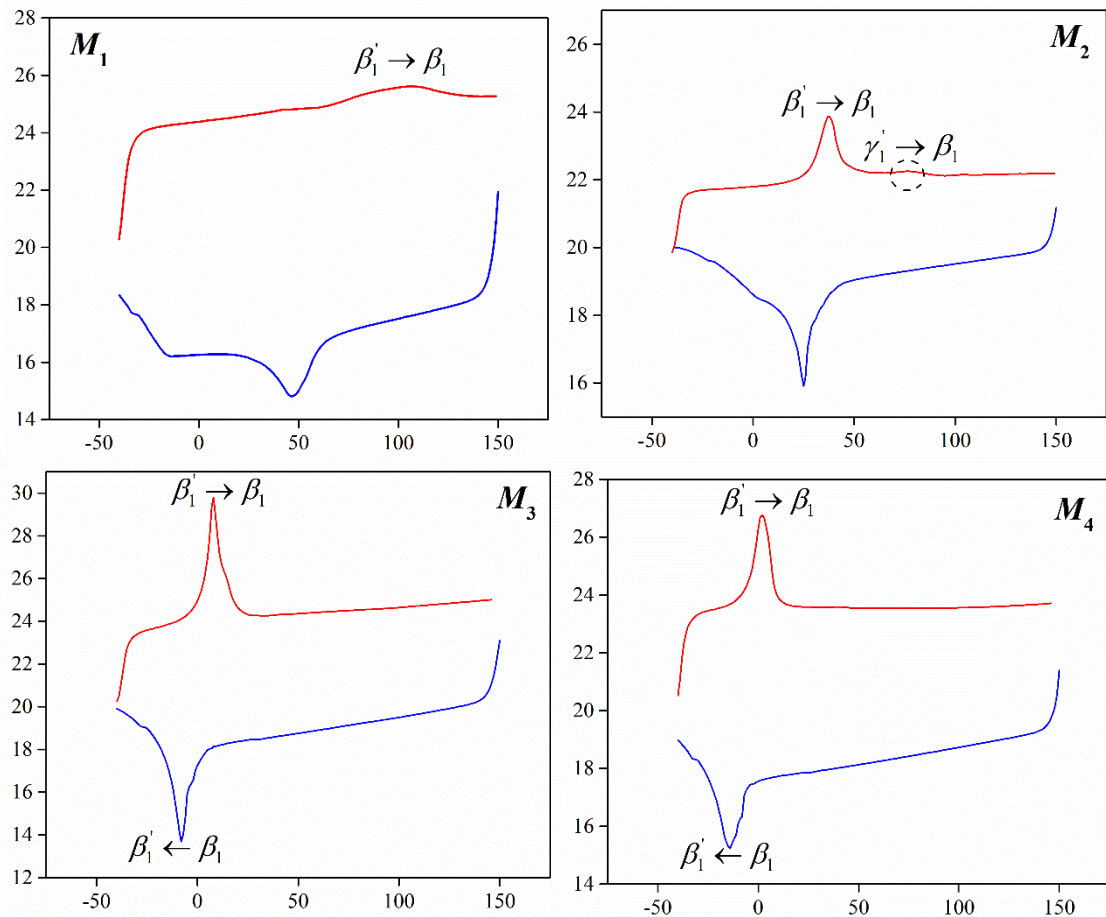


50X - (a) M_1 , (b) M_3 , (c) M_4 , (d) M_6 , (e) M_7 , (f) M_7 , and (g) M_9 .

Figure 4.35 Microstructures of Cu-Al-Be-Mn SMAs.

4.6.3 Phase transformation temperatures

Figure 4.36 depicts the thermograms of the water quenched Cu-Al-Be-Mn SMAs. Thermograms of M_3 , M_4 , M_5 , and M_8 exhibit only one endothermic event representing a single-stage transformation of martensite to austenite, i.e., $\beta'_1 \rightarrow \beta_1$, attributes to the existence of only β'_1 martensite or β_1 austenite in the SMAs, as discussed in Section 4.2.2 and 4.2.3. Alloys M_1 , M_2 , M_6 , M_7 , M_9 , and M_{10} exhibit two endothermic events represent two-stage martensitic reverse transformation, due to the coexistence of martensites (Van Humbeeck et al. 1987; J.H.Yang et al. 1987). The first endothermic peak in the lower temperature side represents the transformation of $\beta'_1 \rightarrow \beta_1$ and the second endothermic peak in the higher temperature side represents the transformation from $\gamma'_1 \rightarrow \beta_1$. It is also observed that no interval/gap in the transformation between $\beta'_1 \rightarrow \beta_1$ and $\gamma'_1 \rightarrow \beta_1$, and the size and shape of the peaks describes the enthalpy required for reverse transformation. It is also observed that an increase in wt.% of Al, Be, and Mn decreases the transformation temperatures and are tabulated in Table 4.13.



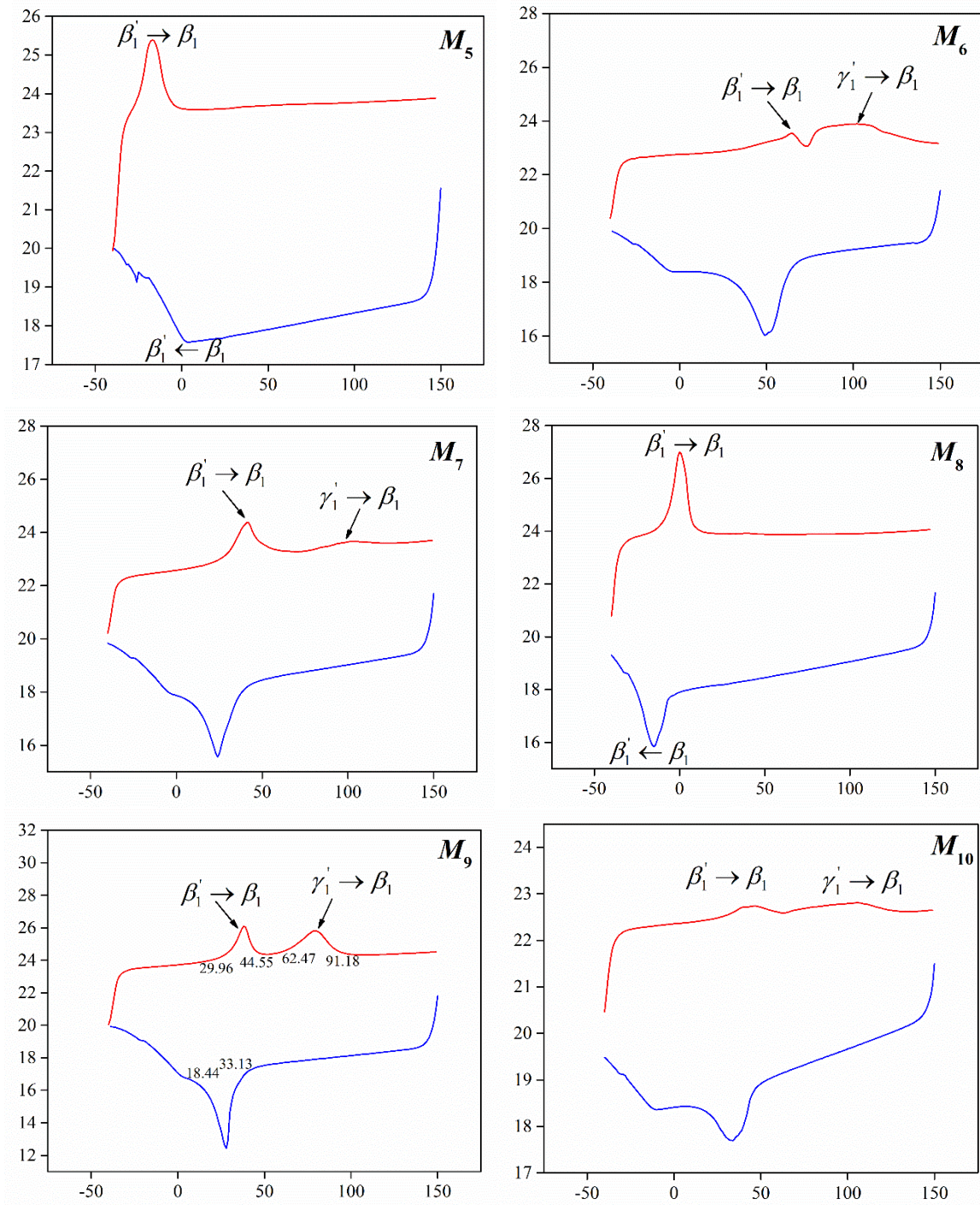


Figure 4.36 Thermograms of Cu-Al-Be-Mn SMAs.

Table 4.13 Transformation temperatures of Cu-Al-Be-Mn SMAs.

S. No	Alloy	Mf (°C)	Ms (°C)	As1 (°C)	Af1 (°C)	As2 (°C)	Af2 (°C)
1.	M_1	31	61	--	--	78	128
2.	M_2	19	28	36	52	66	92
3.	M_3	-15	-3	--	--	4	14
4.	M_4	-24	-4	--	--	-5	9
5.	M_5	--	--	--	--	-27	-7
6.	M_6	34	62	59	72	74	115
7.	M_7	12	34	31	52	81	117
8.	M_8	-25	-7	--	--	-7	7
9.	M_9	18	33	30	45	63	91
10.	M_{10}	17	47	26	62	62	126.63

Note: Mf – martensite finish temperature, Ms – martensite start temperature
As1 – Transformation start of $\beta'_1 \rightarrow \beta_1$, Af1 – Transformation finish of $\beta'_1 \rightarrow \beta_1$.
As2 – Transformation start of $\gamma'_1 \rightarrow \beta_1$, Af2 – Transformation finish of $\gamma'_1 \rightarrow \beta_1$.

4.6.4 Shape recovery ratio

The shape recovery ratio of the alloys was measured by the bend test, and the results are depicted in Figure 4.37, observed maximum recovery of 35%. The poor recovery is due to (i) lattice mismatch/disorder attributes to a mixture of martensites and (ii) γ'_1 (2H) peak lags in transformation as compared to β'_1 , and the same can be seen from the broader second endothermic peak in thermograms of M_2, M_6, M_7, M_9 , and M_{10} , attributes to the coarse martensite plates of 2H (Figure 4.35).

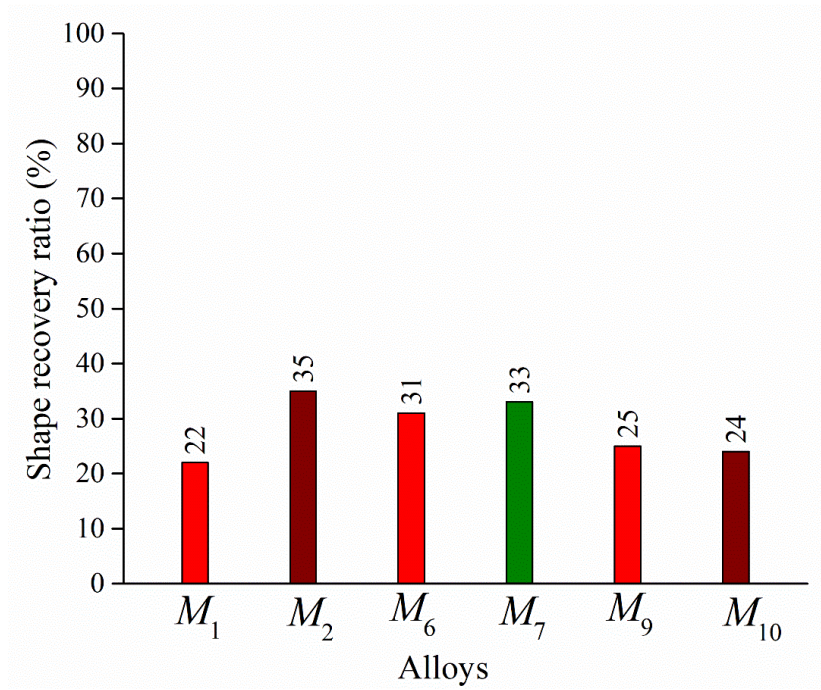


Figure 4.37 Shape recovery ratio of Cu-Al-Be-Mn Alloys

4.7 Cu-Al-Be-Zr

Based on the literature survey, alloying zirconium exhibits the lowest grain growth exponent (Gil et al. 1999) and performs significant grain refinement. This section presents the effect of alloying of zirconium, i.e., 0.1 - 0.4 wt.% to eutectoid and hypereutectoid Cu-Al-Be SMAs and its effect on microstructure, phases, transformation temperatures, and shape recovery ratios are presented with detailed mechanisms. The elemental compositions and their designations are tabulated in Table 4.14, and the alloys are designated as “Z_X,” ‘Z’ represents the type of alloy, ‘X’ represents the wt.% of manganese. X = 1, 2, 3, 4, and 5 for 0.05, 0.1, 0.2, 0.3 and 0.4 wt.% of Mn, respectively.

Table 4.14 Elemental composition and designations of Cu-Al-Be-Zr SMAs.

S. No.	Alloy	Actual composition (wt.%)			Zr (wt.%)
		Cu	Al	Be	
1.	T ₅	87.58	12.00	0.42	0.00
2.	Z ₁	87.50	12.00	0.42	0.08
3.	Z ₂	87.43	12.00	0.42	0.15
4.	Z ₃	87.47	11.90	0.43	0.20
5.	Z ₄	87.28	12.00	0.42	0.30
6.	Z ₅	87.18	12.00	0.42	0.40

4.7.1 XRD – phases

Figure 4.37 depicts the X-Ray diffractograms of Cu-Al-Be-Zr SMAs and unveils the phases that exist in the alloys. It is discerned from the diffractograms that, Zr-free alloy, i.e., Z₀ possess shear martensite of β'_1 (Cu₃Al) with little γ'_1 (CuAl) phase of orthorhombic (18R) and monoclinic (2H) structures, respectively, and confirmed from Figure 4.39a. The alloys, Z₁ to Z₅, exhibits the peaks of ZrAl₃ corresponds to very fine Al-rich spherical precipitates (Figure 4.40 a and d) attributed to a strong chemical affinity of Al to Zr (Bhattacharya et al. 1993a) and as Zr increases, the volume fraction of precipitates increases. It is also observed that, increase in addition of Zr above the solid solubility limit, i.e., greater than 0.1 wt% to the matrix, exhibited the presence of Cu₅Zr and AlCu₂Zr phases. The Cu₅Zr corresponds to the uniform distribution of

nanosized precipitates in the matrix (Bi et al. 2013; Pan et al. 2015; Peng et al. 2015), and AlCu_2Zr corresponds to the zirconium enriched precipitates at the grain boundaries (Figure 4.39 and Figure 4.40) are due to the diffusion of excess Zr towards grain boundaries (Gustmann et al. 2017) at elevated temperatures (betatization) and retained after quenching. The Z_4 and Z_5 exhibit the presence of ZrO_2 (Figure 4.40 f and g) because the diffused Zr at the grain boundaries has a higher affinity towards O_2 (Matsuoka et al. 1983) at elevated temperatures. The phases of β'_1 , γ'_1 , ZrAl_3 , Cu_5Zr , Cu_2AlZr , and ZrO_2 were confirmed and indexed from ICDD 00-028-0005, 03-065-2750, 03-065-2250, 03-065-5906 and 03-065-2357 datasheets, respectively. Further, it is noticed that the prime diffraction peaks from the diffractograms, as shown in Figure 4.38, are (1 2 10) and (0 0 22) belonging to the martensite phase. The Intensity of the peak decreases with the broadening of width (Full Width Half Maximum) is an indicator of refinement in the crystallite size up to Z_4 .

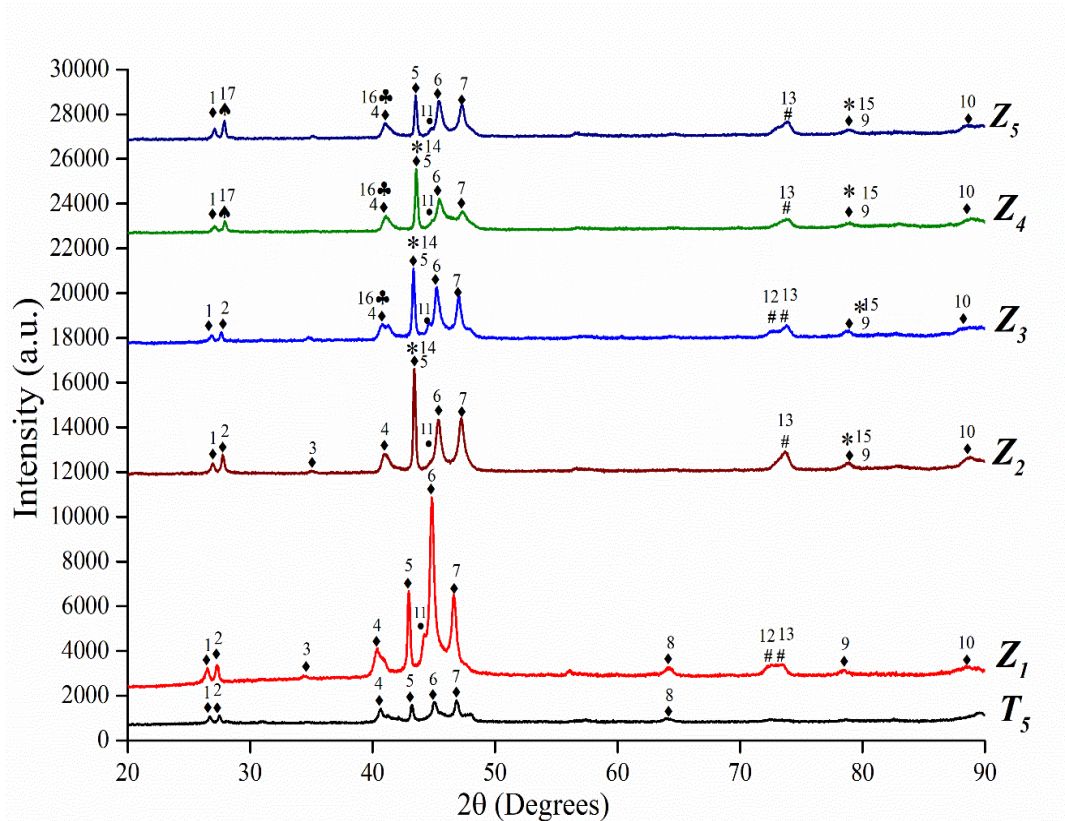
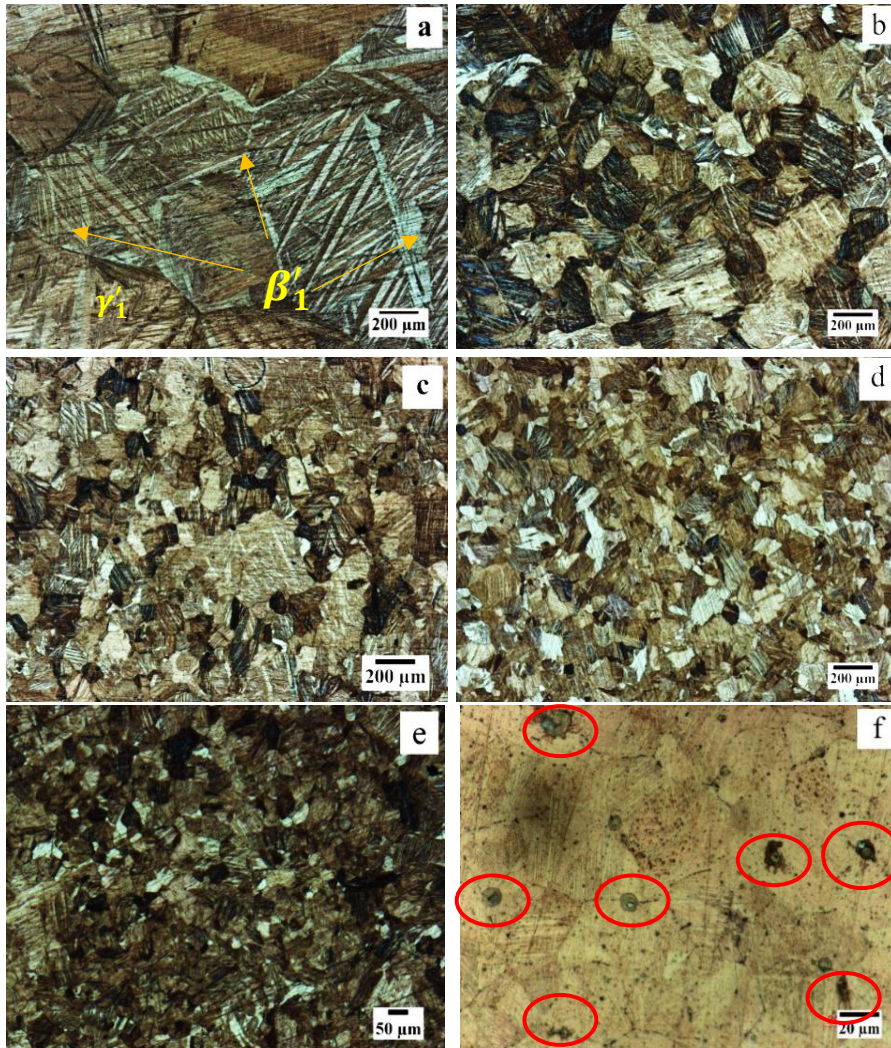


Figure 4.38 X-ray diffractograms of Cu-Al-Be-Zr SMAs.

4.7.2 Microstructure and morphology

Microstructures of the alloys, as depicted in Figure 4.39, exhibits grains were completely recrystallized and refined with the addition of Zr.



50 \times - (a) T_5 , (b) Z_1 , (c) Z_2 , (d) Z_3 , (e) Z_4 and (f) Z_5 - 500 \times

Figure 4.39 Microstructures of Cu-Al-Be-Zr SMAs

It is observed from Figure 4.39a, Z_0 (Zr free) has coarse grains of size $463.45 \pm 10 \mu\text{m}$, with zig-zag martensite ($18R - \beta'_1$) in the form of long spears and a small amount of coarse variants ($2H - \gamma'_1$). Addition of Zr to Z_1 and Z_2 , i.e., 0.05 and 0.1 wt.% to the matrix, exhibit bimodal grains (irregular in sizes), as shown in Figure 4.39b and c have a grain size of 157.07 and 125.97 μm , respectively. The variations in the grain size of the alloys are due to the irregular distribution of refiner in the matrix, because of

minimal addition. An increase in Zr to Z₃ and Z₄, i.e., 0.2 and 0.3 wt.%, produces equiaxial grains in lateral and longitudinal directions, as shown in Figure 4.39d and e, with an average size of 116.49 and 50.13 μm , respectively. An increase in Zr to Z₅ again increases the grain size to 159.02 μm . The percentage of reduction in grain sizes were 0, 66.10, 72.81, 74.86, 89.18, and 65.68% for T₅, Z₁, Z₂, Z₃, Z₄, and Z₅, respectively.

It is manifested that the increase in doping of Zr reduces the grain size up to Z₄ as shown in Figure 4.39a-e, ascribed to various mechanisms, i.e.

- i) very low grain growth exponent of Zr (Gil et al. 1999),
- ii) uniform dispersion of Zr in the matrix acts as nucleant, i.e., Zr is insoluble in the matrix when quenched to room temperature creates heterogeneous nucleation sites (Sampath 2005; Yang et al. 2016a) and enhances the number of grains and
- iii) surplus Zr above the solid solubility limit forms fine spherical precipitates in the grains (Sampath and Mallik 2009a) and precipitates at the grain boundaries inhibits the grain growth.

It is worth noting that the width and thickness of the martensite plates decrease with the decrease in grain size, with the increase of Zr. The orientation of grains and martensite variants are completely irregular due to rapid quenching from the elevated temperature. An increase in grain size of Z₅ is due to the surplus addition of Zr. It is highly insoluble in the matrix and agglomerates at the grain boundary, as shown in the red colored ellipses of Figure 4.39f and also in Figure 4.40a causes no refinement.

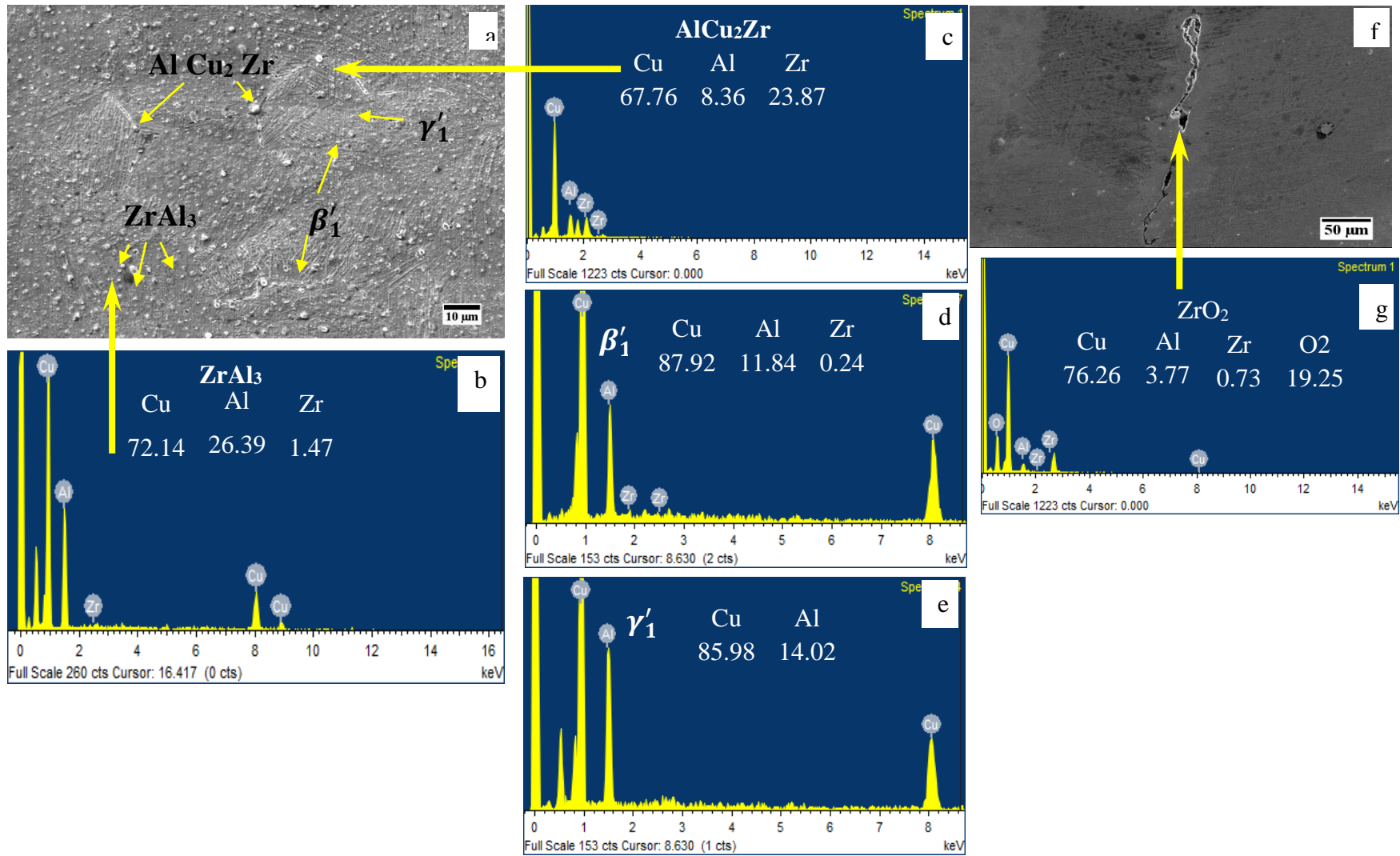


Figure 4.40 SEM images of Cu-Al-Be-Zr SMAs. (a) Z4 and (f) Z5, and EDS; (b) ZrAl_3 , (c) AlCu_2Zr (d) β'_1 , (e) γ'_1 , and (g) ZrO_2 .

4.7.3 Phase transformation temperatures

The thermoelastic martensitic transformation temperatures of the alloys are as depicted in Figure 4.41, and are tabulated in Table 4.15. It is perceived from thermograms, the addition of Zr didn't exhibit a rapid change in the transformation temperatures up to Z_2 , and similar behavior is reported in (Sampath and Mallik 2009a). Further, the addition of Zr shifts (inclined curves) towards higher temperatures (Sampath 2005) attributes to the distribution of fine second phase particles/intermetallics (precipitates), i.e., $ZrAl_3$, Cu_2AlZr , and Cu_5Zr in the matrix require an additional amount of energy for the phase transformation.

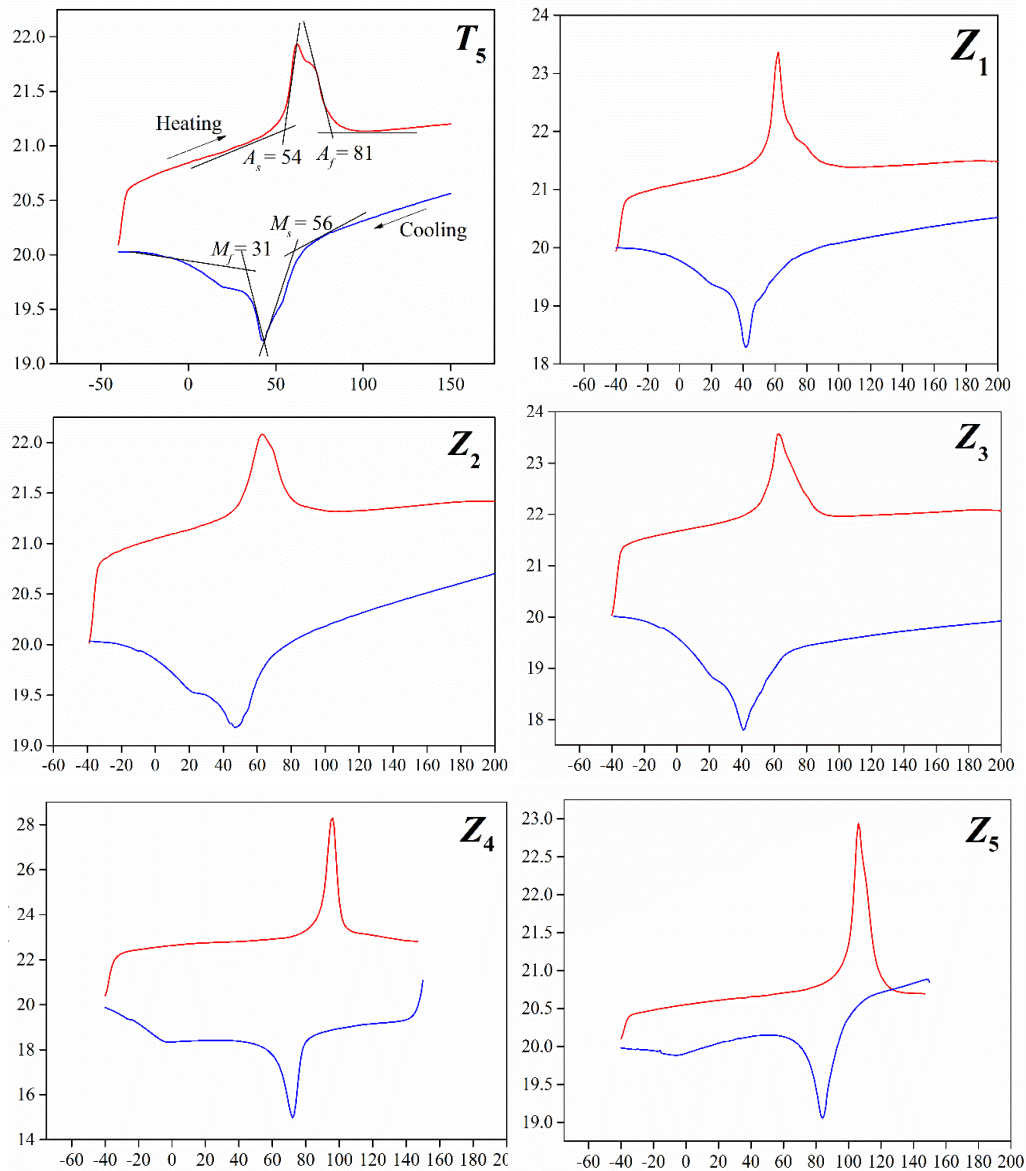


Figure 4.41 Thermograms of Cu-Al-Be-Zr SMAs.

It is also observed that the increase/decrease in M_f , M_s , enthalpies, and hysteresis are due to the size, vol. fraction and types of precipitates with variations in their elemental composition (Flores Zuniga et al. 1991), leads to difficulties in design and developing an actuator for the requisite temperature.

Table 4.15 Transformation temperatures, enthalpies, and hysteresis of Cu-Al-Be-Zr SMAs.

S. No	Alloy	M_f (°C)	M_s (°C)	$\Delta H_{A \rightarrow M}$ (J/g)	A_s (°C)	A_f (°C)	$\Delta H_{M \rightarrow A}$ (J/g)	Hysteresis (°C)
1.	Z_0	31	56	-14.8275	54	81	+9.7952	25
2.	Z_1	32	50	-11.7067	55	68	+6.9593	18
3.	Z_2	24	65	-14.3462	49	79	+7.8134	14
4.	Z_3	25	54	-14.3391	56	78	+8.2263	24
5.	Z_4	62	78	-6.5872	89	101	+6.5345	23
6.	Z_5	73	92.5	-6.4610	101	115	+8.1282	23

4.7.4 Shape recovery ratio

The shape recovery ratio of alloys was measured, and the results are plotted in Figure 4.42. From the results, it is observed that alloys $T_5 - Z_3$, exhibit excellent shape recovery ratio of 100%, due to the larger grains has less grain boundary area, which is easy to recover. The reduction in recovery was observed from Z_4 due to increasing Zr above solid solubility at room temperature forms:

- i) various sizes of precipitates (Figure 4.39 and Figure 4.40) with increase/decrease in the elemental composition compared with the matrix alters the transformation temperatures entirely (Otsuka and Wayman 1999),
- ii) rapid quenching from high temperatures (850 °C) creates more quenched-in vacancies in the fine grains leads to stabilization (Chandrasekaran et al. 1995),
- iii) finer the grains will possess different orientation of grains, and martensite variants which act as a grain constraint and irregular grain boundaries create confusion path to revert back (Sure and Brown 1984) and

- iv) Precipitates at the grain boundary act as a barrier for thermoelastic martensite plate movement requires more energy to overcome the obstacles, supplying more energy tend to deteriorate the life of the actuator rapidly.

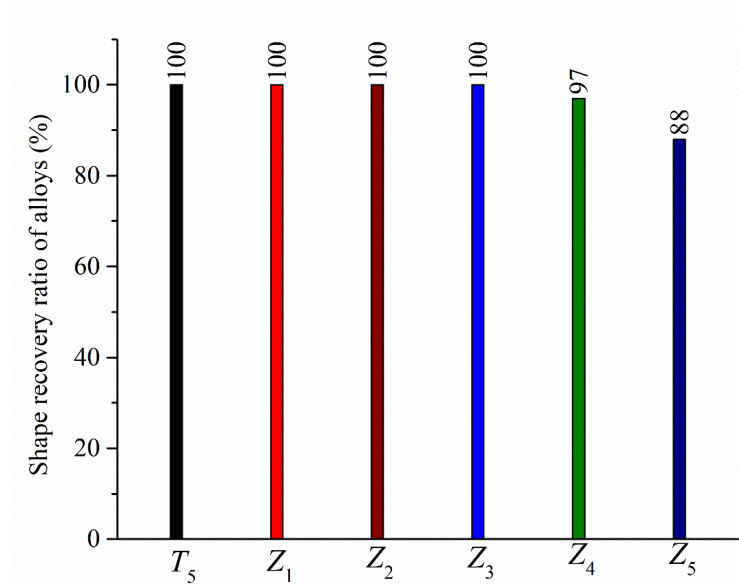


Figure 4.42 Shape recovery ratio of Cu-Al-Be-Zr SMAs.

4.7.5 Mechanical Properties

The addition of Zirconium refines the grains, as shown in Figure 4.39, and its influence on mechanical properties was measured by the unidirectional tensile tests. The measured engineering stress-strain data, i.e., ultimate tensile strength, ductility, yield stress (0.2% Proof stress), and yield strain of the alloys, are presented in Table 4.16, and also depicted in Figure 4.43.

Table 4.16 Mechanical Properties of Cu-Al-Be-Zr SMAs.

Alloy	Ultimate tensile strength (MPa)	Ductility (%)	Yield stress (0.2 %) (MPa)	Yield strain (0.2 %)
Z ₀	363 ± 35	10.80 ± 0.75	132.34 ± 8.40	1.60 ± 0.03
Z ₁	361 ± 15	13.20 ± 0.20	135.41 ± 22.61	1.71 ± 0.24
Z ₂	545 ± 20	18.14 ± 0.29	114.48 ± 21.10	1.16 ± 0.35
Z ₃	569 ± 05	21.90 ± 0.27	144.27 ± 5.79	1.62 ± 0.27
Z ₄	667 ± 30	23.95 ± 0.86	147.03 ± 10.73	1.96 ± 0.15
Z ₅	479 ± 13	10.59 ± 0.17	176.98 ± 13.23	1.70 ± 0.18

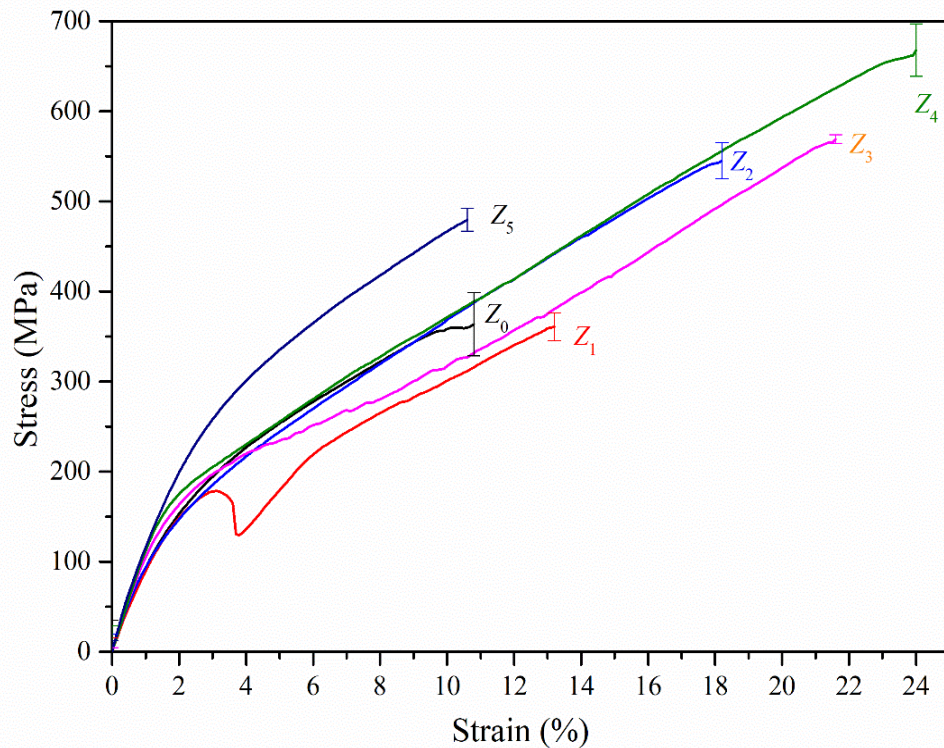
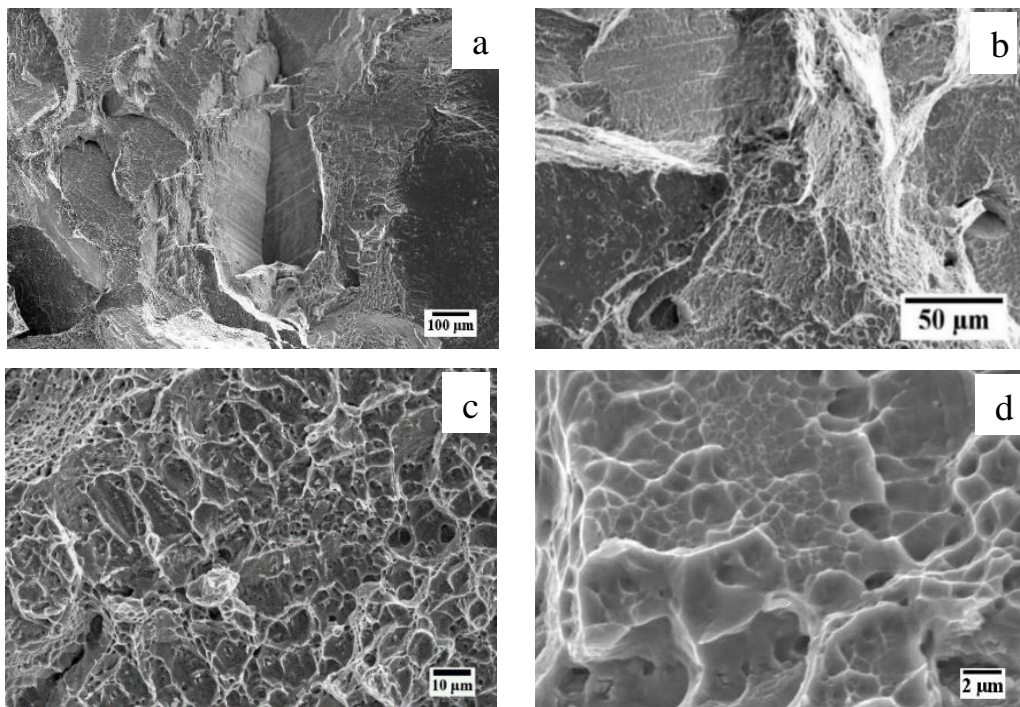
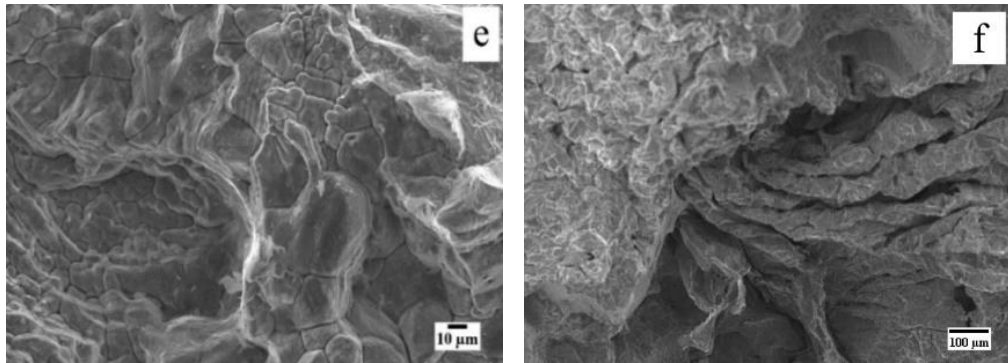


Figure 4.43 Stress-strain curves of Cu-Al-Be-Zr SMAs.

From the results, it is observed that T_5 (Zr-free) has an ultimate tensile strength of 363 ± 35 MPa with ductility of 10.80 ± 0.75 %, which fails in cleavage mode as shown in Figure 4.44a. As Zr increased to Z_1 , i.e., 0.05 wt% to the matrix, it is observed an improvement in the ductility to 13.20 ± 0.20 with almost the same tensile strength of T_5 , i.e., 361 ± 15 MPa. The stress-strain curve of Z_1 exhibit a kink (Figure 4.43) related to heterogeneous deformation, i.e., drop in the stress and then increases till fracture. Heterogeneous deformation attributed to distorted lattice arrangement and bimodal grains (variable sizes), as shown in Figure 4.39b and c, and confirms from the mixed-mode fracture surface, as shown in Figure 4.44b. Increase in Zr to Z_2 , Z_3 and Z_4 exhibit a significant increase in tensile strengths, 545 ± 20 , 569 ± 5 and 667 ± 30 MPa with enhanced ductility of 18.14 ± 0.29 , 21.90 ± 0.27 and 23.95 ± 0.86 respectively. The improvement in the properties are due to (a) finer the grain size, orientation of grains changes over small distances (Figure 4.39d and e) increases in the length of the grain boundary, takes more deviations for the propagation of crack and requires more energy to move the dislocations (Yang et al. 2016a). (b) Formation and distribution of fine precipitates of $ZrAl_3$, Cu_5Zr (Ye et al. 2014; Yi et al. 2015) in the grains, prevents the movement of dislocations, subsequently increases the magnitude of critical stress

for the deformation. It is worth to present, and highlight the factor affecting enhanced ductility of the alloys is Cu_5Zr phase, i.e., it has a higher resistance to uniaxial deformation (Yi et al. 2015). An increase in Zr increases the fine precipitates of Cu_5Zr in the alloy matrix, which confirms from X-ray diffractogram (Figure 4.38). The fractured surfaces, as shown in (Figure 4.44c – d), exhibit dimples (cavities) formed due to precipitates (Lee and Wayman 1986a) and enlarged with the increase in loading till fracture confirms the ductile fracture. Further, the increase in Zr to Zr_5 fails rapidly, with the fall in tensile strength and ductility to 479 MPa and 10.59 %, respectively, as shown in Figure 4.43. The failure attributes to hydrogen embrittlement (Figure 4.44e and f), viz. insoluble Zr segregated at grain boundaries entraps oxygen into the lattice due to the high affinity at elevated temperature forms voids while quenching. However, the hydrogen molecule diffuses rapidly through the voids because of its small atomic radii and reacts with the entrapped oxygen forms water vapor. These vapor molecules exert higher pressure that is too large to diffuse out of the metal and splits the bonding between the grains, forming hydrides at the grain boundaries known as hydride cracking (Schwartz 2003).





(a) T_5 , (b) Z_1 , (c) Z_2 , (d) Z_4 , and (e) and (f) Z_5

Figure 4.44 Fracture morphology of Cu-Al-Be-Zr

4.8 CLOSURE

This chapter reported the effect of ternary and quaternary elements on the phases, grain size, transformation temperatures, thermal hysteresis, shape recovery ratio, and mechanical properties of the alloys. Ternary Cu-Al-Be SMAs exhibit coarse grains of size $463.45 \pm 10 \mu\text{m}$, the maximum tensile strength of $363 \pm 35 \text{ MPa}$ and ductility of $10.80 \pm 0.75\%$. Ternary SMA T_5 exhibit complete recovery with $A_f - 81 \text{ }^\circ\text{C}$ and thermal hysteresis of $25 \text{ }^\circ\text{C}$. Alloying quaternary element boron of 0.15 wt.% to Cu-Al-Be SMA, i.e., B_{16} , refines the grain to $40.19 \pm 5 \mu\text{m}$ with an improved tensile strength of $580.67 \pm 12.67 \text{ MPa}$ and ductility of $24.98 \pm 0.32\%$. Alloying boron up to 0.08 wt.% increases the transformation temperatures and then decreases. B_{16} exhibit $A_f - 51 \text{ }^\circ\text{C}$ with a hysteresis of $28 \text{ }^\circ\text{C}$ and complete recovery. Alloying rare-earth elements, cerium, and gadolinium refine the grains to $25 \pm 10 \mu\text{m}$ and $81.80 \pm 10 \mu\text{m}$, respectively with minimal addition. Besides, the formation of Al-rich secondary phase particles deteriorates shape recovery, increases transformation temperatures, and thermal hysteresis of $29 \text{ }^\circ\text{C}$. Alloying manganese to Cu-Al-Be SMAs formed either coexistence of martensites or austenite and didn't exhibit complete recovery. Zirconium exhibits refinement of grain size to $50.13 \mu\text{m}$ with an improved tensile strength of $667 \pm 30 \text{ MPa}$ and ductility $23.95 \pm 0.86\%$. Increase in Zr increases transformation temperatures and exhibit $A_f - 101 \text{ }^\circ\text{C}$, thermal hysteresis of $23 \text{ }^\circ\text{C}$, reduction in recovery, and susceptible to hydrogen embrittlement/hydride cracking.

It is observed that boron and zirconium modified alloys exhibit improved strength, ductility, and shape recovery. Thermal hysteresis of both Cu-Al-Be-B and Cu-Al-Be-Zr SMAs are closer to the ternary SMA T_5 and didn't show much impact on narrowing. Besides, Cu-Al-Be-Zr SMAs are susceptible to hydrogen embrittlement/hydride cracking. Cu-Al-Be-B SMAs meets the requisites of SMAs for actuator applications and recommended.

CHAPTER 5

CONCLUSIONS & FUTURE SCOPE

5.1 CONCLUSIONS

In the present study, investigated the effect of ternary and quaternary elements and varying their elemental composition on the properties of SMAs. The key conclusions drawn from the study are:

- Aluminium plays a significant role in the modification of phases and martensite fraction, followed by beryllium.
- Hypoeutectoid Al SMAs didn't exhibit martensite transformation due to the mixture of $\alpha + \beta'_1$ phases and Al > 11.8 wt.% exhibit complete martensite β'_1 .
- Beryllium < 0.42 wt.% didn't exhibit complete martensite transformation and increase in Be > 0.44 forms coexistence of martensites $\beta'_1 + \gamma'_1$.
- Microalloying of boron effectively refines the grains, increases transformation temperatures, hysteresis, and exhibit complete recovery.
- Rare-earth elements cerium and gadolinium exhibit improved grain refinement with minimal addition.
- Increase in Ce forms γ_2 precipitates in the matrix and CeO₂ at grain boundaries forms microvoids lead to decohesion.
- An increase in Gd forms insoluble secondary phase precipitates at grain boundaries leads to decohesion.
- Manganese modifies the phases and forms coexistence of martensites $\beta'_1 + \gamma'_1$.and increase in Mn > 0.55 wt.% transforms to complete austenite β_1 .
- Zirconium exhibits good grain refinement and forms precipitates of secondary phases. An increase in Zr increases transformation temperatures, tensile strength, and ductility.
- Excessive Zr leads to hydrogen embrittlement/hydride cracking.

5.2 SCOPE FOR FURTHER RESEARCH

The effect of alloying ternary and quaternary elements and varying their elemental composition on properties has been investigated in the present study and determined the suitable alloying element and its optimal composition. The following are recommended for future research work.

- Investigation on the properties of SMAs quenching in different mediums.
- Investigation on drawing SMA wires for actuator applications from the optimal combination SMA.
- Investigation on functional fatigue of the SMA wire by maintaining constant loads and strains.
- Investigation on vibration characteristics of the shape memory alloy embedded composite structures.

References

- A.P. Prevarskii, and Kuzma, Y. B. (1988). "X-Ray Structural Investigation of the System Gd-Cu-Al." *Russ. Metall.*, 1, 205–207.
- Adnyana, D. N. (1986). "Effect of grain size on transformation temperatures in a grain-refined, copper-based, shape-memory Alloy." *Metallography*, 18(1985), 187–196.
- Agafonov, V., Naudot, P., Dubertret, A., and Dubois, B. (1988). "INFLUENCE OF THE ALUMINIUM CONTENT ON THE APPEARANCE AND STABILITY OF MARTENSITES IN THE Cu - Al - Ni SYSTEM." *Scr. Metall.*, 22, 489–494.
- Akash, K., Mani Prabu, S. S., Gustmann, T., Jayachandran, S., Pauly, S., and Palani, I. A. (2018). "Enhancing the life cycle behaviour of Cu-Al-Ni shape memory alloy bimorph by Mn addition." *Mater. Lett.*, 226, 55–58.
- Aksu Canbay, C., Karagoz, Z., and Yakuphanoglu, F. (2014). "Controlling of transformation temperatures of Cu-Al-Mn shape memory alloys by chemical composition." *Acta Phys. Pol. A*, 125(5), 1163–1166.
- Aksu Canbay, C., and Keskin, A. (2014). "Effects of vanadium and cadmium on transformation temperatures of Cu-Al-Mn shape memory alloy." *J. Therm. Anal. Calorim.*, 118(3), 1407–1412.
- Albuquerque, V. H. C. de, Melo, T. A. de A., Gomes, R. M., Lima, S. J. G. de, and Tavares, J. M. R. S. (2010a). "Grain size and temperature influence on the toughness of a CuAlBe shape memory alloy." *Mater. Sci. Eng. A*, 528(1), 459–466.
- Albuquerque, V. H. C. de, Melo, T. A. de A., Oliveira, D. F. de, Gomes, R. M., and Tavares, J. M. R. S. (2010b). "Evaluation of grain refiners influence on the mechanical properties in a CuAlBe shape memory alloy by ultrasonic and mechanical tensile testing." *Mater. Des.*, 31(7), 3275–3281.
- Atli, K. C., Karaman, I., Noebe, R. D., Garg, A., Chumlyakov, Y. I., and Kireeva, I. V. (2010). "Improvement in the Shape Memory Response of Ti50.5Ni24.5Pd25 High-Temperature Shape Memory Alloy with Scandium Microalloying." *Metall. Mater. Trans. A*, 41(10), 2485–2497.

- Baker, H., and Okamoto, H. (1992). *ASM Handbook. Vol. 3. Alloy Phase Diagrams*. ASM International, Materials Park, Ohio 44073-0002, USA, 1992. 501.
- Balart, M. J., Patel, J. B., Gao, F., and Fan, Z. (2016). “Grain Refinement of Deoxidized Copper.” *Metall. Mater. Trans. A Phys. Metall. Mater. Sci.*, 47(10), 4988–5011.
- Balo, S. N., and Ceylan, M. (2002). “Effect of Be content on some characteristics of Cu – Al – Be shape memory alloys.” *J. Mater. Process. Technol.*, 124, 200–208.
- Belkahla, S., Flores Zuniga, H., and Guenin, G. (1993). “Elaboration and characterization of new low temperature shape memory CuAlBe alloys.” *Mater. Sci. Eng. A*, 169(1–2), 119–124.
- Belkahla, S., and Guenin, G. (1991). “Martensitic Transformation and Metallurgical Study of Low Temperature Cu-Al- Be Ternary alloy.” *J. Phys. IV*, 1(C4), C4-145.
- Bhattacharya, S., Bhuniya, A., and Banerjee, M. K. (1993a). “Influence of minor additions on characteristics of Cu-AI-Ni alloy.” *Mater. Sci. Technol.*, 9(August), 654–658.
- Bhattacharya, S., Bhuniya, A., and Banerjee, M. K. (1993b). “Influence of minor additions on characteristics of Cu-AI-Ni alloy.” *Mater. Sci. Technol.*, 9(August), 654–658.
- Bi, L. M., Liu, P., Chen, X. H., Liu, X. K., Li, W., and Ma, F. C. (2013). “Analysis of phase in Cu-15%Cr-0.24%Zr alloy.” *Trans. Nonferrous Met. Soc. China (English Ed.)*, 23(5), 1342–1348.
- Bigelow, G. S., Padula, S. A., Garg, A., Gaydos, D., and Noebe, R. D. (2010). “Characterization of ternary NiTiPd high-temperature shape-memory alloys under load-biased thermal cycling.” *Metall. Mater. Trans. A Phys. Metall. Mater. Sci.*, 41(12), 3065–3079.
- Birol, Y. (2012). “Grain refinement of Al–Cu foundry alloys with B additions.” *Int. J. Cast Met. Res.*, 25(2), 117–120.
- Blazquez, M. L., Castillo, C. L. D. E. L., and Gomez, C. (1989). “Influence of the Composition and Maximum Cycling Temperature on the Microstructure of Cu-AI-Mn

Shape Memory Alloys The alloys chosen for this work were produced by induction melting.” *Metallography*, 23, 119–133.

Bohong, J., and Hsu, T. Y. (1991). “Influence of Order, Grain Size and Pre-Strain on Shape Memory Effect in Cu-Zn-Al Alloys.” *Mater. Sci. Forum*, 457–461.

Bublei, I. R., and Titov, P. V. (1990). “Effect of Aluminium and Manganese on the Martensitic Transformation Characteristics in alloys of the system Cu-Al-Mn.” (4), 288–290.

Buehler, W. J., and Wiley, R. C. (1961). “THE PROPERTIES OF TiNi AND ASSOCIATED PHASES.” *NOLTR Rep. (AD 266607)*, 61–75.

Bujoreanu, L. G., Lohan, N. M., Pricop, B., and Cimpoes, N. (2011). “Thermal Memory Degradation in a Cu-Zn-Al Shape Memory Alloy During Thermal Cycling with Free Air Cooling.” *J. Mater. Eng. Perform.*, 20(April), 468–475.

Burkart, M. W., and Read, T. A. (1953). “Diffusionless Phase Change in the Indiumthallium System.” *Transactions Am. Inst. Min. Metall. Eng.*, 197(11), 1516–1524.

Canbay, C. A., and Karagoz, Z. (2013). “Effects of Annealing Temperature on Thermomechanical Properties of Cu-Al-Ni Shape Memory Alloys.” *Int. J. Thermophys.*, 34(7), 1325–1335.

Candido, G. V. D. M., Melo, T. A. D. A., Albuquerque, V. H. C. De, Gomes, R. M., Lima, S. J. G. De, and Tavares, J. M. R. S. (2012). “Characterization of a CuAlBe alloy with different Cr contents.” *J. Mater. Eng. Perform.*, 21(11), 2398–2406.

Chandrasekaran, M., Cesari, E., Wolska, J., Hurtado, I., Stalmans, R., and Dutkiewicz, J. (1995). “Stabilisation of Martensite in Copper Based Shape Memory Alloys.” *J. Phys. IV*, 5(C2), 143–152.

Chang, L.-C., and Read, T. A. (1951). “Plastic deformation and diffusionless changes in metals. The gold-cadmium beta phase.” *Trans. AIME*, 191(January), 47–52.

Chen, Z., Kang, H., Fan, G., Li, J., Lu, Y., Jie, J., Zhang, Y., Li, T., Jian, X., and Wang, T. (2016). “Grain refinement of hypoeutectic Al-Si alloys with B.” *Acta Mater.*,

120(January 2018), 168–178.

Chentouf, S. M., Bouabdallah, M., Patoor, E., and Sari, A. (2009). “Microstructural and thermodynamic study of hypoeutectoidal Cu – Al – Ni shape memory alloys.” *J. Alloys Compd.*, 470, 507–514.

Cook, J. M., and Brown, L. M. (1978). “VARIATION OF MARTENSITIC TRANSFORMATION TEMPERATURES AFTER LOW TEMPERATURE AGEING IN A QUENCHED Cu-Zn-AL ALLOY.” *Scr. Metall.*, 12, 949–952.

Dasgupta, R., Jain, A. K., Hussain, S., Pandey, A., and Sampath, V. (2018). “Effect of Alloying Additions on the Properties Affecting Shape Memory Properties of Cu–12.5Al–5Mn Alloy.” *Front. Mater. Process. Appl. Res. Technol.*, 377–390.

Dasgupta, R., Jain, A. K., Kumar, P., Hussain, S., and Pandey, A. (2015). “Role of alloying additions on the properties of Cu-Al-Mn shape memory alloys.” *J. Alloys Compd.*, 620, 60–66.

Davis, J. R., and Committee, A. S. M. I. H. (2001). *Copper and Copper Alloys*. ASM specialty handbook, ASM International.

DELAEY, L., SUZUKI, T., and HUMBEECK, J. VAN. (1984). “THE STABILISATION OF STEP-QUENCHED COPPER-ZINC-ALUMINIUM MARTENSITE PART II: CRYSTAL STRUCTURE AND REORDERING.” *Scr. Metall.*, 18, 899–903.

Dhanalakshmi, K., Umopathy, M., and Ezhilarasi, D. (2014). “Shape memory alloy actuated structural control with discrete time sliding mode control using multirate output feedback.” *J. Vib. Control*, (April), 1–20.

Dong, Y. Y., Wang, C. M., Gu, Y. P., and Liu, Y. G. (2002). “Phenomena of Aluminum Segregation at the Grain Boundaries of CuAlBe-X Alloys.” *Mater. Sci. Forum*, 394–395, 209–212.

Dong, Y. Y., Wang, T. M., Zin, S. J., and Dar, K. Z. (1994). “The shape memory capability and life of Cu-Al-Be-X alloys.” *Mater. Charact.*, 33(2), 163–168.

Dongi, F., Dinkier, D., Kroplin, B., Model, M., Forum, A. S., and Orleans, N. (1996).

- “Active Panel Flutter Suppression Using Self-Sensing Piezoactuators.” *Am. Inst. Aeronaut. Astronaut.*, 34(6), 1224–1230.
- Duerig, T. W., Melton, K. N., and Stöckel, D. (2013). *Engineering Aspects of Shape Memory Alloys*. Elsevier Science.
- Duisemaliev, U., and Presnyakov, A. (1964). “Solubility of cerium in copper and physico-mechanical properties of copper-cerium alloys.” *Zhur. Neorg. Khim.*, 9, 2258–2260.
- Dunne, D., Ireland, K., Gonzalez, C., Morin, M., and Guenin, G. (2006). “Hyperstabilisation of martensite in Cu-Al-Be alloys.” *Mater. Sci. Eng. A*, 438–440, 339–342.
- Duschanek, H., and Rogl, P. (1994). “The Al-B (Aluminum-Boron) System.” *J. Phase Equilibria*, 15(5), 543–552.
- Emadi, P. (2014). “Grain refinement of magnesium and AZ91E magnesium alloy by addition of MgB₂ inoculant.” Ryerson University.
- Epps, J., and Chandra, R. (1997). “Shape memory alloy actuation for active tuning of composite beams *.” *Smart Mater. Struct.*, 6, 251–264.
- Ergen, S., Uzun, O., Yilmaz, F., and Kiliçaslan, M. F. (2013). “Shape memory properties and microstructural evolution of rapidly solidified CuAlBe alloys.” *Mater. Charact.*, 80, 92–97.
- Fazelzadeh, S. A., and Jafari, S. M. (2008). “Active control law design for flutter suppression and gust alleviation of a panel with piezoelectric actuators.” *Smart Mater. Struct.*, 035013(17), 1–9.
- Flores Zuniga, H., Belkahla, S., and Guénin, G. (1991). “The Thermal Aging and Two way Memory Effect (TWME) IN Cu-Al-Be Shape Memory Alloy.” *J. Phys. III*, 1(C4), 289–294.
- Garafolo, N. G., and Mchugh, G. R. (2018). “Mitigation of flutter vibration using embedded shape memory alloys.” *J. Fluids Struct.*, 76, 592–605.
- Gil, F. J., Guilemany, J. M., and Sanchiz, I. (1993). “Grain growth in Cu-Zn-Al-Mn

shape-memory alloy.” *J. Mater. Sci.*, 28(6), 1542–1544.

Gil, F. J., Pena, J., and Guillemany, J. M. (1999). “Improvement of the Grain Refinement of Cu-Zn-Al Shape Memory Alloys with Manganese , Cobalt , and Zirconium Addition.” *J. Mater. Synth. Process.*, 7(2), 127–133.

Greninger, A. B. (1939). “The martensite transformation in beta copper-aluminium alloys.” *AIME Trans*, 133, 204–227.

Guilemany, J. M., and Gil, F. J. (1990). “THE RELATIONSHIP BETWEEN CHEMICAL COMPOSITION AND TRANSFORMATION TEMPERATURES, M_s AND A_s IN POLYCRYSTALS AND SINGLE CRYSTALS OF Cu-Zn-Al SHAPE-MEMORY ALLOYS.” *Thermochim. Acta*, 167, 129–138.

Guilemany, J. M., and Gil, F. J. (1991). “Kinetic grain growth in Cu-Zn-Al shape memory alloys.” *J. Mater. Sci.*, 26, 4626–4630.

Guniputi, B. N., and Murigendrappa, S. M. (2018). “Influence of Gd on the microstructure, mechanical and shape memory properties of Cu-Al-Be polycrystalline shape memory alloy.” *Mater. Sci. Eng. A*, 737(September), 245–252.

Gustmann, T., Santos, J. M. dos, Gargarella, P., Kühn, U., Humbeeck, J. Van, and Pauly, S. (2017). “Properties of Cu-Based Shape-Memory Alloys Prepared by Selective Laser Melting.” *Shape Mem. Superelasticity*, 3(1), 24–36.

Haidar, M. A., Saud, S. N., and Hamzah, E. (2018). “Microstructure , Mechanical Properties , and Shape Memory Effect of Annealed Cu-Al-Ni-xCo Shape Memory Alloys.” *Metallogr. Microstruct. Anal.*, 7(1), 57–64.

Higuchi, A., Suzuki, K., Matsumoto, Y., Sugimoto, K., Komatsu, S., and Nakamura, Y. (1982). “Shape Memory Effect in Cu-Al-Be Ternary alloys.” *J. Phys. Colloq.*, 43(C4), C4-767.

Hong, H. U., Jeong, H. W., Kim, I. S., Choi, B. G., Yoo, Y. S., and Jo, C. Y. (2012). “Significant decrease in interfacial energy of grain boundary through serrated grain boundary transition.” *Philos. Mag.*, 6435.

Horace, P., and Norman, R. (1970). “Influence of Aluminum on the Martensitic

- Transformation of Beta Phase CuZn Alloys.” *Metall. Transactions*, I(9), 2653–2655.
- Hsu, C. A., Wang, W. H., Hsu, Y. F., and Rehbach, W. P. (2009). “The refinement treatment of martensite in Cu–11.38wt.%Al–0.43wt.%Be shape memory alloys.” *J. Alloys Compd.*, 474, 455–462.
- Hsu, C., and Wang, W. (1996). “Superplastic forming characteristics of a Cu-Zn-Al-Zr memory alloy.” 205, 247–253.
- Huang, W. (2002). “On the selection of shape memory alloys for actuators.” *Mater. Des.*, 23(1), 11–19.
- HuaPing, X., Gaofeng, S., and Xiemin, M. (2011). “A Study on Shape Memory Performance of Cu-Al-Ni-Be Alloy Single Crystal.” *Adv. Mater. Res.*, 287–290, 21–25.
- Humbecck, J. Van, D, V. H., L, D., Ortin, J., C, S., and V, T. (1987). “A Two-Stage Martensite Transformation in a Cu-13 . 99 mass % Al-3 . 5 mass % Ni Alloy.” *Trans. Japan Inst. Met.*, 28(5), 383–391.
- Hussain, S., Pandey, A., and Dasgupta, R. (2019). “Designed polycrystalline ultra-high ductile boron doped Cu–Al–Ni based shape memory alloy.” *Mater. Lett.*, 240, 157–160.
- Hussein, A. A. (1982). “Structure-Property Relationships in Dual-Phase Cu-Al Alloys: Part I. Individual Phases.” *Metall. Trans. A*, 13(5), 837–846.
- J.H.Yang, C.S.Zhang, Zhao, L. C., and T.C.Lei. (1987). “VARIATIONS OF MARTENSITE CRYSTAL STRUCTURE AND MORPHOLOGY IN A Cu-Al-Zn-Mn-Ni ALLOY.” *Scr. Metall.*, 21(c), 259–264.
- Jain, A. K., Hussain, S., Kumar, P., Pandey, A., and Rupa, D. (2016). “Effect of Varying Al / Mn Ratio on Phase Transformation in Cu – Al – Mn Shape Memory Alloys.” *Trans. Indian Inst. Met.*, 69(6), 1289–1295.
- Jiao, Y. Q., Wen, Y. H., Li, N., He, J. Q., and Teng, J. (2010). “Effect of solution treatment on damping capacity and shape memory effect of a CuAlMn alloy.” *J. Alloys Compd.*, 491(1–2), 627–630.

- K.A. Gschneidner, J. and, and Calderwood, F. W. (1988). “The Al-Ce (Aluminum-Cerium) System.” *Bull. Alloy Phase Diagrams*, 9(6), 669–672.
- Kainuma, R., Takahashi, S., and Ishida, K. (1996). “Thermoelastic Martensite and Shape Memory Effect in Ductile Cu-Al-Mn Alloys.” *Metall. Mater. Trans. A*, 27A, 2187–2195.
- Kandagal, S. B., and Venkatraman, K. (2006). “Piezo-actuated Vibration and Flutter Control.” *Def. Sci. J.*, 56(4), 615–626.
- Karaca, H. E., Acar, E., Ded, G. S., Basaran, B., Tobe, H., Noebe, R. D., Bigelow, G., and Chumlyakov, Y. I. (2013). “Shape memory behavior of high strength NiTiHfPd polycrystalline alloys.” *Acta Mater.*, 61(13), 5036–5049.
- Karagoz, Z., and Canbay, C. A. (2013). “Relationship between transformation temperatures and alloying elements in Cu-Al-Ni shape memory alloys.” *J. Therm. Anal. Calorim.*, 114(3), 1069–1074.
- Kim, J. W., Roh, D. W., Lee, E. S., and Kim, Y. G. (1990). “Effects on Microstructure and Tensile Properties of a Zirconium Addition to a Cu-Al-Ni Shape Memory Alloy.” *Metall. Trans. A*, 21A(March), 741–744.
- Koeda, N., Omori, T., Sutou, Y., Suzuki, H., Wakita, M., Kainuma, R., and Ishida, K. (2005). “Damping Properties of Ductile Cu-Al-Mn-Based Shape Memory Alloys.” 46(1), 198–201.
- Koster, W., and Godecke, T. (1966). “No Title.” *Z. Met.*, 57, 889.
- Koul, A. K., and Thamburaj, R. (1985). “Serrated Grain Boundary Formation Potential of Ni-Based Superalloys and Its Implications.” *Metall. Trans. A*, 16(January), 17–26.
- Kurdyumov, GV and Khandros, L. (1949). “ON THE ‘THERMOELASTIC’ EQUILIBRIUM ON MARTENSITIC TRANSFORMATIONS.” *Dokl. Akad. Nauk SSSR*, 66(2), 211–214.
- Kustov, S., Pons, J., Cesari, E., Humbeeck, J. Van, and Morin, M. (2004a). “Stabilization and hyperstabilization of Cu-Al-Be martensite by thermal treatment and plastic deformation.” *Mater. Sci. Eng. A*, 378, 283–288.

- Kustov, S., Pons, J., Cesari, E., Morin, M., and Humbeeck, J. Van. (2004b). "Athermal stabilization of Cu-Al-Be martensite due to plastic deformation and heat treatment." *Mater. Sci. Eng. A*, 373, 328–338.
- Lai, M. O., Lu, L., and Lee, W. H. (1996). "Influence of heat treatment on properties of copper-based shape-memory alloy." 31, 1537–1543.
- Lee, J. S., and Wayman, C. M. (1986a). "Grain Refinement of Cu-Zn-Al Shape Memory Alloys." *Metallography*, 19, 401–419.
- Lee, J. S., and Wayman, C. M. (1986b). "Grain Refinement of a Cu–Al–Ni Shape Memory Alloy by Ti and Zr Additions." *Trans. Japan Inst. Met.*, 27(8), 584–591.
- Lexcellent, C. (2013). *Shape-memory alloys handbook*. John Wiley & Sons.
- Li, J., and Ansell, G. S. (1983). "The Effect of Thermal Cycling on the Thermoelastic Martensitic Transformation in a Cu-Zn-Al Alloy." *Metall. Trans. A*, 14A, 1293–1297.
- Liu, A. L., Gao, Z. Y., Gao, L., Cai, W., and Wu, Y. (2007a). "Effect of Dy addition on the microstructure and martensitic transformation of a Ni-rich TiNi shape memory alloy." *J. Alloys Compd.*, 437(1–2), 339–343.
- Liu, A. L., Sui, J. H., Lei, Y. C., Cai, W., Gao, Z. Y., and Zhao, L. C. (2007b). "Effect of y addition on microstructure and martensitic transformation of a Ni-rich Ti-Ni shape memory alloy." *J. Mater. Sci.*, 42(14), 5791–5794.
- Lojen, G., Anžel, I., Kneissl, A., Križman, A., Unterweger, E., Kosec, B., and Bizjak, M. (2005). "Microstructure of rapidly solidified Cu-Al-Ni shape memory alloy ribbons." *J. Mater. Process. Technol.*, 162–163(SPEC. ISS.), 220–229.
- Lopez Del Castillo, C., Heranez, J., and Mellor, B. G. (1986). "The effect of thermal and stress cycling on thermoelastic martensite formation in Cu - Al - Mn alloys." *J. Mater. Sci.*, 21, 4043–4047.
- Lopez del Castillo, C., Mellor, B. G., Blazquez, M. ., and Gomez, C. (1987). "The Influence of Composition and Grain Size on the Martensitic Transformation Temperatures of Cu-Al-Mn Shape Memory Alloys." *Scr. Metall.*, 21, 1711–1716.
- Lozovoi, A. Y., and Paxton, A. T. (2008). "Boron in copper: A perfect misfit in the

bulk and cohesion enhancer at a grain boundary.” *Phys. Rev. B - Condens. Matter Mater. Phys.*, 77(16), 1–16.

Lu, X., Chen, F., Li, W., and Zheng, Y. (2009). “Effect of Ce addition on the microstructure and damping properties of Cu – Al – Mn shape memory alloys.” *J. Alloys Compd.*, 480, 608–611.

Mallik, U. S., and Sampath, V. (2009). “Influence of quaternary alloying additions on transformation temperatures and shape memory properties of Cu-Al-Mn shape memory alloy.” *J. Alloys Compd.*, 469(1–2), 156–163.

Mallik, U. S., and Sampath, V. (2015). “Effect of Grain Refinement on Shape Memory Properties of Cu-Al-Mn SMAs.” *Adv. Mater. Res.*, 1101, 104–107.

Masamichi, M., Maeshiro Noriaki, and Yoshikiyo, O. (1989). “Effects of Additional elements on the superplasticity of a Cu-14Al-3Ni shape memory alloy.” *Mater. Trans.*, 30(12), 999–1008.

Matsuoka, S., Hasebe, M., Oshima, R., and Fujita, F. E. (1983). “Improvement of Ductility of Melt Spun Cu – Al – Ni Shape Memory Alloy Ribbons by Addition of Ti or Zr.” *Jpn. J. Appl. Phys.*, 22(8), 528–530.

Matsushita, K., Okamoto, T., and Okamoto, T. (1985). “Effects of manganese and ageing on martensitic transformation of Cu-Al-Mn alloys.” *J. Mater. Sci.*, 20, 689–699.

Melo, T. A. A., Oliveira, D. F. De, Lima, S. J. G., Bueno, V. T. L., and Gomes, R. M. (2009). “Nb Modified Cu-Al-Be Shape Memory Alloys.” *Int. Conf. Martensitic Transform.*, John Wiley & Sons, Inc., 591-594.

Melton, K. N., and Mercier, O. (1979). “The Effect of the Martensitic Phase Transformation on the Low Cycle Fatigue Behaviour of Polycrystalline Ni-Ti and Cu-Zn-Al Alloys.” *Mater. Sci. Eng.*, 40, 81–87.

Moghaddam, A. O., Arash, M., and Mostafa, K. (2017). “Effect of Accumulative Roll Bonding and Equal Channel Angular Rolling on Microstructural and Mechanical Properties of Cu – Al – Mn Shape Memory Alloys.” *Trans. Indian Inst. Met.*, 70(7), 1901–1909.

- Moghaddam, A. O., Ketabchi, M., and Afrasiabi, Y. (2014). "Accumulative Roll Bonding and Post-Deformation Annealing of Cu-Al-Mn Shape Memory Alloy." *J. Mater. Eng. Perform.*, 23(December), 4429–4435.
- Montecinos, S. (2015). "Influence of microstructural parameters on damping capacity in CuAlBe shape memory alloys." *Mater. Des.*, 68, 215–220.
- Montecinos, S., and Cuniberti, A. (2012). "Martensitic Transformation and Grain Size in a Cu-Al-Be alloy." *Procedia Mater. Sci.*, 1(0), 149–155.
- Montecinos, S., Cuniberti, A., and Sepúlveda, A. (2008). "Grain size and pseudoelastic behaviour of a Cu-Al-Be alloy." *Mater. Charact.*, 59(2), 117–123.
- Moon, S. H., and Seok, H. J. (2005). "Panel flutter suppression with an optimal controller based on the nonlinear model using piezoelectric materials." *Compos. Struct.*, 68, 371–379.
- Morris, M. A. (1992). "High temperature properties of ductile Cu-Al-Ni shape memory alloys with boron additions." *Acta Met. Mater.*, 40(7), 1573–1586.
- Morris, M. A., and Lipe, T. (1994). "Microstructura Influence of Mn additions on thermoelastic and pseudoelastic properties of Cu-Al-Ni alloys." *Acta Met. mater.*, 42(5), 1583–1594.
- Nagasawa, A., and Kawachi, K. (1971). "Memory Effect in Cu-Al Alloy." *J. Phys. Soc. Japan*, 30(1), 296.
- Narasimha, G. B., and Murigendrappa, S. M. (2020). "An investigation on the properties of boron modified Cu-Al-Be polycrystalline shape memory alloys." *J. Alloys Compd.*, 823, 153733.
- Nickel, O. (1957a). "No Title." *Z.metall.*
- Nickel, O. (1957b). "No Title." *Z.metall.*, 48, 417.
- Noriyuki, K., Isao, O., Yoshitsugu, T., and Tetsuo, E. (1977). "Formation Process of α_2 Phase in Cu-Al Alloys." *Trans. Japan Inst. Met.*, 18(3), 195–203.
- Oh, J. T., Park, H. C., and Hwang, W. (2001). "Active shape control of a double-plate

structures using piezoceramics and SMA wires.” *SMARTMATERIALS Struct.*, 10, 1100–1106.

Olivier, M., and Melton, K. N. (1979). “The Substitution of Cu for Ni in NiTi Shape Memory Alloys.” *Metall. Trans. A*, 10A, 387–389.

Otsuka, K., and Shimizu, K. (1970). “MEMORY EFFECT AND THERMOELASTIC MARTENSITE TRANSFORMATION IN Cu-Al-Ni ALLOY.” *Scr. Metall.*, 4, 469–472.

Otsuka, K., and Wayman, C. M. (1999). *Shape Memory Materials*. Cambridge University Press.

Ozkul, I., Aksu Canbay, C., Aladağ, F., and Aldaş, K. (2017). “The Effect of the Aging Period on the Martensitic Transformation and Kinetic Characteristic of at % Cu68.09 Al26.1 Ni1.54 Mn4.27 Shape Memory Alloy.” *Russ. J. Non-Ferrous Met.*, 58(2), 130–135.

P.R., S., and Warlimontt, H. (1963). “The Electron-Metallography and Crystallography of Copper-Aluminium Martensites.” *Acta Metall.*, 11, 511–527.

Pan, Z. Y., Chen, J. B., and Li, J. F. (2015). “Microstructure and properties of rare earth-containing Cu-Cr-Zr alloy.” *Trans. Nonferrous Met. Soc. China (English Ed.)*, 25(4), 1206–1214.

Parameswaran, A. P., Ananthkrishnan, B., and Gangadharan, K. V. (2015). “Modeling and design of field programmable gate array based real time robust controller for active control of vibrating smart system.” *J. Sound Vib.*, 345, 18–33.

Peng, L. J., Mi, X. J., Xiong, B. Q., Xie, H. F., and Huang, G. J. (2015). “Microstructure of phases in a Cu–Zr alloy.” *Rare Met.*, 34(10), 706–709.

Perkins, J. (1974). “Substructure of Cu-Zn-Al Martensite.” *Metallography*, 7, 345–356.

Perkins, J., and Muesing, W. E. (1983). “Martensitic Transformation Cycling Effects in Cu-Zn-Al Shape Memory Alloys.” *Metall. Trans. A*, 14A(M), 33–36.

Prawdizg, T. J., Zurey, F. T., and Mack, D. J. (1966). “An investigation of the mechanical properties and microstructures of heat treated aluminium bronzes.” *Second*

Annu. Rep. to Incra.

Ramaiah, K. V., Saikrishna, C. N., Gouthama, and Bhaumik, S. K. (2013). “Microstructure and transformation behaviour of Ni₇₅- XTiXPd₂₅ high temperature shape memory alloys.” *J. Alloys Compd.*, 554, 319–326.

Ramaiah, K. V., Saikrishna, C. N., Gouthama, and Bhaumik, S. K. (2014). “Ni_{24.7}Ti_{50.3}Pd_{25.0} high temperature shape memory alloy with narrow thermal hysteresis and high thermal stability.” *Mater. Des.*, 56, 78–83.

Recarte, V., Perez-Landazabal, J. I., Rodríguez, P. P., Bocanegra, E. H., No, M. L., and San Juan, J. (2004). “Thermodynamics of thermally induced martensitic transformations in Cu – Al – Ni shape memory alloys.” *Acta Mater.*, 52, 3941–3948.

Recarte, V., R.B., P., Bocanegra, E. H., and San Juan, J. (2002). “Influence of Al and Ni Concentration on the Martensitic Transformation in Cu-Al-Ni Shape-Memory Alloys.” *Metall. Mater. Trans. A*, 33A(August), 2002–2581.

Riani, P., and Perrot, P. (n.d.). “Al-Cu-Gd (Aluminium - Copper - Gadolinium).” *Light Met. Syst. Part 2*, G. Effenberg and S. Ilyenko, eds., Springer-Verlag Berlin Heidelberg, 1–9.

Rogers, C. A. (1990). “Active vibration and structural acoustic control of shape memory alloy hybrid composites : Experimental results.” *J. Acoust. Soc. Am*, 88(6), 2803–2811.

Roh, D. W., Kim, J. W., Cho, T. J., and Kim, Y. G. (1991). “Tensile properties and microstructure of microalloyed Cu-Al-Ni-X shape memory alloys.” *Mater. Sci. Eng. A*, A136, 17–23.

Roy, F., and Teh, Y. H. (2006). “Improving the speed of shape memory alloy actuators by faster electrical heating.” *Exp. Robotics*, IX(21), 67–76.

Sampath, V. (2005). “Studies on the effect of grain refinement and thermal processing on shape memory characteristics of Cu–Al–Ni alloys.” *Smart Mater. Struct.*, 14, S253–S260.

Sampath, V. (2006). “Improvement of shape-memory characteristics and mechanical

properties of copper-zinc-aluminum shape-memory alloy with low aluminum content by grain refinement.” *Mater. Manuf. Process.*, 21(8), 789–795.

Sampath, V., and Mallik, U. S. (2009a). “Influence of minor additions of boron and zirconium on shape memory properties and grain refinement of a Cu-Al-Mn shape memory alloy.” *ESOMAT 2009 - 8th Eur. Symp. Martensitic Transform.*, 05028.

Sampath, V., and Mallik, U. S. (2009b). “Influence of minor additions of boron and zirconium on shape memory properties and grain refinement of a Cu-Al-Mn shape memory alloy.” *Mater. Soc. Annu. Meet.*, 05028, 181–188.

Santiago, J. J. de M., Alcântara, C. C. de, Costa, E. de S., and Brito, I. C. A. (2019). “Evaluation of Nb-Ni Influence on the Mechanical Behavior in a Cu-Al-Be Shape Memory Alloy.” *Curr. J. Appl. Sci. Technol.*, 32(4), 1–8.

Sari, U. (2010). “Influences of 2.5wt% Mn addition on the microstructure and mechanical properties of Cu-Al-Ni shape memory alloys.” *Int. J. Miner. Metall. Mater.*, 17(2), 192–198.

Saud, S. N., Hamzah, E., and Abubakar, T. (2014a). “Microstructure and corrosion behaviour of Cu – Al – Ni shape memory alloys with Ag nanoparticles.” *Mater. Corros.*, (Xxx), 1–8.

Saud, S. N., Hamzah, E., Abubakar, T., Bakhsheshi-Rad, H. R., Farahany, S., Abdolahi, A., and Taheri, M. M. (2014b). “Influence of Silver nanoparticles addition on the phase transformation, mechanical properties and corrosion behaviour of Cu-Al-Ni shape memory alloys.” *J. Alloys Compd.*, 612, 471–478.

Saud, S. N., Hamzah, E., Abubakar, T., Zamri, M., and Tanemura, M. (2014c). “Effects of Mn Additions on the Structure , Mechanical Properties , and Corrosion Behavior of Cu-Al-Ni Shape Memory Alloys.” *J. Mater. Eng. Perform.*, 23(10), 3620–3629.

Schwartz, M. M. (2003). *Brazing, 2nd Edition*. ASM International.

Shimizu, K., Sakamoto, H., and Otsuka, K. (1978). “Phase Diagram Associated with Stress-induced Martensitic Transformations in a Cu-Al-Ni Alloy.” *Scr. Metall.*, 12(8), 771–776.

- Song, Z., and Li, F. (2011). "Active aeroelastic flutter analysis and vibration control of supersonic beams using the piezoelectric actuator / sensor." *Smart Mater. Struct.*, 055013(20), 1–12.
- Sure, G. N., and Brown, L. C. (1984). "The Mechanical Properties of Grain Refined beta-CuAlNi Strain-Memory Alloys." *metallurg*, 15(August), 1613–1621.
- Suresh, M., Srinivasan, A., Ravi, K. R., Pillai, U. T. S., and Pai, B. C. (2009). "Influence of boron addition on the grain refinement and mechanical properties of AZ91 Mg alloy." *Mater. Sci. Eng. A*, 525(1–2), 207–210.
- Sutou, Y., Kainuma, R., and Ishida, K. (1999). "Effect of alloying elements on the shape memory properties of ductile Cu – Al – Mn alloys." *Mater. Sci. Eng. A*, 275, 375–379.
- Sutou, Y., Omori, T., Koeda, N., Kainuma, R., and Ishida, K. (2006). "Effects of grain size and texture on damping properties of Cu-Al-Mn-based shape memory alloys." *Mater. Sci. Eng. A*, 438–440(SPEC. ISS.), 743–746.
- Sutou, Y., Omori, T., Okamoto, T., Kainuma, R., and Ishida, K. (2001). "Effect of grain refinement on the mechanical and shape memory properties of Cu-Al-Mn base alloys." *J. Phys. IV*, 11, 185–190.
- Suzuki, Y., and Kagawa, Y. (2010). "Active vibration control of a flexible cantilever beam using shape memory alloy actuators." *Smart Mater. Struct.*, 19, 1–9.
- Tadesse, Y., Thayer, N., and Priya, S. (2010). "Tailoring the response time of shape memory alloy wires through active cooling and pre-stress." *J. Intell. Mater. Syst. Struct.*, 21(1), 19–40.
- Turabi, Y. A. A. S., and Vance, A. A. E. D. (2016). "The effects of substituting B for Cu on the magnetic and shape memory properties of CuAlMnB alloys." *Appl. Phys. A*, 122(7), 1–8.
- Wang, Q., Han, F., Hao, G., and Wu, J. (2006). "Influence of heat treatment on the damping behaviour of a Cu – Al – Mn shape memory alloy." *Phys. Status Solidi*, 830(5), 825–830.
- Wang, T., Chen, Z., Fu, H., Xu, J., Fu, Y., and Li, T. (2011). "Grain refining potency

- of Al-B master alloy on pure aluminum.” *Scr. Mater.*, 64(12), 1121–1124.
- Wang, X. (2005). “The formation of AlB₂ in an Al-B master alloy.” *J. Alloys Compd.*, 403(1–2), 283–287.
- West, R. F., and D. Lloyds-Thomas. (1956). “No Title.” *J. Inst. Met.*, 85(97).
- Xinyun, G., Yiu-Yin, L., and Chuh, M. (2007). “Supersonic Nonlinear Panel Flutter Suppression Using Shape Memory Alloys.” *J. Aircr.*, 44(4).
- Xu, H. P., Song, G. F., and Mao, X. M. (2011). “Influence of Be and Ni to Cu-Al Alloy Shape Memory Performance.” *Adv. Mater. Res.*, 197–198, 1258–1262.
- Xu, J. W. (2008a). “Effects of Gd addition on microstructure and shape memory effect of Cu – Zn – Al alloy.” 448, 331–335.
- Xu, J. W. (2008b). “Effects of Gd addition on microstructure and shape memory effect of Cu – Zn – Al alloy.” *J. Alloys Compd.*, 448, 331–335.
- Xu, J. W. (2008c). “Effects of Gd addition on microstructure and shape memory effect of Cu-Zn-Al alloy.” *J. Alloys Compd.*, 448(1–2), 331–335.
- Y. Aydogdu, Turabi, A. S., Aydogdu, A., Vance, E. D., Kok, M., Kirat, G., and Karaca, H. E. (2016). “The effects of substituting B for Cu on the magnetic and shape memory properties of CuAlMnB alloys.” *Appl. Phys. A*, 122(687), 1–8.
- Yang, G., Lee, J., and Jang, W. (2009). “Effect of grain refinement on phase transformation behavior and mechanical properties of Cu-based alloy.” *Trans. Nonferrous Met. Soc. China*, 19(4), 979–983.
- Yang, J., Wang, Q. Z., Yin, F. X., Cui, C. X., Ji, P. G., and Li, B. (2016a). “Effects of grain refinement on the structure and properties of a CuAlMn shape memory alloy.” *Mater. Sci. Eng. A*, 664, 215–220.
- Yang, J., Wang, Q. Z., Yin, F. X., Cui, C. X., Ji, P. G., and Li, B. (2016b). “Effects of grain refinement on the structure and properties of a CuAlMn shape memory alloy.” *Mater. Sci. Eng. A*, 664, 215–220.
- Yang, S., Zhang, F., Wu, J., Zhang, J., Wang, C., and Liu, X. (2017). “Microstructure

characterization, stress–strain behavior, superelasticity and shape memory effect of Cu – Al – Mn – Cr shape memory alloys.” *J. Mater. Sci.*, 52, 5917–5927.

Ye, Y., Yang, X., Wang, J., Zhang, X., Zhang, Z., and Sakai, T. (2014). “Enhanced strength and electrical conductivity of Cu-Zr-B alloy by double deformation-aging process.” *J. Alloys Compd.*, 615, 249–254.

Yi, G., Zhang, X., Qin, J., Ning, J., Zhang, S., Ma, M., and Liu, R. (2015). “Mechanical , electronic and thermal properties of Cu 5 Zr and Cu 5 Hf by first-principles calculations.” *J. Alloys Compd.*, 640, 455–461.

Zak, G., Kneissl, A. C., and Zatulskij, G. (1996). “SHAPE MEMORY EFFECT IN CRYOGENIC Cu-Al-Mn ALLOYS.” *Scr. Mater.*, 34(3), 363–367.

Zhang, P., Ma, A., Jiang, J., Lu, S., Lin, P., Yang, D., and Liu, G. (2010). “Microstructural evolution and mechanical response of Cu -Al - Be -B shape memory alloy processed by repetitive equal channel angular pressing.” *J. Alloys Compd.*, 497(1–2), 210–214.

Zhang, P., Ma, A., Lu, S., Lin, P., Jiang, J., Ma, H., and Chu, C. (2009). “Effect of equal channel angular pressing and heat treatment on the microstructure of Cu-Al-Be-B shape memory alloy.” *Mater. Lett.*, 63(30), 2676–2679.

Zhang, P., Ma, A., Lu, S., Liu, G., Lin, P., Jiang, J., and Chu, C. (2011). “Effect of grain refinement on the mechanical properties of Cu–Al–Be–B shape memory alloy.” *Mater. Des.*, 32(1), 348–352.

Zhang, X., Sui, J., Liu, Q., and Cai, W. (2016). “Effects of Gd addition on the microstructure, mechanical properties and shape memory effect of polycrystalline Cu-Al-Ni shape memory alloy.” *Mater. Lett.*, 180, 223–227.

Zhang, X., Zhang, M., Cui, T., Li, J., Liu, Q., and Wang, H. (2019). “The enhancement of the mechanical properties and the shape memory effect for the Cu-13.0Al-4.0Ni alloy by boron addition.” *J. Alloys Compd.*, 776, 326–333.

Zhu, M., Ye, X., Li, C., Song, G., and Zhai, Q. (2009). “Preparation of single crystal CuAlNiBe SMA and its performances.” *J. Alloys Compd.*, 478(1–2), 404–410.

List of publications based on Ph.D. research work

Sl no	Title of paper	Authors	Journal Name, Year, Volume Number, Issue, Pages)	Month, year of publication	Category*
1	Influence of Gd on the microstructure, mechanical and shape memory properties of Cu-Al-Be polycrystalline shape memory alloy https://doi.org/10.1016/j.msea.2018.09.064	<u>Guniputi Bala Narasimha</u> , S. M. Murigendrappa	Materials Science & Engineering A, 2018, 737, 245 - 252	September, 2018	1
2	Effect of zirconium on the properties of polycrystalline Cu-Al-Be shape memory alloy https://doi.org/10.1016/j.msea.2019.04.022	<u>Guniputi Bala Narasimha</u> , S. M. Murigendrappa	Materials Science & Engineering A, 2019, 755, 211 - 219.	April, 2019	1
3	An investigation on the properties of boron modified Cu-Al-Be polycrystalline shape memory alloys https://doi.org/10.1016/j.jallcom.2020.153733	<u>Guniputi Bala Narasimha</u> , S. M. Murigendrappa	Journal of Alloys and Compounds, 2020, 823, 153733	January, 2020	1

Category* 1: Journal paper, full paper reviewed

3: Conference /Symposium paper, full paper reviewed

5: Others (including paper in workshop, NITK Bulletin, short notes, etc.)

2: Journal paper, Abstract reviews

4: Conference /Symposium paper, Abstract reviewed

G. Bala Narasimha
7/7/2020

Guniputi Bala Narasimha
Research Scholar


7/7/2020
Prof. S. M. Murigendrappa
Research Guide

BIODATA

- Name:** Guniputi Bala Narasimha
- Fathers Name:** Guniputi Thirunath
- Date of Birth:** 17 -10 -1988
- Nationality:** Indian
- Marital Status:** Single
- Address:**

Permanent Address

Present Address

Department of Mechanical Engineering
National Institute of Technology Karnataka
Surathkal – 575025, Srinavasangar,
Dakshina kannada (Dist), Karnataka, India.

- Mobile Number:** 9515795349
- E-Mail:** balanarasimha.g@gmail.com
- Educational qualification:**

Qualification	College/School	University/Board	Year of passing	Performance
Ph.D.	National Institute of Technology Karnataka	National Institute of Technology Karnataka	Pursuing	8.71 (CGPA)
M.Tech – Machine Design	Madanapalle Institute of Technology and Science	J.N.T.U. Anantapur	2013	80.48 %
B.Tech – Mechanical Engineering	Chadalawada Ramanamma Engineering College	J.N.T.U. Anantapur	2010	71.01 %

10. Work experience:

Name of the organization	Duration	Position
S. V. College of Engineering.	2013 - 2014	Assistant Professor
Annamacharya Institute of Technology and Sciences.	2010 - 2011	Assistant Professor

I declare that the above information is true and correct to the best of my knowledge.

(G. BALA NARASIMHA)